

Comparative Planetary Studies of Distributed-style Volcanic Fields in the Solar System

by

Jacob Richardson

A dissertation submitted in partial fulfillment  
of the requirements for the degree of  
Doctor of Philosophy  
School of Geosciences  
College of Arts and Sciences  
University of South Florida

Major Professor: Charles B. Connor, Ph.D.  
Jacob E. Bleacher, Ph.D.  
Rocco Malservisi, Ph.D.  
Matt A. Pasek, Ph.D.  
Timothy H. Dixon, Ph.D.

Date of Approval:  
Month day, Year

Keywords: 1, 2, 3, 4

Copyright © 2016, Jacob Richardson

## Table of Contents

List of Figures	iii
Abstract	vi
1 Role of sills in the development of volcanic fields: Insights from lidar mapping surveys of the San Rafael Swell, Utah	1
1.1 Abstract	1
1.2 Introduction	1
1.3 Geologic Description	2
1.4 Lidar Reconnaissance and Analysis	4
1.5 Igneous System Reconstruction	6
1.5.1 Hebes Sill	6
1.5.2 Central Cedar Sill	8
1.6 Discussion and Conclusions	10
1.7 Acknowledgments	14
1.8 References	14
2 Validating Lava Flow Simulators using a Validation Hierarchy and Bayesian Analysis	25
2.1 Introduction	25
2.1.1 Case Study Area: 2012-3 Tolbachik Lava Flow	28
2.2 A Modular Cellular Automata Algorithm for lava flows	29
2.2.1 MOLASSES Algorithm Outline	30
2.2.2 Cells in E2	32
2.2.3 Source Locations and the Source Function	33
2.2.4 Substates and the Transition Function	33
2.2.4.0.1 Local slope-based spreading	34
2.2.4.0.2 Neighborhood size	35
2.2.4.0.3 Spreading inhibited by special relationships	35
2.2.5 Cell Neighborhood, X	36
2.3 Benchmarking Hierarchy	38
2.3.0.0.4 Test Algorithms	39
2.3.1 Level 0: Conservation of Mass	39
2.3.2 Level 1: Repeatability given meaningless parameter variation	40
2.3.2.1 Benchmark Parameters	41
2.3.2.2 Results	42

2.3.3	Level 2: Replication of flow morphologies on simple physical surfaces	43
2.3.3.1	Benchmark Parameters	44
2.3.3.2	Results	45
2.3.4	Level 3: Replication of real lava flows over complex topography	45
2.3.4.1	Results	47
2.4	Bayesian Applications for Lava Flow Models	49
2.4.0.1.1	Potential Hazard Area	52
2.4.0.1.2	Review of Validation Level 3	54
2.4.1	Improving model performance on one model parameter	55
2.4.1.1	Model Execution	56
2.4.1.2	Results	57
2.4.2	Incorporating Model Uncertainty with a Monte Carlo method	59
2.4.2.1	Bayesian distribution of MC results	60
2.4.2.2	Estimating inundation risk from the simulated frequency of inundation	61
2.5	Discussion	65
2.5.1	Benchmark Validation	65
2.5.2	Bayesian applications for real lava flows	66
2.5.2.1	Using Bayesian statistics to compare models	67
2.5.2.2	Decision Making with the Bayes Factor	67
2.6	Conclusions	69
2.7	Data Statement	71
2.8	References	71
3	The Volcanic History of Syria Planum, Mars	74
3.1	Abstract	74
3.2	Introduction	75
3.2.1	Geologic Description	76
3.3	Methods	79
3.3.1	Study Area	79
3.3.2	Catalog of Volcanic Vents	80
3.3.3	Crater Counting	82
3.3.4	Nearest Neighbor Analysis	83
3.3.5	Two-point azimuthal analysis	85
3.4	Results	86
3.4.1	Mapping	86
3.4.2	Age-Dating	88
3.4.3	Nearest Neighbor Analysis	90
3.4.4	Two-point azimuthal analysis	92
3.5	Discussion	94
3.6	Conclusion	101
3.7	Acknowledgments	103
3.8	References	104

## List of Figures

Figure 1.1	Shaded relief map of airborne laser scanning data, San Rafael Swell, Utah (USA).	3
Figure 1.2	Northwest-facing panoramic diagram of Central Cedar sill	6
Figure 1.3	Sill thickness contour plots of Hebes and Central Cedar sills	7
Figure 1.4	Chart of measured thicknesses and elevations of Central Cedar sill	9
Figure 1.5	Photograph and lidar point cloud of the east face of Cedar Mountain	11
Figure 1.6	Contour plots of thickness models over ALSM hillshade data for additional sills	12
Figure 2.1	The Tolbachik region of Kamchackta, Russia	28
Figure 2.2	MOLASSES flow chart	31
Figure 2.3	A 2-D example of two transition functions with different slope treatments	34
Figure 2.4	A 2-D example of different transition functions with different “parentage” rules	36
Figure 2.5	Cellular Automata neighborhoods	37
Figure 2.6	Rotating slope test for the LavaPL algorithm	41
Figure 2.7	Fitness scores of different shaped flows on a flat surface	44
Figure 2.8	Three transition function algorithms simulating the 2012-3 Tolbachik lava flows	47
Figure 2.9	Potential hazard areas of the 2012-3 Tolbachik Flows	54
Figure 2.10	MOLASSES Simulations with different Pulse Volume parameter values of the 2012-3 Tolbachik Lava Flows	57

Figure 2.11	Posterior $\Pr(Lava Sim)$ for MOLASSES flows with differing Pulse Volumes.	58
Figure 2.12	Negative posterior $\Pr(\neg Lava \neg Sim)$ for MOLASSES flows with differing Pulse Volumes.	58
Figure 2.13	Map of Monte Carlo simulations of the 2012-3 Tolbachik lava flows	60
Figure 2.14	Fitness statistic distribution of Monte Carlo simulations of the 2012-3 Tolbachik lava flows	61
Figure 2.15	Sub-regions within the Monte Carlo solution, defined by $\Pr(Sim)$	62
Figure 2.16	Relative likelihood of inundation given $\Pr(Sim)$	64
Figure 2.17	Weighted averages of $\Pr(Lava Sim)$ and $\Pr(\neg Lava \neg Sim)$ for different pulse volumes	68
Figure 3.1	Geologic Map of Syria Planum	78
Figure 3.2	Graphical summary of age-dating results by unit.	89
Figure 3.3	Plot of vents with lines drawn to their nearest neighbors.	89
Figure 3.4	Plots of skewness vs. kurtosis values for 95% of 1000 simulated Poisson spatial distributions	91
Figure 3.5	Plot of vents and all inter-vent relationships less than the minimum significant distance.	92
Figure 3.6	Distribution of inter-vent distances and inter-vent alignments	93
Figure 3.7	Map of tectonic centers from Anderson et al. (2001)	99

## **Abstract**

Sills are important, but so is lava. There are volcanoes on Mars around Arsia Mons and Syria Planum. Volcano clusters can be compared with non-parametric statistics even if they are on different planets.

# **1. Role of sills in the development of volcanic fields: Insights from lidar mapping surveys of the San Rafael Swell, Utah<sup>1</sup>**

## **1.1 Abstract**

Analysis of airborne and terrestrial lidar data demonstrates that  $>0.4 \text{ km}^3$  of magma cooled in sills at shallow ( $<1 \text{ km}$ ) depth in the now eroded Pliocene San Rafael Swell distributed volcanic field, Utah (USA). The volumes of each of seven sills are estimated from 3D models of the lidar data and range from  $10^{-4}$ - $10^{-1} \text{ km}^3$ . Directions of magma flow during emplacement are interpreted from precise sill thickness measurements and measurements of linear vertical offsets within the sills, helping to identify feeder conduits and dikes; 3D map relationships derived from lidar data demonstrate that magma flowed into and out of sills from these active dikes and eruptive conduits. Mapped sill volumes account for  $>92\%$  of intrusive material within the  $50 \text{ km}^2$  study area. We conclude that sills played a significant role in modifying eruption dynamics during activity in San Rafael, and suggest that monitoring of sill inflation and deflation in active distributed volcanic fields may provide key information about unrest and potential eruption dynamics.

## **1.2 Introduction**

Intermediate to shallow crustal storage of pre- and syn-eruption magma modulates magma supply rate in many volcanic systems. At Mount St. Helens (A.D. 1980 eruption; USA) and Parícutin (A.D. 1943 eruption; Mexico), magma supply rate is thought to have been influenced by the presence of shallow ( $<10 \text{ km}$ ), temporary magma storage (Cashman and McConnell, 2005) and by the length of storage time (Scandone et al., 2007). Erlund et al. (2010) identified increasing amounts of shallow crust ( $\leq 4 \text{ km}$  depth) assimilated at

---

<sup>1</sup>This chapter has been reprinted from Geology with permission from XXX as: Richardson, J. A., ...

Parícutin over the 9-year eruption, and concluded that a shallow intrusion network formed early and caused later eruptive products to be more effusive. On shorter timescales, gas may segregate preferentially into conduits above shallow sills, increasing volumetric flow in the conduit and intensifying the eruption (Conte, 2000; Pioli et al., 2009). Sill-like intrusions into shallow magma chambers have recently been geodetically linked with interferometric synthetic aperture radar (InSAR) and seismic monitoring to eruptions at Tungurahua, Ecuador (Biggs et al., 2010) and Eyjafjallajökull, Iceland (Tarasewicz et al., 2012). These models and observations suggest that it is critical to understand the volume, depth and distribution of sills in volcanic fields in order to forecast eruption dynamics and the evolution of volcanic systems. In young volcanic fields, such as the one around Parícutin (Connor, 1990), it is not possible to directly observe the shallow plumbing system. Here, we use lidar technology to map part of the eroded San Rafael Swell (UT) volcanic field. These data demonstrate that sills are prevalent at shallow depths (<1 km), modulated magma flow in eruptive conduits, and likely influenced eruption dynamics within this volcanic field.

### 1.3 Geologic Description

The San Rafael volcanic field was active between 4.6 and 3.8 Ma (Delaney and Gartner, 1997). This volcanic field is part of a larger occurrence of Cenozoic basaltic volcanism in the Colorado Plateau and Basin and Range provinces but is distinct from many other fields as it has been eroded to a depth of ~800 m, based on its age and late Cenozoic erosion rates (Pederson et al., 2002, e.g.). The sill-and-dike swarm, or volcanic plumbing system, cut a Jurassic sedimentary section from the Carmel Formation through the Cutler Formation. Diabasic dikes in this area trend 335° to 0° (relative to north) along regional joint sets, indicating low horizontal deviatoric stress during emplacement (Delaney and Gartner, 1997). Sills in the San Rafael Swell range from <5 m to >40 m thick and are exposed in cliff sides and canyons in outcrops that extend for 100s-1000s m. This shallow magma plumbing system has been mapped (Delaney and Gartner, 1997), and used to improve our understanding of (i) dike emplacement (Delaney et al., 1986), (ii) magma diapirism in the shallow crust (Diez

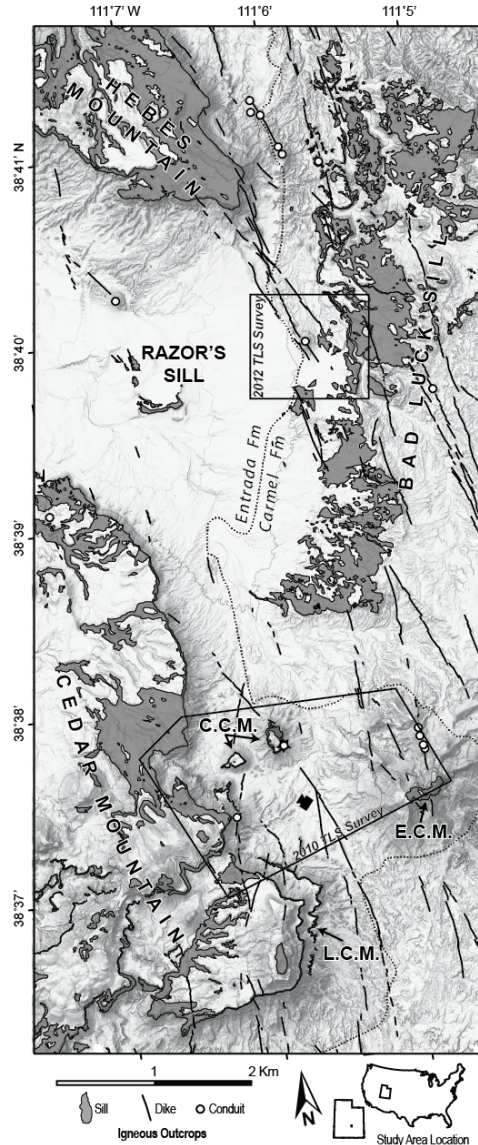


Figure 1.1: Shaded relief map of airborne laser scanning data, San Rafael Swell, Utah (USA) with formation contact and terrestrial laser scanning (TLS) areas labeled. Sills mapped are Hebes, Bad Luck, Razor's, Cedar Mountain, Lower Cedar Mountain (LCM), Central Cedar Mountain (CCM), and East Cedar Mountain (ECM). Starred conduit symbol near CCM denotes conduit that was formed concurrently with CCM sill. Camera symbol near CCM is view location of Figure 1.2.

et al., 2009), and (iii) the spatial relationships between dikes and conduits (Kiyosugi et al., 2012), the latter of which are commonly surrounded by brecciated country rock, indicating conduit erosion during rapid magma ascent. Although Gartner (1986) described physical characteristics of exposed sills in the area, the complex emplacement processes of sills in this volcanic field have remained enigmatic. With the aid of lidar, we are able to document the complex map relationships between intrusions in the area.

#### 1.4 Lidar Reconnaissance and Analysis

Terrestrial laser scanning (TLS), performed in 2010 and 2012, collected a 7.3 GB point cloud over an area of  $5 \text{ km}^2$ . Both TLS surveys used Riegl terrestrial scanners. An airborne laser scanning (ALS) survey, in 2013, provided data for a  $54 \text{ km}^2$  airborne laser swath map (ALSM) (Richardson, 2013), connecting the 2 TLS surveys into a single study area (Figure 1.1). Instrument specifications and data formats from these surveys are outlined in Table 1.3. Co-registering the coordinate systems of the three surveys creates a coverage area of  $\sim 50 \text{ km}^2$ , within which relief varies by up to 500 m. Thus, we are able to characterize the magma plumbing system in a tabular block approaching  $25 \text{ km}^3$  in volume, which bounds the study area extent. This reconstruction of a magmatic plumbing system attempts to model the amount of magma emplaced into the crust due to Pliocene volcanism for the  $25 \text{ km}^3$  space.

The three point clouds (two TLS and one ALSM) were consolidated and analyzed using LiDAR Viewer software (Kreylos et al., 2008). Because the three-dimensional point cloud is so precise, lidar data help identify subtle changes in sill thickness over large areas, vertical offsets in sills, and disrupted stratigraphy in overlying sedimentary units, which allow magma movements to be deduced. Contacts between igneous and sedimentary rocks are identified by shade contrast (igneous rocks are generally darker than sedimentary rocks in the near-infrared point cloud) and weathering patterns easily observable in the point cloud (Figure 1.5). Thickness measurements are made in LiDAR Viewer where sill upper and lower contacts are seen in close proximity. The exact locations of sill contacts are manually

picked between points in the point cloud, where one point is interpreted as sill and the other as sedimentary rock (Table 4). Uncertainty at each measurement is determined as the average of point-to-point distances on top and bottom of the sill and is drastically reduced in areas where both TLS and ALSM data are available. Other measurements made in LiDAR Viewer include sill base elevations and strikes and dips of continuous sill segments and of sedimentary host rock below sills. Locations where sills abruptly change stratigraphic level are also mapped in the field. These abrupt changes can be traced between outcrops with point cloud measurements.

Sill exposures are mapped using 1 m National Agriculture Imagery Program (NAIP) images and the ALSM digital elevation model (DEM). These are combined with thickness measurements to estimate terminal boundaries of sills. The lateral edges of sills are not commonly preserved in outcrop, so we have estimated the terminal boundary of each sill to extend no more than 0.5 km from current exposures. Sills commonly crop out at cliffs with little horizontal exposure area (Figure 1.2), and by assuming that the mapped sills are contiguous between these outcrops, mapped sill areas are relatively small in comparison to interpreted sill areas (Table 1.1). Sill volume and average thickness are modeled by constraining the thicknesses of sills at their respective modeled boundaries to be 0 m and interpolating a Laplacian-spline surface within sill boundaries, calibrated to the measured thicknesses (Figures 1.3 and 1.6). Results from mapped and modeled areas, and maximum measured thicknesses, are detailed in Table 1.1.

Using aerial images and field mapping, Kiyosugi et al. (2012) mapped 16 conduits and 180 vertical, en echelon dike segments, with a cumulative length of 53 km, that crop out in the study area (Figure 1.1). The cumulative volume of igneous material stored in dikes is estimated to be the product of dike length, the modeled block height, and 85 cm, the modal dike thickness (Delaney and Gartner, 1997). This might be a slight overestimate as some dikes might not have cut through the entire block height. The volume stored in conduits is the product of the surface area, mapped with the ALSM DEM and NAIP images, of each



Figure 1.2: Northwest-facing panoramic diagram of Central Cedar sill, shaded dark gray (see Figure 1.1 for location). Other igneous intrusions are lighter gray, including sill capping Cedar Mountain (background), a conduit, and a dike.

conduit and the modeled block height. This assumes conduit thickness does not change within the vertical limits of this reconstruction and might underestimate volume if conduits widen toward the surface or formed above the present-day surface.

## 1.5 Igneous System Reconstruction

Seven isolated sills crop out within the study area. We interpret these sills to have been emplaced independently as a result of single dike injections, based on evidence described below. Sill volumes range from  $10^{-4}$ - $10^{-1}$  km $^3$  and have been emplaced over areas of  $10^{-1}$  to tens of square kilometers (Table 1.1). Through modeling sill geometries, we find that  $\sim 0.4$  km $^3$  of igneous material is permanently stored in the sills, representing 93% of all intrusive rocks in our reconstructed volume. Table 1.2 summarizes mapped areas and modeled volumes of sills, dikes, and conduits within the study area. By combining adjacent conduits along the same dike, we estimate that 12 distinct volcanic events are represented within the study area. Emplacement processes of sills and their role in the development of the Pliocene volcanic field can be further understood by investigating individual sills.

### 1.5.1 Hebes Sill

The sill at Hebes Mountain (Figure 1.1) is primarily preserved as a single 1.9 km $^2$  sill exposed over an area of  $\sim 4$  km $^2$ . This sill generally dips with strata 1°-8° to the northwest, although locally some areas dip 5°-30° toward the center of the sill. Sill thicknesses are measured to a precision of  $\pm 75$  cm, with virtually all exposures measuring  $> 19$  m. The sill

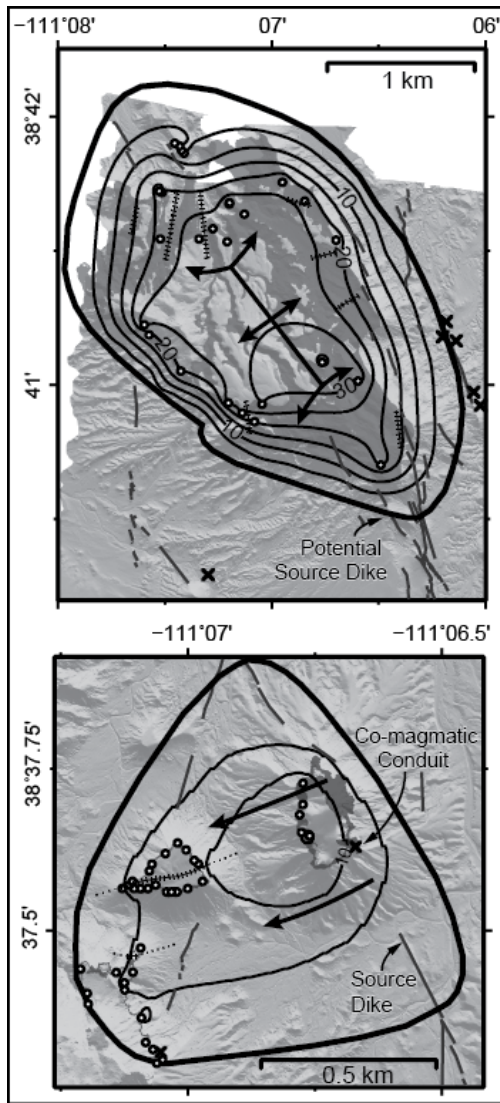


Figure 1.3: Sill thickness contour plots of Hebes (top) and Central Cedar (bottom) sills. White circles show measurement locations; X symbols are mapped conduits; gray lines are dikes; shaded areas are mapped sills. Thick lines with arrows indicate inferred direction of magma injection; hashed and dotted lines indicate mapped and inferred vertical sill offsets, respectively. Thick contours mark modeled sill boundaries where thickness is modeled to be 0 m.

Table 1.1: Areas, Thickness, and Volumes for 7 Sills in the Eroded San Rafael Swell Volcanic Field

Sills	Observations		Modeled values		
	Mapped area* ( $10^3$ m $^2$ )	Max thickness*	Modeled area ( $10^3$ m $^2$ )	Volume (km $^3$ )	Mean thickness
Bad Luck	2901±141	19.0±0.2 m	13040	$9.45 \times 10^{-2}$	7.3 m
Cedar Mountain	2782±149	40.7±0.2	25570	$2.78 \times 10^{-1}$	10.9
Hebes	1919±45	36.1±0.1	5390	$8.47 \times 10^{-2}$	15.7
East Cedar Mountain	39±2	N/A <sup>†</sup>	130	$4.08 \times 10^{-4}$	3.0
Razor's	37±4	7.8±0.2	1270	$1.62 \times 10^{-3}$	1.3
Central Cedar Mountain	26±5	15.5±0.1	880	$4.42 \times 10^{-3}$	5.0
Lower Cedar Mountain	20±5	14.4±0.2	1030	$5.44 \times 10^{-3}$	5.3

\* Area uncertainty determined by assuming a 1-pixel-width error in mapping with 1-m basemap image. Thickness uncertainty calculation is discussed in the text.

† Sedimentary rocks are not observed above East Cedar Mountain Sill, inhibiting thickness measurements.

thins monotonically from the center to the edges of Hebes Mountain, thinning most rapidly to the southwest.

By modeling Hebes sill as a  $5.4 \text{ km}^2$  area, roughly following the shape of Hebes Mountain, the volume is estimated to be  $8.5 \times 10^{-2} \text{ km}^3$ . The elongate nature of this sill model (Figure 1.3), with increased thickness trending in the northwest dip direction is aligned in the regional dike direction, perhaps indicating a linear source region (dike) feeding the sill.

### 1.5.2 Central Cedar Sill

The Central Cedar sill caps two buttes to the east of Cedar Mountain and is exposed on the east facing cliffs of Cedar Mountain (Figure 1.2). The outcrops are interpreted to be parts of a single sill, as their basal contacts project across the small valleys between each exposure at the same elevation. Measured thicknesses of the Central Cedar Sill are 2-15 m, with basal contacts that dip with sedimentary host rock, at 2-5° WNW to SW. The

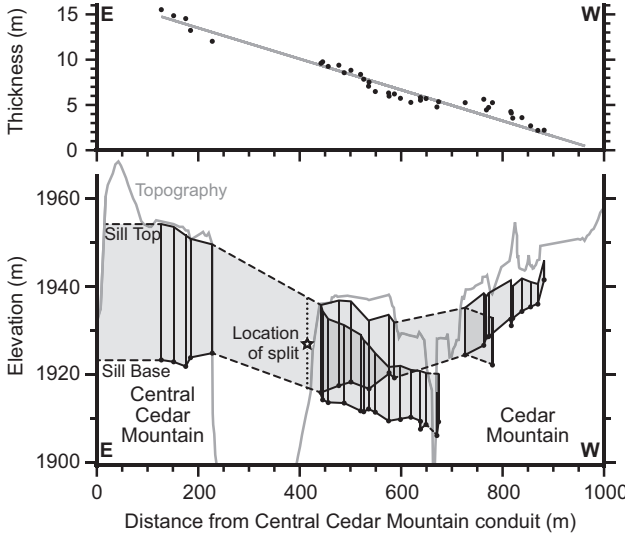


Figure 1.4: Top: Measured thicknesses of Central Cedar sill with respect to distance from conduit on Central Cedar Mountain with superimposed linear trend. All vertical errors are within size of plotted points. Bottom: Pseudo-cross section of Central Cedar sill superimposed on current topographic profile. Filled circles represent measured basal elevation (m above sea level) of sill; shaded area represents interpolated sill. Dotted line (star symbol) is inferred location where sill splits into two branches, manifested as step-ups in outcrop.

sill outcrops adjacent to a conduit associated with a  $\sim 2$  km long dike on Central Cedar Mountain. Basalt between the conduit and sill appears continuous, with no brecciation, suggesting the dike and sill were formed cotemporally, and were thus comagmatic.

The average uncertainty in thickness measurements for Central Cedar Sill is  $< 20$  cm, due to coverage from both ALSM and TLS data sets. The point cloud also enables the mapping of curvilinear “step-up” features, defined by Gartner (1986) as vertical offsets between different intrusion pathways, or feathers. Flow direction during intrusion is interpreted to be parallel to step-ups. Step-ups in this sill indicate flow to the W-WNW, away from and/or toward, the conduit. Modeling this sill as a tongue-shaped body intruding to the west from the suspected source dike (Fig S1, top center), Central Cedar Sill has an areal extent of  $\sim 0.88 \text{ km}^2$ , and a total volume of  $4.4 \times 10^{-3} \text{ km}^3$  (Table 1.1).

A linearly thinning trend away from the conduit is evident in the sill, continuing for 1 km to the observed sill limit (Figure 1.4). Within 100 m of the conduit, sill thickness changes dramatically due to the presence of rotated sandstone blocks with thin basalt lenses

Table 1.2: Igneous Material Contributions in the Study Area

	Area (km <sup>2</sup> )	Volume (km <sup>3</sup> )	Vol% of intrusives
Sills	34.5	$4.1 \times 10^{-1}$	92.9
Dikes	$4.5 \times 10^{-2}$	$2.2 \times 10^{-2}$	5.0
Conduits	$1.9 \times 10^{-2}$	$9.5 \times 10^{-3}$	2.1
Total	34.6	$4.5 \times 10^{-1}$	1.8
Model Space	50.0	25.0	—

injected over the tops of the sandstone blocks, indicating roof collapse into the sill (Figure 1.2). From these observations we conclude that the Central Cedar Sill was fed from a single dike and was emplaced in a tongue-like fashion to the west in its initial dipping direction. Further, we infer that a conduit-forming volcanic event may have halted further advance of the sill and subsequent flow of magma from the sill into the conduit caused the observed conduit-adjacent roof collapse.

## 1.6 Discussion and Conclusions

Through lidar mapping of the San Rafael study area, seven sill-forming events in the shallow crust and 12 conduit-forming events have been identified and mapped in detail (Figure 1.1). We model the total volume of igneous material stored in sills to be 0.4 km<sup>3</sup> within a 25 km<sup>3</sup> block. This sill volume represents 93% of the stored igneous volume in the block, with the remaining 7% in dikes and conduits. There is no doubt that, volumetrically, sills are a critical component of the magma plumbing system in this distributed volcanic field.

It is possible, in fact, that sill volume in the San Rafael Sell volcanic field is comparable to erupted volume. Eruption volumes for the 12 conduits cannot be directly observed, as those lavas are completely eroded away. Eruption volumes for monogenetic volcanoes in similar fields span three orders of magnitude, ranging from  $10^{-3}$  to  $10^{-1}$  km<sup>3</sup> (Crowe et al., 1983; Condit et al., 1989; Kiyosugi et al., 2012, e.g.). If we assume that average eruption volume is 0.1 km<sup>3</sup> for conduits in the San Rafael Swell,  $\sim 1.2$  km<sup>3</sup> of basalt would have been

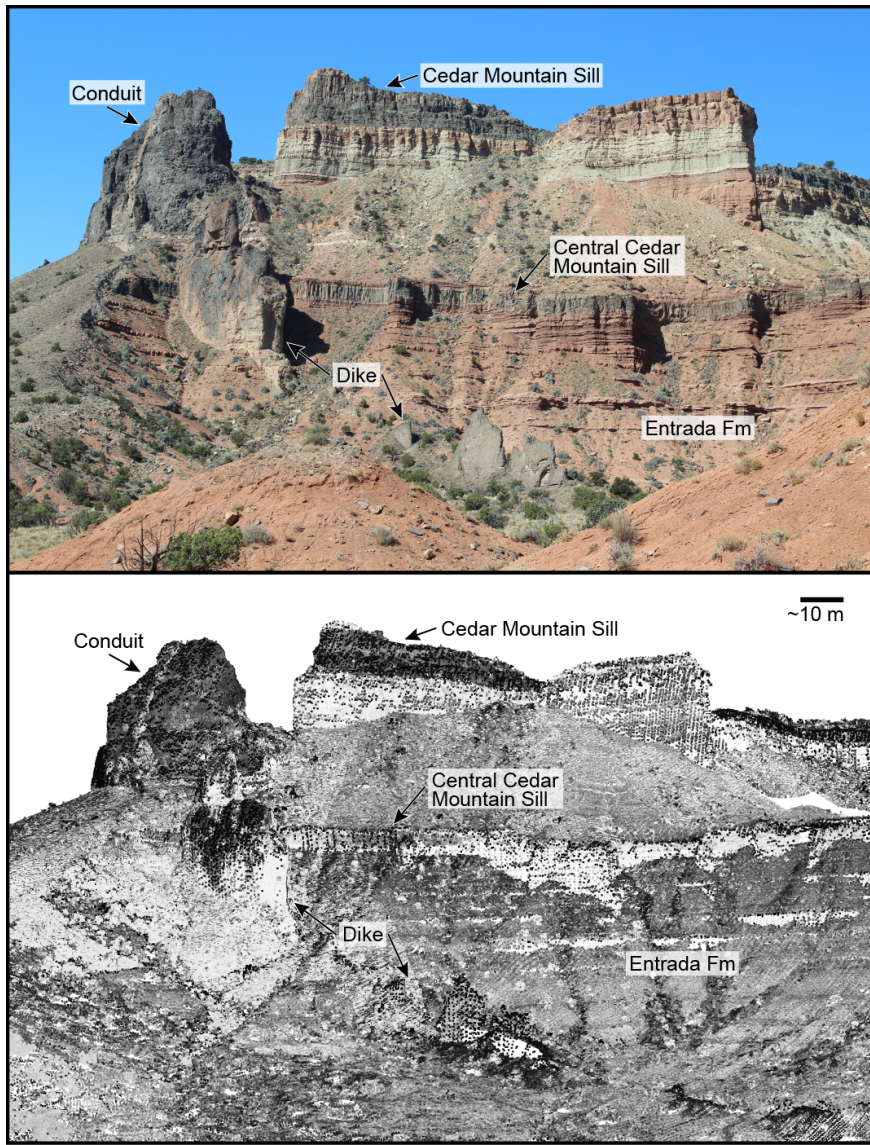


Figure 1.5: Top: Photograph of the east face of Cedar Mountain featuring Central Cedar Sill, Cedar Mountain Sill, and a dike which cross-cuts Central Cedar Sill. Sills are separated by dozens of meters by sedimentary rock. Photograph courtesy of J. McIlrath. Bottom: Combined TLS and ALS point cloud of the same view. Near-Infrared intensity differentiates between igneous and sedimentary rocks.

erupted at the surface, four times the estimated sill volume. Again, this comparison suggests that, volumetrically, crustal storage of magma in sills is a major feature of the magmatic system.

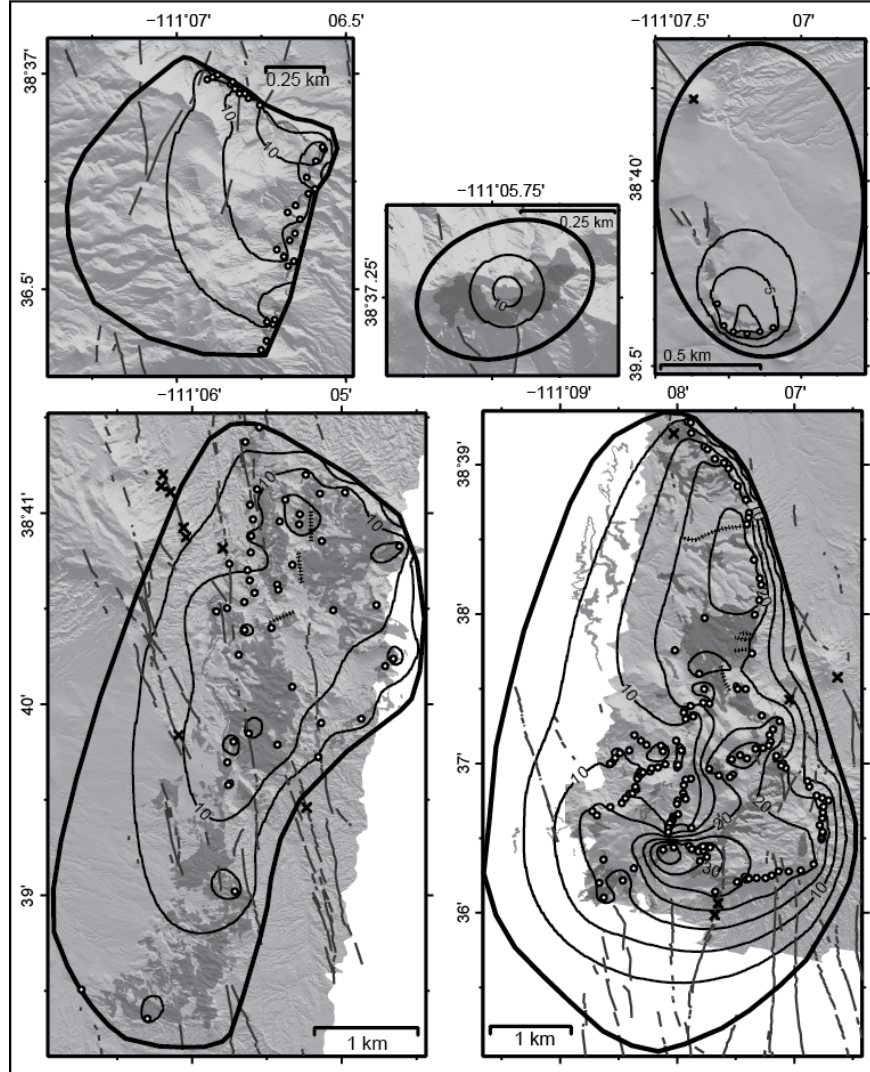


Figure 1.6: Contour plots of thickness models over ALSM hillshade data for additional sills. White circles are measurement locations; Xs are mapped conduits; gray lines are dikes; shaded areas are mapped sills. Thick lines with arrows indicate the inferred direction of magma injection and hashed/dotted lines indicate mapped/inferred vertical sill offsets. Top row, left to right sills are: Lower Cedar, East Cedar Mountain, Razor's; Bottom row, left to right: Bad Luck, Cedar Mountain. Contour intervals are 5 m thickness except Razor's sill where contours are every 2.5 m. Thick contours mark the modeled sill boundaries where sill thickness is modeled to be 0 m thickness. Note change in map scale.

The general shape of the mapped sills in this field does include a thick center of several to tens of meters in height, tapering edges, and horizontal dimensions of one to several kilometers. While smaller sills exhibit a monotonic decrease in thickness from their interiors (Figure 1.4), the thickness profiles of larger sills are more complex and multiple thickened zones exist (Figure 1.6). The irregular shapes and size range of these sills might suggest that all sills in this area are the product of single injection events and are not polygenetic (Gudmundsson, 2012). Furthermore, the maximum observed thicknesses of each of these sills are not highly correlated to the exposed or modeled areas of each sill. Sills in this area generally ascend stratigraphy only after lifting the roof, enabling exploitation of new bedding planes, suggesting that initial emplacement at this depth was a pressure-driven process, similar to the intrusion of the Trachyte Mesa laccolith (Henry Mountains, Utah, USA) (Wetmore et al., 2009). Because horizontal deviatoric stress was low in this area during the Pliocene (Delaney et al., 1986), the minimum compressive stress direction could have significantly migrated from horizontal at 1 km depth, enabling sill formation given local stress conditions influenced by overlying topography (Gudmundsson, 2012).

The development of shallow sills likely affected eruption dynamics. If a comagmatic sill is present during a volcanic eruption, ascending bubbles can become concentrated in the vertical conduit at the conduit-sill junction by disproportional capture of the liquid phase of a two-phase flow in the horizontal branch (Conte, 2000). This concentration occurs if overall magma flux is sufficiently low. The presence of the sill, therefore, enables modulation of explosive potential, with low magma flow rates resulting in more explosive activity than if a sill was not present. Following the method of Pioli et al. (2009), assuming a magma density of  $2800 \text{ kg/m}^3$ , we calculate the transition flux to be  $1.8 \times 10^5 \text{ kg/s}$  within the Central Cedar Mountain conduit (diameter 25 m), where lower flux would have concentrated bubbles in the conduit system. As average mass eruption rate for strombolian eruptions is commonly observed to be  $10^3\text{-}10^5 \text{ kg/s}$  (Pioli et al., 2009), the presence of sills at the level where  $\text{H}_2\text{O}$  exolves critically impacts volcanic hazard.

Sills have been identified as a major instigator of unrest in association with strato-volcanoes (Biggs et al., 2010; Tarasewicz et al., 2012, e.g.), volcanic calderas (Macedonio et al., 2014), and monogenetic volcanic eruptions (Erlund et al., 2010). The observation in the San Rafael Swell that the vast majority of igneous rock at 1 km depth is contained in sills suggests that similar deformation events may be precursory to volcanic eruptions in some active volcanic fields. Monitoring of active volcanic fields may benefit from use of deformation networks to detect sill emplacement in the shallow crust.

## 1.7 Acknowledgments

This project would not have been possible without the support of David Phillips and UNAVCO for lidar field equipment and data processing assistance. The TLS data acquisition project was funded by a grant from the National Science Foundation (EAR-0910696). ALS data acquisition and processing was completed by the National Center for Airborne Laser Mapping (NCALM) with funding provided by NSF's Division of Earth Sciences, Instrumentation and Facilities Program (EAR-1043051). M. Oskin and O. Kreylos of UC Davis are thanked for their help regarding LiDAR Viewer. USF students and faculty, Judy McIlrath, Kaz Mannen, Koji Kiyosugi, James Wilson, Samantha Kinman, and Travis Doering are thanked for field assistance. Helpful comments from K. Cashman, A. Gudmundsson, and an anonymous reviewer improved this manuscript.

## 1.8 References

- Biggs, J., Mothes, P., Ruiz, M., Amelung, F., Dixon, T., Baker, S., and Hong, S.-H. (2010). Stratovolcano growth by co-eruptive intrusion: The 2008 eruption of Tungurahua Ecuador. *Geophysical Research Letters*, 37(21).
- Cashman, K. and McConnell, S. (2005). Multiple levels of magma storage during the 1980 summer eruptions of Mount St. Helens, WA. *Bulletin of Volcanology*, 68(1):57–75.

- Condit, C. D., Crumpler, L. S., Aubele, J. C., and Elston, W. E. (1989). Patterns of volcanism along the southern margin of the Colorado Plateau: The Springerville Field. *Journal of Geophysical Research*, 94(B6):7975–7986.
- Connor, C. B. (1990). Cinder Cone Clustering in the TransMexican Volcanic Belt: Implications for Structural and Petrologic Models. *Journal of Geophysical Research*, 95(B12):19,395–19,405. doi:10.1029/JB095iB12p19395.
- Conte, G. (2000). *An experimental study for the characterisation of gas/liquid flow splitting at T-junctions*. PhD thesis, The University of Nottingham.
- Crowe, B., Self, S., Vaniman, D., Amos, R., and Perry, F. (1983). Aspects of potential magmatic disruption of a high-level radioactive waste repository in southern Nevada. *The Journal of Geology*, pages 259–276.
- Delaney, P. and Gartner, A. (1997). Physical processes of shallow mafic dike emplacement near the San Rafael Swell, Utah. *Geological Society of America Bulletin*, 109(9):1177–1192.
- Delaney, P., Pollard, D., Ziony, J., and McKee, E. (1986). Field relations between dikes and joints: emplacement processes and paleostress analysis. *Journal of Geophysical Research: Solid Earth*, 91(B5):4920–4938.
- Diez, M., Connor, C., Kruse, S., Connor, L., and Savov, I. (2009). Evidence of small-volume igneous diapirism in the shallow crust of the Colorado Plateau, San Rafael Desert, Utah. *Lithosphere*, 1(6):328–336.
- Erlund, E., Cashman, K., Wallace, P., Pioli, L., Rosi, M., Johnson, E., and Granados, H. (2010). Compositional evolution of magma from Parícutin Volcano, Mexico: the tephra record. *Journal of Volcanology and Geothermal Research*, 197(1):167–187.

Gartner, A. (1986). *Geometry, Emplacement History, Petrography and Chemistry of a Basaltic Intrusive Complex, San Rafael and Capitol Reef Areas, Utah*. US Department of the Interior, Geological Survey.

Gudmundsson, A. (2012). Magma chambers: Formation, local stresses, excess pressures, and compartments. *Journal of Volcanology and Geothermal Research*, 237:19–41.

Kiyosugi, K., Connor, C., Wetmore, P., Ferwerda, B., Germa, A., Connor, L., and Hintz, A. (2012). Relationship between dike and volcanic conduit distribution in a highly eroded monogenetic volcanic field: San Rafael, Utah, USA. *Geology*, 40(8):695–698.

Kreylos, O., Bawden, G., and Kellogg, L. (2008). Immersive Visualization and Analysis of LiDAR Data. In Bebis, G., Boyle, R., Parvin, B., Koracin, D., Remagnino, P., Porikli, F., Peters, J., Klosowski, J., Arns, L., Chun, Y., Rhyne, T.-M., and Monroe, L., editors, *Advances in Visual Computing*, volume 5358 of *Lecture Notes in Computer Science*, pages 846–855. Springer Berlin Heidelberg.

Macedonio, G., Giudicepietro, F., D'Auria, L., and Martini, M. (2014). Sill intrusion as a source mechanism of unrest at volcanic calderas. *Journal of Geophysical Research: Solid Earth*, 119(5):3986–4000.

Pederson, J., Mackley, R., and Eddleman, J. (2002). Colorado Plateau uplift and erosion evaluated using GIS. *GSA TODAY*, 12(8):4–10.

Pioli, L., Azzopardi, B., and Cashman, K. (2009). Controls on the explosivity of scoria cone eruptions: Magma segregation at conduit junctions. *Journal of Volcanology and Geothermal Research*, 186(3-4):407 – 415.

Richardson, J. (2013). San Rafael, UT: Survey of exposed subsurface volcanic features. doi: 10.5069/G908638S.

Scandone, R., Cashman, K., and Malone, S. (2007). Magma supply, magma ascent and the style of volcanic eruptions. *Earth and Planetary Science Letters*, 253(3):513–529.

Tarasewicz, J., White, R. S., Woods, A. W., Brandsdóttir, B., and Gudmundsson, M. T. (2012). Magma mobilization by downward-propagating decompression of the eyjafjallajökull volcanic plumbing system. *Geophysical Research Letters*, 39(19).

Wetmore, P., Connor, C., Kruse, S., Callihan, S., Pignotta, G., Stremtan, C., and Burke, A. (2009). Geometry of the Trachyte Mesa intrusion, Henry Mountains, Utah: Implications for the emplacement of small melt volumes into the upper crust. *Geochemistry, Geophysics, Geosystems*, 10(8).

Table 1.3: Lidar Survey Specifications

Survey Date	Instrument	Camera	Instrument Accuracy/Misfit*	Points per m <sup>2</sup>	Data Format
June 2010	Riegl LMS-Z620	Nikon D200	10 mm/13 cm standard misfit between tiepoints	49	XYZRGBI ASCII
May 2012	Riegl VZ-400	Nikon D200	5 mm/11 cm standard misfit between tiepoints	148	XYZRGBI ASCII
August 2013	Optech Gemini ALTM	N/A	5-35 cm/5cm interswath misfit	6.25	LAS

\* Misfit in Riegl point clouds are reported after Georeferencing to WGS84 in RiSCAN Pro 1.8.0.

Table 4: Sill Thickness Measurements made  
in Lidar Viewer

<b>Cedar Mountain Sill</b>			
Easting*	Northing*	Thickness	
489663 m	4274770 m	21.28±0.10 m	
489243	4275170	16.39±0.74	
489144	4275170	14.35±0.22	
488668	4275360	11.95±0.15	
488367	4275650	18.56±0.17	
488735	4276050	19.51±0.12	
488524	4278480	7.38±0.49	
488565	4278470	1.85±0.28	
488574	4278340	9.08±0.30	
488736	4278170	12.58±0.21	
488774	4278140	13.88±0.26	
488867	4278020	13.42±0.15	
488979	4277970	14.78±0.13	
489031	4277900	15.47±0.20	
489147	4277680	18.52±0.49	
489249	4277510	16.47±0.28	
489288	4277350	17.82±0.20	
489282	4277290	18.27±0.14	
489258	4277210	19.37±0.38	
489348	4276770	24.83±0.42	
489420	4276540	21.68±0.33	
	489438	4276460	20.01±0.52
	489412	4276270	22.84±0.29
	489356	4276090	18.12±0.15
	489322	4275610	15.10±0.05
	489442	4274840	16.60±0.15
	489579	4274670	22.89±0.21
	489538	4274600	22.18±0.18
	489551	4274520	23.53±0.14
	489528	4274470	23.81±0.17
	489456	4274440	24.55±0.10
	489363	4274430	27.37±0.15
	489257	4274310	27.51±0.29
	489173	4274350	27.05±0.15
	489067	4274300	26.20±0.29
	489083	4274110	22.68±0.16
	489046	4274080	22.26±0.15
	488908	4274100	18.50±0.32
	488790	4274180	23.49±0.21
	488729	4275170	24.68±0.07
	488717	4275000	15.07±0.21
	488560	4274960	15.52±0.16
	488486	4274910	14.51±0.31
	488475	4274880	13.79±0.33
	488499	4274800	11.41±0.32

488795	4274990	$20.09 \pm 0.12$	490180	4273310	$17.58 \pm 0.21$
488590	4274830	$5.90 \pm 0.17$	490186	4273340	$12.63 \pm 0.11$
488379	4274530	$5.10 \pm 0.15$	490198	4273380	$23.08 \pm 0.43$
488443	4274410	$2.68 \pm 0.13$	490194	4273400	$18.06 \pm 0.13$
488537	4273230	$32.87 \pm 0.15$	490158	4273480	$17.68 \pm 0.28$
488571	4273190	$28.87 \pm 0.16$	490189	4273570	$18.70 \pm 0.31$
488653	4273160	$33.31 \pm 0.20$	490197	4273640	$15.89 \pm 0.52$
488716	4273170	$33.71 \pm 0.29$	490206	4273710	$13.05 \pm 0.35$
488710	4273220	$33.13 \pm 0.28$	490268	4273790	$13.68 \pm 0.46$
488800	4273210	$32.62 \pm 0.32$	490191	4273820	$14.27 \pm 0.32$
488759	4273090	$33.61 \pm 0.34$	490121	4273850	$14.66 \pm 0.10$
488673	4273040	$29.92 \pm 0.31$	490030	4273960	$13.01 \pm 0.30$
488863	4272660	$27.55 \pm 0.10$	490007	4274030	$9.51 \pm 0.45$
489132	4272780	$28.60 \pm 0.34$	489738	4274190	$15.53 \pm 0.12$
489249	4272810	$22.32 \pm 0.23$	489683	4274220	$17.17 \pm 0.11$
489281	4272820	$26.53 \pm 0.33$	489622	4274340	$12.12 \pm 0.14$
489375	4272830	$21.53 \pm 0.46$	488560	4274060	$5.60 \pm 0.24$
489486	4272830	$25.26 \pm 0.46$	488499	4274050	$6.00 \pm 0.21$
489563	4272860	$20.21 \pm 0.48$	488474	4273980	$5.63 \pm 0.14$
489647	4272910	$23.20 \pm 0.21$	488468	4273880	$5.34 \pm 0.11$
489772	4272910	$20.86 \pm 0.30$	488485	4273830	$4.63 \pm 0.15$
489922	4272920	$21.32 \pm 0.17$	488497	4273810	$5.91 \pm 0.09$
490081	4273000	$21.64 \pm 0.10$	488399	4273790	$6.38 \pm 0.26$
490130	2473110	$18.55 \pm 0.57$	488388	4273750	$6.87 \pm 0.41$

488401	4273620	6.85±0.29	487897	4274060	10.22±0.49
488340	4273590	7.07±0.21	487936	4274110	8.76±0.17
488335	4273560	8.97±0.26	487933	4274150	10.36±0.41
488328	4273530	7.77±0.22	487967	4274140	8.97±0.32
488297	4273510	9.19±0.18	488056	4274150	7.81±0.57
488282	4273450	8.85±0.10	488074	4274190	6.97±0.34
488279	4273400	9.19±0.22	488153	4274200	6.45±0.33
488567	4273450	9.62±0.37	488244	4274240	7.56±0.23
488218	4273180	40.57±0.15	488405	4274230	4.15±0.35
488347	4273210	40.70±0.21	488216	4274400	17.30±0.15
487479	4272590	16.55±0.26	488190	4274470	9.90±0.44
487422	4272770	15.22±0.05	488011	4274480	6.16±0.28
487851	4272950	17.97±0.24	487943	4274530	6.22±0.27
487715	4272800	12.68±0.14	487863	4274600	5.83±0.11
487476	4273060	17.94±0.28	487798	4274410	8.82±0.22
487395	4273610	19.54±0.19	487683	4274380	10.90±0.36
487339	4273660	15.05±0.52	487624	4274320	10.12±0.44
487561	4273710	13.93±0.61	487562	4274250	8.39±0.22
487705	4273760	12.85±0.67			
487749	4273820	12.20±0.36			
487796	4273870	12.40±0.36			
487838	4273880	8.61±0.23			
487885	4273930	9.51±0.46			
487872	4273960	9.87±0.44			

---

Central Cedar Mountain Sill		
Easting	Northing	Thickness
489772 m	4274800 m	3.54±0.03 m
489756	4274790	3.61±0.04
489745	4274830	4.26±0.04

489724	4274850	4.10±0.16	489658	4275290	4.78±0.23
489887	4275310	9.61±0.11	489743	4275360	5.98±0.43
489875	4275360	9.77±0.30	489735	4275340	6.21±0.17
489863	4275370	9.25±0.22	489687	4275310	5.82±0.66
489840	4275400	9.38±0.25	489845	4275290	8.57±0.20
489816	4275420	8.84±0.02	489814	4275280	8.38±0.14
489781	4275390	7.52±0.42	489798	4275280	7.08±0.17
490174	4275590	12.02±0.08	489712	4274920	5.26±0.18
490174	4275530	13.22±0.10	489663	4275020	5.62±0.17
490193	4275440	15.53±0.12	490165	4275500	14.55±0.31
489688	4275050	5.27±0.13	490170	4275450	14.87±0.10
489664	4275000	4.73±0.16	<hr/>		
489710	4275120	5.37±0.21	<b>Razor's Sill</b>		
489640	4275050	4.47±0.29	Easting	Northing	Thickness
489538	4275060	2.71±0.33	489464 m	4279070 m	5.7±0.11 m
489557	4274990	2.20±0.14	489511	4279040	7.78±0.18
489560	4274960	2.23±0.38	489580	4279030	7.25±0.08
489808	4275280	7.85±0.20	489644	4279040	7.78±0.10
489784	4275280	6.49±0.16	489710	4279060	5.81±0.11
489753	4275300	6.32±0.13	489431	4279180	6.33±0.15
489731	4275290	5.75±0.09	<hr/>		
489710	4275290	5.28±0.26	<b>Hebes Sill</b>		
489691	4275290	5.52±0.22	Easting	Northing	Thickness
489678	4275300	5.72±0.15	490593 m	4281090 m	22.58±0.16 m

490439	4281670	33.34±0.42	489089	4282980	21.65±0.47
490194	4281800	36.08±0.10			
<hr/>					
490290	4282640	22.49±0.15	<b>Bad Luck Sill</b>		
489926	4283040	24.07±0.32	Easting	Northing	Thickness
490078	4282910	23.27±0.36	492071 m	4280530 m	14.37±0.17 m
489565	4282890	26.61±0.18	492785	4281840	15.32±0.12
489110	4282970	19.77±0.21	491954	4282470	5.64±0.43
489020	4281990	20.72±0.20	491820	4282330	4.81±0.20
489234	4281740	20.80±0.23	491866	4281720	9.18±0.21
489558	4281520	27.48±0.34	491892	4281580	7.93±0.25
489651	4281450	27.57±0.31	492152	4281560	14.03±0.39
489786	4281510	30.38±0.30	492342	4281530	16.49±0.38
489736	4281390	22.64±0.34	492560	4281370	13.22±0.26
488987	4282060	27.73±0.14	492275	4281140	12.17±0.29
489096	4282650	21.33±0.29	493087	4280750	13.74±0.26
489359	4282650	28.24±0.29	492940	4279650	8.36±0.32
489453	4282720	25.33±0.14	492126	4280950	9.93±0.33
489550	4282630	27.77±0.23	492137	4280900	11.57±0.36
489668	4282820	27.80±0.41	491933	4281870	8.93±0.34
489568	4282900	27.01±0.35	491641	4280720	11.42±0.27
489258	4283240	4.51±0.30	491537	4280690	15.79±0.14
489242	4283260	3.50±0.35	491753	4280270	13.25±0.30
489228	4283290	7.30±0.29	492071	4280530	14.92±0.21
489196	4283310	7.55±0.64	491643	4279230	13.02±0.14

491651	4279010	15.66±0.18	491811	4280510	15.74±0.20
491713	4277980	12.82±0.17	492272	4279960	13.22±0.12
490865	4276750	6.83±0.15	<hr/>		
490225	4277030	4.03±0.05	<b>Lower Cedar Mountain Sill</b>		
493252	4280230	13.43±0.34	Easting	Northing	Thickness
493172	4280160	7.45±0.21	490227 m	4273100 m	1.26±0.13 m
492669	4280700	12.08±0.08	490230	4273180	6.82±0.19
492551	4279610	6.69±0.14	490256	4273170	2.26±0.23
492524	4279280	5.21±0.29	490263	4273190	0.76±0.08
492128	4279400	15.28±0.07	490320	4273420	9.44±0.26
491851	4279510	7.65±0.21	490345	4273440	9.19±0.22
491703	4279430	17.32±0.07	490302	4273460	10.71±0.35
493311	4281320	18.52±0.36	490272	4273490	12.09±0.41
492541	4281830	12.38±0.11	490327	4273530	8.57±0.20
492404	4282010	12.20±0.24	490350	4273560	6.32±0.43
492346	4281630	18.96±0.17	490372	4273620	10.26±0.16
492205	4281770	15.35±0.14	490319	4273650	12.62±0.14
491840	4281090	9.69±0.16	490353	4273680	12.53±0.44
491876	4281420	11.09±0.17	490408	4273730	10.52±0.13
491871	4281260	8.46±0.28	490436	4273750	9.95±0.35
491663	4281150	9.22±0.20	490401	4273800	8.95±0.23
491860	4280990	11.12±0.27	490441	4273870	12.06±0.20
491907	4280870	11.53±0.19	490475	4273920	11.19±0.20
491808	4280780	12.79±0.28	490469	4273930	13.32±0.18

490200	4274110	12.37±0.45
490151	4274140	13.21±0.16
490136	4274160	7.59±0.25
490113	4274160	14.43±0.45
490093	4274180	10.50±0.45
490073	4274200	5.39±0.19
490083	4274210	3.20±0.15
489974	4274220	10.40±0.36
489997	4274230	4.38±0.26
490019	4274240	2.85±0.16
490204	4273060	1.88±0.24

---

\* Eastings and northings reported in  
UTM Zone 12 coordinates.

## **2. Validating Lava Flow Simulators using a Validation Hierarchy and Bayesian Analysis**

### **Abstract**

Modeling lava flows through cellular automata (CA) methods enables a computationally inexpensive means to quickly forecast lava flow paths and ultimate areal extents. A CA program has been created in the program language C that is modular, which enables a combination of governing CA rules to be evaluated against each other. My objective is to find a successful combination of automata behaviors that behaves like a bingham fluid and accurately forecasts lava inundation. To fulfill this objective, four validation levels have been devised, into which different benchmarks can be applied to test lava spreading algorithms against increasingly complex tests. These levels are 1) verification of the code by testing for conservation of mass; 2) testing for flow self-similarity given inconsequential variations in input parameters; 3) testing for replication of Bingham flow morphology on simple surfaces; and 4) testing for replication of real lava flow morphologies on pre-eruption elevation models. Two Bayesian posterior statistics  $\text{Pr}(Lava|Sim)$  and  $\text{Pr}(\neg Lava|\neg Sim)$  are then used to further characterize model performance against the 2012-3 Tolbachik lava flow. These metrics can provide insight into improving model performance and decision making in volcanic crises.

### **2.1 Introduction**

Lava flows as a gravity current on the surface of the Earth when liquid magma is effused at the surface with little or no explosivity. In the vicinity of active volcanoes, lava flows represent significant long term impact to infrastructure (Peterson and Tilling, 2000). In the past, lava flow hazard has been mitigated with the construction of physical diversions

and at least once in 252 A.D. by the supernatural grace of St. Agatha of Sicily who died the year prior. Modern science suggests, however, that forecasting the flow path of lava from active volcanoes might be more useful than St. Agatha for communities impacted by effusive volcanism.

Methods of forecasting lava flows range from simple predictions using empirical relationships between magma flux and flow length (Glaze and Baloga, 2003), to 1-D numerical solutions such as FLOWGO (Harris and Rowland, 2001), to advanced computational fluid dynamics codes like lavaSIM (Hidaka et al., 2005). All modern numerical flow models by nature trade precision in simulating physical processes with computer run-time, so that while FLOWGO is relatively fast it only predicts downslope flow length, while lavaSIM solves Navier-Stokes equations to produce a 3-D flow distribution at the expense of large computational requirements.

Cellular Automata (CA) methods have been developed to simulate fluid flow, including lava spreading (Barca et al., 1994). In contrast to CFD codes, these do not generally attempt to compute Navier-Stokes equations but instead abstract many physical parameters, such as viscosity and temperature, into more or less empirical rules. The benefit of CA methods for simulating lava flows is most noticeable in the reduced computer time necessary for simulation compared to CFD methods.

Multiple CA lava flow algorithms exist, such as SCIARA (Crisci et al., 2004), MAGFLOW (Del Negro et al., 2008), ELFM (Damiani et al., 2006), and LavaPL (Connor et al., 2012). These algorithms are variations on a theme, where the largest difference between each is how lava is distributed from one automaton to its neighbors. For instance, three versions of SCIARA allow for lava to spread in cardinal directions (Barca et al., 1994), in hexagonal directions (Crisci et al., 2008), or in directions based on an inherent velocity calculated in an eulerian way for each automaton (Avolio et al., 2006). MAGFLOW and ELFM by contrast to the original SCIARA algorithm implements 8 directions of spreading.

LavaPL and SCIARA both spread in four directions but the apportionment of lava from one automaton to neighbors is based on a different algorithm.

While several lava flow simulators now exist, each have been made and tested with different lava flows or aspects of flows in mind. Because of this, selecting a specific algorithm to effectively model lava flow hazards can be a necessary, if unwanted challenge. To address this problem, we propose a hierarchical validation scheme to objectively test different flow spreading algorithms. Benchmark tests can be designed with different validation levels in mind, to compare lava flow simulations to increasingly complex models, from simply conserving mass to replicating the paths and ultimate areal extents of real lava flows. The benchmarks described in this project can be applied to any flow algorithm that provides at least a list or map of inundated locations over various topographies.

In this paper, multiple lava flow algorithms are tested using a new modular lava flow code, which I have named MOLASSES (standing for *MOdular LAvA Simulation Software in Earth Science*). This code, implemented in C, is a Cellular Automata code which tracks a population of equal-area spaced cells over a grid, that is defined by a digital elevation model (DEM). These cells may or may not be inundated with lava and they are governed by universal rules. Because MOLASSES has been designed in a modular way, it is relatively quick to modify the flow algorithm. Using this code while changing methods of lava distribution enables code output in a constant format, which simplifies the comparison of methods.

In Section 2.2, I will demonstrate how CA is applied to lava flows and detail how a CA simulation is carried out in the MOLASSES code. I will introduce a validation hierarchy in Section 2.3 that can be used to verify and validate different lava flow algorithms using increasingly complex model parameters. In Section 2.4, I will expand on the final validation level (validation against real lava flows) with a Bayesian approach to improving model performance for the 2012-3 Tolbachik Lava Flow. The results from these Sections will be discussed in Section 2.5.

### 2.1.1 Case Study Area: 2012-3 Tolbachik Lava Flow

In the third validation level (Section 2.3.4), the recent lava flows at Tolbachik will be used as an example benchmark test to validate flow algorithms against a real lava flow. These flows will then be used in Section 2.4 as examples of how a Bayesian approach to evaluating model performance can improve model performance.

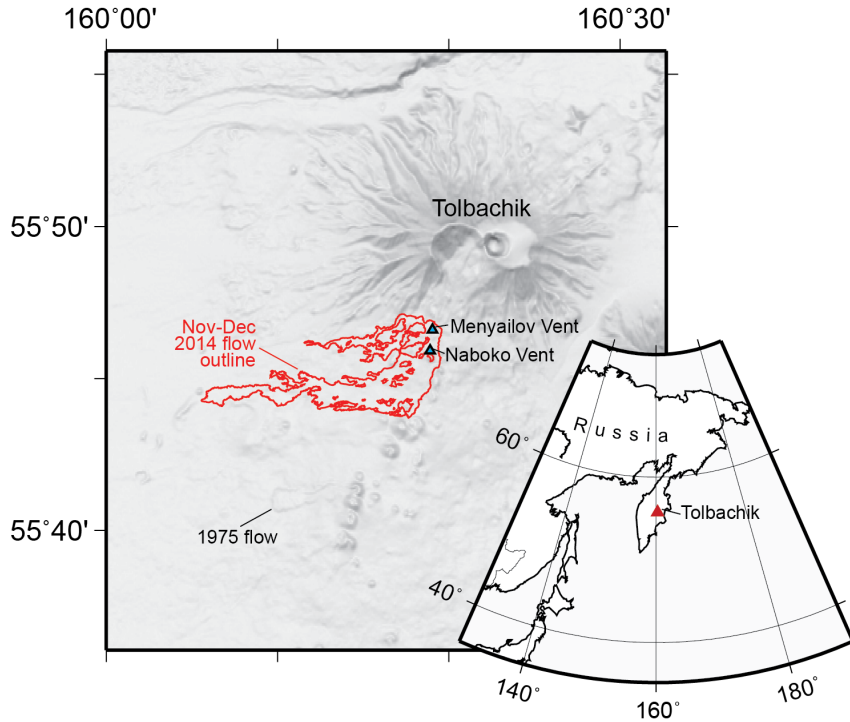


Figure 2.1: The Tolbachik region of Kamchackta, Russia. The two main vents are shown as triangles and the outline of western lava flows, emplaced in 2014, is drawn in red.

The Tolbachik lava flow began in November 2012, originally being sourced from a long fissure vent south of Tolbachik Dol. Initial magma flux was estimated to be  $440 \text{ m}^3 \text{ s}^{-1}$  (Belousov et al., 2015). The fissure vent ultimately coalesced into two main vents, seen in TanDEM-X interferometric synthetic aperture radar (InSAR) data (Kubanek et al., 2015), and the flux dropped significantly to between  $100$  and  $200 \text{ m}^3 \text{ s}^{-1}$ . Early stages of the flow carried lava west to a maximum runout of 14.5 km and later stages beginning in January or February, carried lava east. The total emplacement volume is  $\sim 0.53 \pm 0.07 \text{ km}^3$  with  $0.38 \text{ km}^3$  of that being to the west. TanDEM-X InSAR data has been used to show that the

modal thickness of the flow is 7.8 m, and that the overall thickness distribution is log-normal (Kubanek et al., 2015). After the flow ceased, the total emplacement area was mapped using orthophotos and TanDEM-X data where clouds were present in the images by Kubanek et al. (2015).

Figure 2.1 shows the outline of the early lava flows, which traveled from two vents along a fissure to the west. This areal extent will be used to validate lava flow simulators. The flow volume is taken to be the total emplacement area within this outline,  $26 \text{ km}^2$ , multiplied by the observed modal thickness of the flow, 7.8 m. The total flow volume used the input parameter in the flow simulations will be  $0.22 \text{ km}^3$ . The remainder of the total emplacement volume to the west of the vents,  $0.16 \text{ km}^3$  is interpreted to be material that built near-vent edifices (e.g. cones) (Kubanek et al., 2015). The volume interpreted to be emplaced from the northern vent is  $4.63 \times 10^7 \text{ km}^3$ , while the southern vent volume is  $1.74 \times 10^8 \text{ km}^3$ . This estimate was made by splitting the flow between areas north of the Menyailov (northern) vent and south of it, assuming that flows from the Menyailov vents traveled north.

## 2.2 A Modular Cellular Automata Algorithm for lava flows

CA in lava flows has historically been defined as a 2-dimensional space, which is divided into equal-area grid cells, such as those found in a common digital elevation model (DEM). Within the location of each cell is defined an “elementary automaton” (*ea*) that has a set of properties, is governed by a set of global rules, and has a set list of neighboring automata. While the behavior rules that each *ea* follow is identical to those of all other automata, its behavior is only dictated by local phenomena. Specifically, the amount of lava that flows in or out of an *ea* will depend on properties such as lava thickness and elevation within it and its neighbors. Because grid cells and *ea* are fundamentally inseparable in this application, I will refer to *ea* as cells.

The set of cellular automata is defined as

$$\mathbf{A} = \{E^2, V, S, X, \sigma, \gamma\} \quad (2.1)$$

where  $E^2$  is the set of point locations of cells in  $\mathbf{A}$ ,  $V \subset E^2$  is the set of vent or source locations,  $S$  is the set of substates within each cell, and  $X$  is the local neighborhood that each cell can directly influence (Barca et al., 1994).  $\sigma$  and  $\gamma$  represent the transition functions and source functions within  $\mathbf{A}$ .

Practically,  $E^2$  is a set of coordinate pairs denoting row and column addresses of cells in a larger grid.  $S(i,j)$ , which represents the set of substates for the cell at row  $i$ , column  $j$ , includes  $S_e$ , the underlying elevation of an automaton;  $S_h$ , the thickness of lava within the cell; and  $S_{h0}$ , the critical thickness, above which lava will spread from a cell. Some algorithms include  $S_T$ , or the cell temperature in this set.  $X$ , in a four-connected neighborhood scheme, is given as  $\{(0,1), (0,-1), (1,0), (-1,0)\}$ , where  $(0,0)$  is the location of a cell under evaluation.  $\sigma$  is the change of substates in  $S$  for each cell from timestep  $t$  to  $t + 1$ , or  $S^t \rightarrow S^{t+1}$ .  $\gamma$  specifies the lava emitted at locations within  $V$ . The implementation of these sets within the CA structure  $\mathbf{A}$  is described in detail below.

### 2.2.1 MOLASSES Algorithm Outline

MOLASSES is a Cellular Automata code developed in the C programming language based on the CA algorithm “LavaPL” of Connor et al. (2012). The major change between LavaPL and MOLASSES is that MOLASSES is constructed with nine modules that each have a specific task, either carrying out the CA simulation, reading model input, or writing model output (Figure 2.2). The nine modules were designed to replicated major functions in LavaPL and are:

1. **DRIVER** Calls modules in sequence to execute the flow algorithm.
2. **INITIALIZE** Reads a user-provided configuration file to define model parameters.

3. **DEM\_LOADER** Imports a raster file to define the elevation model.
  4. **INITFLOW** Uses model parameters to define data arrays.
  5. **PULSE** Incrementally adds lava to source locations.
  6. **DISTRIBUTE** Determines whether to spread and how to spread lava between cells.
  7. **NEIGHBOR\_ID** Identifies the cell neighborhood.
  8. **ACTIVATE** Adds newly inundated cells to the list of active cells.
  9. **OUTPUT** Writes model results to a file using user-specified formats.

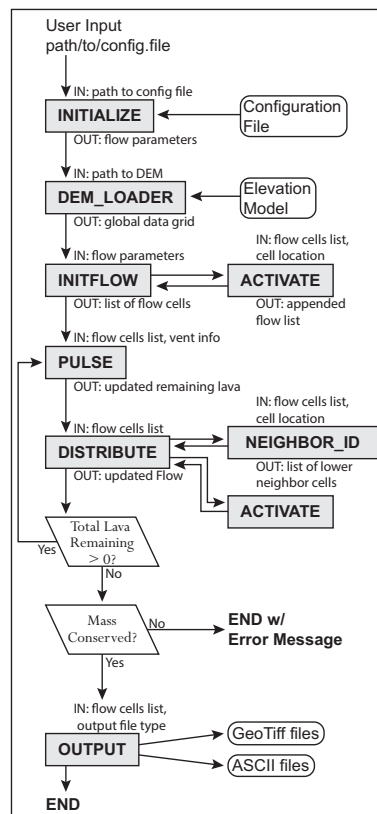


Figure 2.2: A flow chart of MOLASSES carried out within the **DRIVER** module. Gray boxes denote various modules, with major inputs and outputs given above and below. Parallelograms are checks performed within DRIVER itself. Rounded boxes represent external input and output files.

Like LavaPL, model parameters are specified by a user through a text configuration file, which must include 1) a digital elevation model (DEM), 2) a residual lava flow thickness, 3) at least one vent location, 4) the total volume and “pulse volume” of this vent, and 5) an output file path. The lava flow thickness defines the CA value of  $S_{h0}$ , where cells with flow thicknesses  $S_h > S_{h0}$  will spread all lava to their neighboring cells, while cells with less lava will retain their lava. The “pulse volume” defines  $\gamma$  and the amount of lava to emit at the source location at each time step. The total volume constrains  $\gamma$  as lava will not be introduced to the source location after the total volume has been delivered. Modules within MOLASSES that further execute the CA simulation are detailed below.

### 2.2.2 Cells in $E^2$

Information for cells in the grid defined by  $E^2$  is stored in two ways, for code efficiency. First, some information of the CA structure **A** is stored in a Global Data Grid. This grid stores information known at the beginning of the simulation, such as the user supplied residual flow thickness and the elevation. Grid dimensions are set in the **DEM\_LOADER** module to be identical to the user-specified raster DEM. This module then imports the elevation of each raster pixel into the corresponding grid cell location. After this operation, the residual flow thickness is also stored in the grid.

The second information storage method is a list defined in the **INITFLOW** module. The “Active List” is declared with a length that corresponds to the theoretical maximum number of cells that can be inundated by lava. This list contains data that is updated during the simulation, including lava thicknesses,  $S_h$ , within cells. As cells are determined within the simulation to be inundated with lava for the first time, their row and column addresses, as well as their lava thicknesses are appended to the Active List with the module **ACTIVATE**.

### 2.2.3 Source Locations, $V$ , and the Source Function, $\gamma$

Initially in the Active List, **INITFLOW** only declares source location(s) as the first few elements of the list. These source locations are flagged in the list to be identified as source locations by other modules.

The **PULSE** module carries out the source function,  $\gamma$ . In this module, a separate array stores each source vent's volume parameters. The pulse volume is added to the quantity of lava in the source cell and is subtracted from the remaining volume. The remaining volume is initially set as the total volume given in the configuration file, so **PULSE** continues to add lava to the source locations at each time step until remaining volume is 0.

### 2.2.4 Substates, $S$ , and the Transition Function, $\sigma$

Substates which cannot change, such as the cell elevation  $S_e$  and the residual flow thickness  $S_{h0}$ , are stored within the Global Data Grid. Substates which do change, primarily flow thickness,  $S_h$ , are stored in the Active List and are allowed to change from timestep to timestep. These values are initialized in **INITFLOW** where thicknesses are set to 0.

The transition function,  $\sigma$ , is defined in the **DISTRIBUTE** module. Cells in this module are evaluated in order of their inundation (i.e. vents are evaluated first and distal cells are evaluated last). The incoming and outgoing quantity of lava from each cell is stored in the Active List. Generally, if a cell has a flow thicknesses  $S_h > S_{h0}$ , it will spread the lava above  $S_{h0}$  to any neighbors lower in elevation than itself. When all inundated cells have been evaluated, the incoming and outgoing quantities of lava of each cell are applied to the cells. This flow transition represents a timestep as all cells are updated at once.

Multiple possible transition functions can effectively spread lava from and to cells in a manner that might replicate lava in real life. Selecting the best transition function is the purpose of the validation benchmarks described in Section 2.3. In this project three main variations are combined and tested which vary 1) how local slope affects spreading, 2) the

neighborhood size, and 3) if any neighbors are eliminated from the neighborhood based on their relationship to the cell.

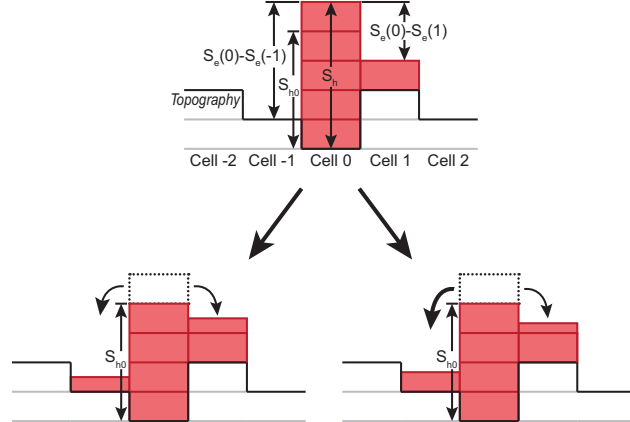


Figure 2.3: A 2-D example of two transition functions. At timestep  $t$  (top), Two cells are inundated with lava. The central cell (Cell 0) has 1 block of lava higher than the residual thickness,  $S_{h0}$ . In a slope-proportional sharing scheme, timestep  $t + 1$  will follow the path to the right; because Cell -1 has twice the relief as Cell 1, it receives twice as much of the residual lava (2/3 blocks vs. 1/3 to the right). In an equal-sharing scheme, the left path will be followed, and half the block will be added to both neighbor cells.

**2.2.4.0.1 Local slope-based spreading** In the LavaPL algorithm given by Connor et al. (2012), lava is apportioned from cells to their neighboring cells proportional to slope. To give a specific case, let a cell at location  $c$  be the central cell, with a set of neighbor cells,  $X$ . The total relief between cell  $c$  and its lower neighboring cells is

$$TR(c) = \sum_{n \in X} (S_h(c) + S_e(c)) - (S_h(n) + S_e(n)) \quad (2.2)$$

where  $S_h$  is the height or thickness of the lava in a cell,  $S_e$  is the underlying elevation of the cell, and  $n$  is a neighbor in  $X$ . The total lava to spread away from the central cell is the difference between thickness of lava ( $S_h$ ) at  $c$  the residual thickness ( $S_{h0}$ ), unless the lava

thickness is lower than the residual thickness, giving

$$\text{Outbound}(c) = \begin{cases} S_h(c) - S_{h0}(c) & \text{if } S_h(c) - S_{h0}(c) > 0 \\ 0 & \text{if } S_h(c) - S_{h0}(c) \leq 0 \end{cases} \quad (2.3)$$

In LavaPL, the excess flow, “Outbound”, is delivered to neighbors  $n$  based on the proportion of total relief, TR, found at each neighbor location (the right path of Figure 2.3). For each  $n \in X$ ,

$$\text{Inbound}(n) = \text{Outbound}(c) \left( \frac{(S_h(c) + S_e(c)) - (S_h(n) + S_e(n))}{\text{TR}} \right) \quad (2.4)$$

This is the slope-proportional spreading equation. Another method would be “slope-blind,” and would spread lava to all lower neighbors equally following the equation

$$\text{Inbound}(n) = \left( \frac{\text{Outbound}(c)}{|X|} \right) \quad (2.5)$$

where  $|X|$  is the size of the neighborhood, or the number of elements in the neighborhood. This is illustrated as the left path of Figure 2.3.

**2.2.4.0.2 Neighborhood size** The size of the neighborhood,  $X$ , in CA algorithms is commonly 4 or 8 in cardinal or ordinal directions. Here both have been implemented, which enables the benchmarks to test whether 8 spreading directions increases the performance of these tests. This is further described in the next section (2.2.5).

**2.2.4.0.3 Spreading inhibited by special relationships** Though the size of the neighborhood is set globally for all cells, neighbors are not guaranteed to receive lava from central cells. In all algorithms, for example, cells in the neighborhood that are higher than the central cell, including lava thicknesses, are excluded from the neighborhood set.

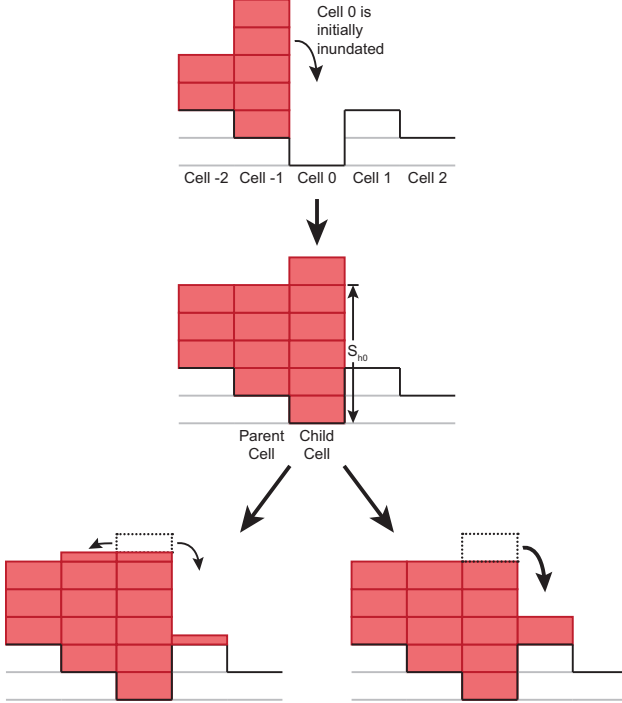


Figure 2.4: Another 2-D example of different transition functions. In the first timestep (top), Cell -1 initially inundates Cell 0, creating the Parent-Child relationship shown in the next illustrated timestep (middle). If Parents cannot receive lava from Child cells, all residual lava in Cell 0 will flow to Cell 1, following the path to the right. If these relationships are ignored, as shown in the left path, Cell 0 will spread lava in both directions.

Other neighbor elimination rules can also be implemented. One has been designed by Connor et al. (2012), where the cell that initially gives lava to another cell is forever eliminated from the receiving cell’s neighborhood. This is done by creating a “parent-child” relationship for each activated cell in the flow. Simply put, child cells cannot give lava to their parent cells (right path in Figure 2.4). This transition function rule is tested against no parentage rules in competing MOLASSES algorithms (left path in Figure 2.4).

### 2.2.5 Cell Neighborhood, X

The final set in the CA is the cell neighborhood  $X$  and is defined by the **NEIGH-BOR\_ID** module. This neighborhood is usually either 4-connected (von Neumann neighborhood) or 8-connected (Moore neighborhood) as illustrated in Figure 2.5. Four-connected neighborhoods are defined as the row, column coordinates  $\{(0,1), (0,-1), (1,0), (-1,0)\}$ , where

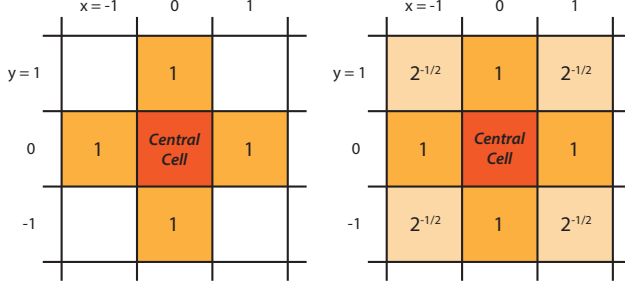


Figure 2.5: Cellular Automata neighborhoods. To the left, in a 4-connected neighborhood, a central cell may influence or be influenced by cells in cardinal directions. To the right, in an 8-connected neighborhood, the zone of influence is expanded to include ordinal directions. Numbers in each cell are relative weights (determined by distance from the central cell), so diagonal neighbors are weighted less than orthogonal cells.

(0,0) is the location of a cell under evaluation, while the set elements might correspond to North, South, East, and West. Eight-connected neighbors include the ordinal directions, Northeast, Southeast, Northwest, and Southwest:  $\{(0,1), (0,-1), (1,0), (-1,0), (1,1), (-1,1), (1,-1), (-1,-1)\}$ .

NEIGHBOR\_ID is implemented within the DISTRIBUTE module to evaluate cells within X, and determine whether they are lower in elevation (including their lava) than the central cell. If one is lower, NEIGHBOR\_ID returns their relief, or the difference in elevation between the cell and the central cell, to the DISTRIBUTE module. Depending on whether parent-child relationships are recorded or ignored in the transition function, NEIGHBOR\_ID can follow one of two algorithms below.

---

<b>4-connected NEIGHBOR_ID module</b>	<b>8-connected NEIGHBOR_ID with Parent-Child Relationships</b>
$X = \{(0,1), (0,-1), (1,0), (-1,0)\}$	$X = \{(0,1), (0,-1), (1,0), (-1,0), (1,1), (-1,-1), (1,-1), (-1,-1)\}$
$X' = \{\}$	$X' = \{\}$
$c = (0,0)$ (central cell location)	$c = (0,0)$ (central cell location)
<b>For</b> $n \in X$	<b>For</b> $n \in X$
<b>If</b> $(S_h(c) + S_e(c)) - (S_h(n) + S_e(n)) > 0$	<b>If</b> $(S_h(c) + S_e(c)) - (S_h(n) + S_e(n)) > 0$
<b>Append</b> $n$ to $X'$	<b>If</b> $n$ is <b>not</b> Parent of $c$
	<b>Append</b> $n$ to $X'$
<b>Return</b> $X'$	<b>Return</b> $X'$

---

### 2.3 Benchmarking Hierarchy

The strategy implemented in this paper follows the advice of Bayarri et al. (2007) for validating computer models, namely “1) defining the problem; 2) establishing evaluation criteria; 3) designing experiments; 4) approximating computer model output; 5) analyzing the combination of field and computer run data.” The sixth step in their validation process, feeding results back to revise models, has been done informally to determine how to alter spreading algorithms in future benchmarking attempts. Each level below presents a problem for a lava spreading algorithm to complete. These fundamental problems (e.g. replicating a Bingham flow) are evaluated using simple tests that demonstrate the problem. The relevant model output for each of these tests is a list of locations (i.e. a list of x and y coordinates) that have been inundated by lava. After verification (Level 0), the first validation level tests model results with other model results; the second level tests model output against expected analytical solutions; and the third level tests model output from field data.

Table 2.1: Transition Algorithm Codes and Descriptions

Transition Function	Neighborhood	Parent-Child Relationships Preserved?	Slope-proportional Sharing?
<b>4/P/S</b>	4-directions	Yes, “parents” do not accept lava from “children.”	Yes, lower cells receive lava based on relative relief.
<b>8/P/S</b>	8-directions	Yes	Yes
<b>4/N/S</b>	4-directions	No, “parents” are not defined.	Yes
<b>8/N/S</b>	8-directions	No	Yes
<b>4/P/E</b>	4-directions	Yes	No, all lower cells receive equal quantities of lava.
<b>8/P/E</b>	8-directions	Yes	No
<b>4/N/E</b>	4-directions	No	No
<b>8/N/E</b>	8-directions	No	No

**2.3.0.0.4 Test Algorithms** Combining three variations of the Transition Function described in Section 2.2, I have created eight MOLASSES lava flow algorithms. Each variation has been made by modifying one module in the MOLASSES framework: The neighborhood is changed between 4- and 8- directions using the NEIGHBOR\_ID module, classifying one cell as a “parent” cell when a location is initially inundated is within the ACTIVATE module, and dividing lava amongst neighboring cells proportional to slope or equally is carried out in the DISTRIBUTE module. These eight algorithms will be referred to using three character codes, listed in Table 2.1. For the algorithm used by LavaPL in Connor et al. (2012), the code would therefore be 4/P/S, as it spreads lava in 4-directions from a central cell, all inundated cells have designated parents to whom they cannot spread lava, and the quantity of lava to spread from a central cell is higher for lower neighboring cells.

### 2.3.1 Level 0: Conservation of Mass

Before the results of a lava flow simulation can be validated, it must be verified to at least prove that conservation of mass is preserved. A lava flow simulation will therefore not be tested against the following benchmark tests until this conservation of mass requirement is shown to be fulfilled.

In MOLASSES, the code is verified within the DRIVER module, which manages each subordinate module. The erupted volume,  $V_{in}$ , is given as the total eruption volume specified by the user in the configuration file. If multiple source locations are given in this file,  $V_{in}$  is the sum of total eruption volumes.  $V_{in}$  is compared at the end of the module to the total volume of the flow, or  $V_{out}$ . The volume  $V_{out}$  is calculated by summing the volume in all inundated grid cells. MOLASSES reports success if  $V_{in} - V_{out} \leq 10^{-8} \text{ m}^3$ , which is the precision of a 64-bit double. If this test fails, MOLASSES reports failure and the excess volume found in the flow.

---

### MOLASSES Conservation of Mass Test

---

**If**  $|V_{in} - V_{out}| \leq 10^{-8}$

**Print** SUCCESS: MASS CONSERVED

**Else**

$excess = V_{out} - V_{in}$

**Print** ERROR: MASS NOT CONSERVED! Excess:  $excess \text{ m}^3$

---

### 2.3.2 Level 1: Repeatability given meaningless parameter variation

Once the code has been verified to conserve mass, the flow can be validated. This first validation level tests that lava flow simulations are repeatable, regardless of changes in parameter space that should have no effect on the flow. Parameters that ideally should not effect lava flows include slope direction and elevation model resolution. For instance, a slope to the west and an identically dipping slope to the east should produce lava flows of equal length and shape (given identical flow attributes).

Miyamoto and Sasaki (1997) performed a simple validation test on two CA-like flow simulators (Ishihara et al., 1990; Miyamoto and Sasaki, 1997) where a sloped DEM was rotated 45 degrees from “south” to “southeast”. This benchmark was performed to demonstrate that the flow models had the same run-out length regardless of the arbitrary slope direction. Here, the DEM rotation scheme by Miyamoto and Sasaki (1997) is adopted and

expanded, so that a DEM of a simple slope is rotated 19 times at increments of  $5^\circ$ . Flows are simulated on each of these slopes and the locations of inundated cells are output from the model.

Three characteristics of the simulated flows are determined for each slope direction: flow length, orientation, and aspect ratio. Flow length is defined as the distance between the vent and the furthest inundated point from the vent. Flow orientation is defined as the direction that furthest point lies, with respect to North. Flow aspect ratio is the ratio of maximum flow width to flow length. Perfect success for this benchmark is when simulated flows, regardless of slope direction, 1) do not change in length, 2) have an orientation identical to the slope direction, and 3) do not change in aspect ratio. Failure is more subjective, but I will define failure as 1) more than 10% variation in flow length depending on slope direction, 2) more than  $5^\circ$  offset between the slope and the flow orientation on average, or 3) more than 15% variation in flow aspect ratio.

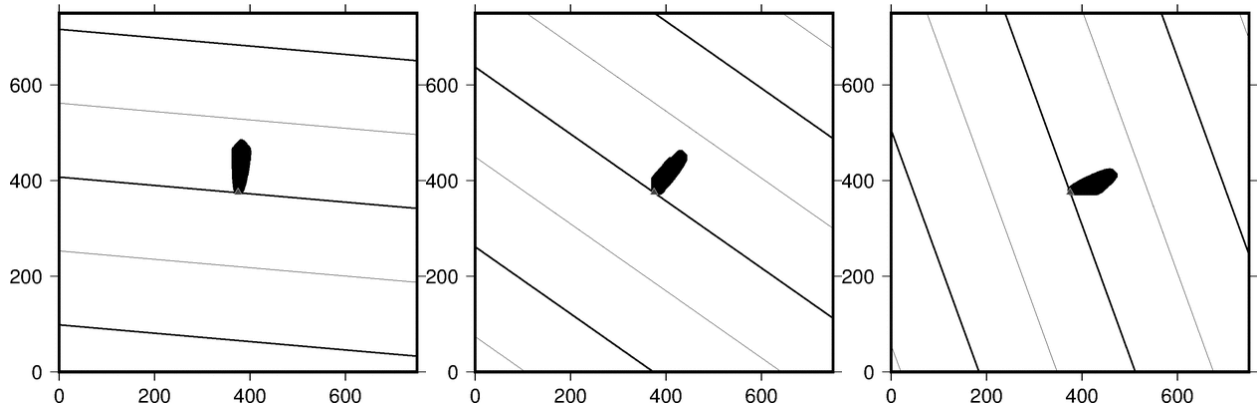


Figure 2.6: Rotating slope test for algorithm 4/P/S (LavaPL). Slope dip is  $18^\circ$ , with dip-directions 0N, 30N, and 80N from left to right. The flow length and aspect ratio are similar and the flow direction is in the slope direction, so it passes Level 1 criteria.

### 2.3.2.1 Benchmark Parameters

The underlying DEM for this benchmark has a simple  $18^\circ$  slope, dipping to the North. The DEM has a spatial resolution of 1 m. The source cell is placed at the center of the DEM, is given a total volume of  $1000 \text{ m}^3$ , and is given a pulse volume of  $1 \text{ m}^3$ . When the simulation

is finished, model output is used to determining the three flow characteristics used in this benchmark (length, orientation, and aspect ratio). The DEM is rotated 5° clockwise and the process is repeated 19 times until the flow is simulated on an East-facing slope.

### 2.3.2.2 Results

For all eight flow algorithms, flow length, aspect ratio, and orientation were calculated 19 times, corresponding to the 19 dip directions sampled between 0°N and 90°N. Variance for length and aspect ratio were calculated as the ratio of their standard deviations to their means. For instance, if mean runout length for the 18 flows is 100 m and the standard deviation of the 18 lengths is 2 m, the runout length variance is 2%. The mean direction error is also calculated for the set of flows from each algorithm. These are reported in the table below.

DEM Rotation Results			
Transition Function	Run-out Variance	Aspect Ratio Variance	Mean Direction Error
4/P/S	2.7%	6.7%	1.2°
8/P/S	4.4	12.2	0.9
4/N/S	9.6	19.7	1.3
8/N/S	3.9	7.5	0.6
4/P/E	21.6	38.6	14.2
8/P/E	7.2	13.8	5.4
4/N/E	21.6	38.7	14.1
8/N/E	7.2	13.8	5.5

While with an ideal spreading algorithm, variances and direction error would be 0 under a rotating slope, every spreading algorithm tested performed differently as DEM direction changed. Following from the above pass-fail standards, five of the eight algorithms

can be rejected. Algorithms 4/P/E and 4/N/E have high run-out length variance. Algorithms 4/N/S, 4/P/E and 4/N/E have large aspect-ratio variance. Algorithms 4/P/E, 8/P/E, 4/N/E, and 8/N/E all systematically deviate from running downslope by  $> 5^\circ$  on average. This implies that algorithms which share lavas equally from central cells to all lower neighboring cells perform worse than algorithms which share lavas proportional to slope.

For the eight different transition functions tested, runout length varied between 60–160 m. The flow algorithm with the least flow length variance was the 4-connected, parent-child, slope-proportional strategy implemented in LavaPL. Algorithms 4/P/S (LavaPL), 8/P/S, and 8/N/S cannot be rejected because of any of the three standards set in this benchmark.

### 2.3.3 Level 2: Replication of flow morphologies on simple physical surfaces

The second benchmarking level is the first step in validating lava flow algorithms against realistic flow expectations. Instead of parameter space being arbitrarily defined, which was the case in Level 1, the defined parameter space informs tests at this level as to what the model output should be. As lava flows on a large scale are well described as Bingham fluids, simulations can be tested against analytical solutions or experimental observations of these fluids in simple conditions. For instance, a lava flow on a perfectly flat surface might be expected to create a circular areal extent (Griffiths, 2000).

Here I measure flow algorithm performance on a flat surface from a single vent source location. To measure the extent to which the simulated flow replicates a circle, the inundated area is compared to the area of a circle which circumscribes the flow exactly. This can be described as

$$Fit = \frac{A_{flow}}{\pi d_{max}^2} \quad (2.6)$$

where  $d_{max}$  is the farthest extent of the simulated flow from the vent. A perfect match to a circle would result in a  $Fit = 1$ . With the same maximum distance from the vent (i.e. the

distance from the center to a vertex) a perfect square would cover 64% of the area of a circle, ergo  $Fit = 0.64$ . An octagon would have a fit of 0.90. We consider a model to successfully pass this test if it produces a flow of  $Fit > 0.90$ , or if the flow approximates a circle better than an octagon. The model unambiguously fails this test if it produces a flow of  $Fit < 0.64$ , where a square better describes a circle than a flow generated from the model.

### Circular Flow Test

- 
- |            |  |
|------------|--|
| Fit = 1.0  | Best Possible Score; perfectly circular. |
| Fit > 0.90 | Success; better than an octagon.         |
| Fit < 0.64 | Failure; worse than a square.            |
- 

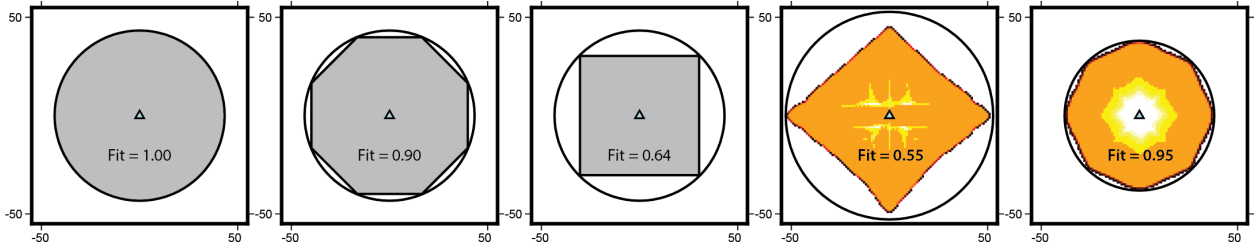


Figure 2.7: Fitness scores of different shapes. From left to right: A circle has a perfect fit score of 1.00; an octagon has 0.90 times the area of a circumscribing circle; a square has a score of 0.64; Two flat surface tests for slope proportional spreading algorithms with parent rules. The flow second to the right is 4-connected (4/P/S) and has a score of 0.55, while the rightmost flow is 8-connected (8/P/S) with a score of 0.95. While the 4/P/S flow scores worse than a square, its 8-connected version passes the test as it scores better than an octagon.

#### 2.3.3.1 Benchmark Parameters

The DEM used in this benchmark is a horizontal plane (all grid locations have the same elevation) with a spatial resolution of 1 m. A single vent is located at the DEM center with a total volume of 1000 m<sup>3</sup>, and a pulse volume of 1 m<sup>3</sup>. When the simulation is finished, model output is used to find the inundated cell farthest from the vent ( $d_{max}$ ). The total inundated area is divided by the area of a circle with radius  $d_{max}$  to provide the Fit score.

### 2.3.3.2 Results

Five of the eight algorithms unambiguously passed the test of performing better than an octagon. In this test 8-connected algorithms outperformed 4-connected algorithms. Four algorithms unambiguously passed this test: 8/P/S, 8/N/S, 4/N/E, and 8/N/E.

Bingham Circle Results		
Algorithm	Circularity	
4/P/S	0.55	Worse than a square.
8/P/S	0.95	Better than an octagon.
4/N/S	0.55	Worse than a square.
8/N/S	0.98	Better than an octagon.
4/P/E	0.77	Between a square and an octagon.
8/P/E	0.80	Between a square and an octagon.
4/N/E	1.00	Perfectly circular.
8/N/E	0.99	Better than an octagon.

### 2.3.4 Level 3: Replication of real lava flows over complex topography

The recent availability of global or near-global topographic datasets, such as SRTM or ASTER GDEM has enabled the direct observation of the underlying surface of even more recent lava flows. Flow algorithms can be validated against recent lava flows by simulating lava over these surfaces with parameters defined by the new lava flows. The 2012-3 Tolbachik lava flows will be used as a benchmark for the eight flow algorithms. As discussed above (Section 2.1.1), the earliest lavas flowed from a fissure to the west. Before later stage flows began moving to the east, the volume of the lavas were  $0.22 \text{ km}^3$ . The modal thickness of the flow has been found to be 7.8 m and the areal extent was mapped with orthoimages (Kubanek et al., 2015).

For this example, two metrics which are commonly employed to validate lava flow simulators against real flows will be used: model sensitivity and a fitness metric called the

“Jaccard coefficient.” An alternative bayesian approach to these metrics is discussed in Section 2.4. Model sensitivity is defined as

$$\text{Model Sensitivity} = \frac{|Lava \cap Sim|}{|Lava|} \quad (2.7)$$

where  $|Lava \cap Sim|$  is the size of the intersection of the simulation and the true lava flow (the True Positives) and  $|Lava|$  is the size of the lava flow. This gives a percentage of the true lava flow that the simulation correctly predicted.

The Jaccard coefficient, or fit, is defined as

$$\text{Jaccard Fit} = \frac{|Lava \cap Sim|}{|Lava \cup Sim|} \quad (2.8)$$

where  $|Lava \cup Sim|$  is the size of the union of the lava flow and a simulated flow. This gives a percentage of the total area covered by either the simulated flow or the true flow that is covered by both.

Each flow algorithm is run using the following parameters. Flows are run over both 3-arcsecond SRTM topography (75 m grid resolution at 56°N) and bistatic TanDEM-X topography processed by Kubanek et al. (2015). The pulse volume, the volume added to vent cells at each code loop (i.e. each instance of the PULSE module), is set at the product of the grid-cell area (5600 m<sup>2</sup> for the SRTM DEM and 225 m<sup>2</sup> for the TanDEM-X DEM) and the residual thickness (7.8 m). Both fitness metrics are calculated with the resulting model output, given as a list of inundated locations. “Failure” can be defined here as either metric falling below 50% for the sake of example.

### Tolbachik Validation Flow Parameters

---

Elevation Model	75-m SRTM or 15-m TanDEM-X
Residual Thickness	7.8 m
Pulse Volumes	44200 m <sup>3</sup> (SRTM) or 1800 m <sup>3</sup> (TanDEM-X)
Vent <sub>N</sub> Easting	582800 m (UTM Zone 57)
Vent <sub>N</sub> Northing	6182100 m
Vent <sub>N</sub> Total Volume	4.63·10 <sup>7</sup> m <sup>3</sup>
Vent <sub>S</sub> Easting	582475 m
Vent <sub>S</sub> Northing	6180700 m
Vent <sub>S</sub> Total Volume	1.737·10 <sup>8</sup> m <sup>3</sup>

---

#### 2.3.4.1 Results

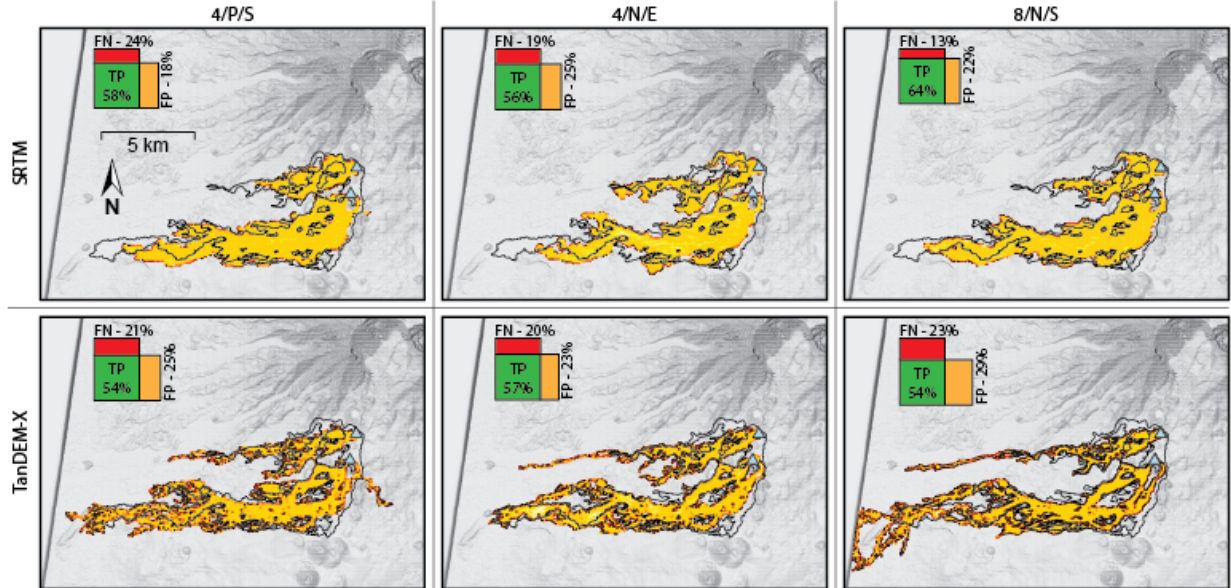


Figure 2.8: Three simulation algorithms (4/P/S, 4/N/E, and 8/N/S) applied to two elevation models (SRTM and TanDEM-X) to simulate the 2012-3 Tolbachik lava flows, outlined in black. Lava is emitted from two vent locations marked as blue triangles in the simulation. Diagrams showing the relative True Positives (green), False Positives (orange), and False Negatives (red) are illustrated in the top left of each simulation.

Three example algorithms are illustrated in Figure 2.8. One primary observation is that all simulations had a longer run-out length on the finer TanDEM-X grid than on the coarser SRTM grid. Despite this, all flows took the correct major pathways taken by the true lava flow. A small diagram in the top left corner of each map in Figure 2.8 shows the true positives, false positives, and false negatives in each simulation. True positives are areas inundated by both flow and simulation, false positives are areas simulated as being inundated but are not mapped as such, and false negatives are areas hit by lava that the simulation failed to forecast.

The best algorithm and DEM pair were the 8/N/S algorithm over SRTM (top left of Figure 2.8), while this same algorithm performed fairly poorly over TanDEM-X topography. For the SRTM simulation, this algorithm achieved a model sensitivity of 82.8% and a Jaccard fitness score of 63.1%. Graphically, sensitivity is calculated as the green area in the Figure 2.8 diagram divided by the green and red areas. The Jaccard fitness is the green area divided by the total area of the diagram. Because the Jaccard fitness statistic essentially expands the denominator of model sensitivity, it will never be higher than model sensitivity.

If success and failure are defined by having a fits of greater or less than 50%, all models tested would pass for the SRTM DEM and about half would pass for the TanDEM-X DEM. All but one model (4/P/E) performed worse on the TanDEM-X DEM. The Jaccard fit and Sensitivity for all models are given below.

### Tolbachik Flow Results

Transition		<b>SRTM DEM</b>		<b>TanDEM-X DEM</b>	
Function	Jaccard	Sensitivity	Jaccard	Sensitivity	
4/P/S	56.7%	76.4%	53.0%	72.4%	
8/P/S	61.1	80.8	46.8	67.2	
4/N/S	57.2	77.5	44.0	64.0	
8/N/S	63.1	82.8	46.7	67.4	
4/P/E	51.2	71.5	54.2	73.4	
8/P/E	58.8	78.2	56.3	76.0	
4/N/E	54.5	74.5	55.7	73.7	
8/N/E	59.6	78.8	56.2	75.3	

## 2.4 Bayesian Applications for Lava Flow Models

The final step Bayarri et al. (2007) give for validating computer models is “feeding [observations and results] back to revise the model.”

The use of computer models to forecast hazards is a fundamentally Bayesian strategy: there is an initial concern due to hazards and computer models help us inform, constrain, and update this concern. Using Bayesian statistics can therefore be an improvement in testing lava flow models, over the two commonly used fitness tests, model sensitivity and the Jaccard index, because of their more direct application to informing perceived risk.

Three tools will be used in this section: A posterior probability, a “negative” posterior probability, and a Bayes factor. Bayes theorem connects a phenomenon  $A$  to observations  $B$  through the function

$$\Pr(A|B) = \frac{\Pr(B|A)\Pr(A)}{\Pr(B)} \quad (2.9)$$

where  $\Pr(A)$  is the general probability of  $A$  occurring,  $\Pr(B)$  is the probability of  $B$  being observed, and  $\Pr(B|A)$  is the conditional probability of  $B$  given the occurrence of  $A$ .  $\Pr(B|A)$  is also known as model sensitivity, which is a common fitness statistic and was discussed in Section 2.3.4

The left side of Equation 2.9,  $\Pr(A|B)$ , is the Posterior probability of  $A$  and can be stated as “the probability that lava will inundate a location if the model forecasted inundation at that location.” A second posterior, which I call the negative posterior, is  $\Pr(\neg A|\neg B)$  and is the obverse of  $\Pr(A|B)$ . This negative posterior relates not being inundated by lava at a given location to a safe outcome forecasted by a simulation and can be calculated by modifying Equation 2.9 and substituting  $A$  for *Lava* (the lava flow) and  $B$  for *Sim* (the simulation), resulting in the formula

$$\Pr(\neg Lava|\neg Sim) = \frac{\Pr(\neg Sim|\neg Lava)\Pr(\neg Lava)}{\Pr(\neg Sim)} \quad (2.10)$$

where the  $\neg$  symbol indicates the event or observation not happening, and  $\Pr(\neg Sim|\neg Lava)$  is model specificity.

The negative posterior is important in hazard forecasting as it is in some sense a probability of safety. The more common posterior  $\Pr(A|B)$  (or  $\Pr(Lava|Sim)$ ) does not contain information about areas that the simulation does not inundate; while it can support the hypothesis that lava will hit a location given a simulated hit, it cannot estimate one’s relative risk if the simulation forecasts a safe outcome. The negative posterior  $\Pr(\neg Lava|\neg Sim)$  does just this, and informs a user whether to rely on a safe outcome from a simulation. If, for example, the posterior probability  $\Pr(Lava|Sim)$  is high while the negative posterior probability  $\Pr(\neg Lava|\neg Sim)$  is low for a given lava flow simulator, areas that are evacuated due to the simulation outcome will be evacuated for good reason, but many areas will likely be inundated that were not evacuated due to the simulation outcome. This is why it is important to estimate and ultimately try to improve both posterior metrics.

Bayes factors provide a tool to test the relative likelihood of a hypothesis against another. Aspinall et al. (2003) introduced this tool to volcano hazard forecasting by testing whether the onset of particular seismic events before the 1993 Galeras catastrophe was a significant indicator of the eruption or not. A Bayes Factor (BF) relating two models is

given by Jeffreys (1998) as

$$BF = \frac{\Pr(\text{Data}|\text{Model 1})}{\Pr(\text{Data}|\text{Model 2})} \quad (2.11)$$

In the example of Galeras, the “data” are the seismic events, Model 1 is “imminent explosion,” and Model 2 is “not imminent explosion” (Aspinall et al., 2003). Below, I will apply this with the data being the probability of simulated inundation and the models “lava inundation” and “not lava inundation.” Jeffreys (1998) provided a log-scale interpretation to the value of BF in Equation 2.11, given in the Table 2.2.

Table 2.2: Bayes Factor Interpretations (modified from Aspinall et al. (2003))

BF Value	Description
$BF > 10^2$	Evidence for Model 1 is Decisive.
$10^{1.5} < BF < 10^2$	Evidence for Model 1 is Very Strong.
$10^1 < BF < 10^{1.5}$	Evidence for Model 1 is Strong.
$10^{0.5} < BF < 10^1$	Evidence for Model 1 is Substantial.
$10^0 < BF < 10^{0.5}$	Evidence for Model 1 is just worth a mention.
$10^{-0.5} < BF < 10^0$	Evidence for Model 2 is just worth a mention.
$10^{-1} < BF < 10^{-0.5}$	Evidence for Model 2 is Substantial.
$10^{-1.5} < BF < 10^{-1}$	Evidence for Model 2 is Strong.
$10^{-2} < BF < 10^{-1.5}$	Evidence for Model 2 is Very Strong.
$BF < 10^{-2}$	Evidence for Model 2 is Decisive.

In the same manner as the final validation level, the statistics discussed above will be calculated based on the areal extent of flows and simulations. The probability of the lava flow inundating an area  $N$  can be given as

$$\Pr(A) = \frac{|Lava|}{|N|} \quad (2.12)$$

where  $|Lava|$  is the areal size of the flow (i.e. literally the number of DEM grid cells the lava inundates) and  $|N|$  is the size of the area of interest, or the potential hazard area. The

probability of the simulation is similarly found to be

$$\Pr(Sim) = \frac{|Sim|}{|N|}. \quad (2.13)$$

By substituting these definitions and model sensitivity (Equation 2.7,  $|Lava \cap Sim|/|Lava|$ ) in Equation 2.9, the posterior probability of lava flow inundation, given a simulation that forecasts inundation can be recast as

$$\Pr(Lava|Sim) = \frac{\frac{|Lava \cap Sim|}{|Lava|} \frac{|Lava|}{|N|}}{\frac{|Sim|}{|N|}}, \text{ or simplified,} \quad (2.14)$$

$$= \frac{|Lava \cap Sim|}{|Sim|}. \quad (2.15)$$

where  $|Lava \cap Sim|$  is the size of the intersection of the lava flow and simulated flow (again, the number of DEM grid cells). Note that this posterior probability is independent of the potential hazard area.

The negative posterior can be stated in terms of the sizes of the lava flow and simulated flow as well.

$$\Pr(\neg Lava | \neg Sim) = \frac{|\neg Lava \cap \neg Sim|}{|\neg Sim|} \quad (2.16)$$

Calculating the size or number of grid cells of  $\neg Lava$  or  $\neg Sim$  is fundamentally dependent on the potential hazard area, as  $|\neg Lava|$  is defined as

$$|\neg Lava| = |N| - |Lava|. \quad (2.17)$$

Because of this, we must define the size of the potential hazard area  $N$  ( $|N|$ ).

**2.4.0.1.1 Potential Hazard Area** There are multiple strategies to estimating an *a priori* hazard area. Kauahikaua et al. (1995) for instance identified catchments or “lava sheds” in which a volcanic vent was erupting, and identified these lava sheds as the hazard

area. Kilburn (2000) provided a theoretical maximum distance that a lava flow can travel given the mass flux of magma erupting at the vent location. A combination of these two would provide an objective hazard area defined as the area within the “Kilburn distance” that is topographically below the volcanic vent. The theoretical maximum distance, or hazard radius, given by Kilburn (2000) is

$$R_{max} = \sqrt{\frac{3\epsilon S Q}{\rho g \kappa}} \quad (2.18)$$

where  $\epsilon$  is an empirical value related to the amount of extension of lava crust allowed before it fails ( $10^{-3}$ ),  $S$  is the tensile strength of this crust ( $10^7$  Pa),  $\rho$  is the lava crust density ( $2200$  kg m $^{-3}$ ),  $g$  is gravitational acceleration,  $\kappa$  is the bulk thermal diffusivity ( $4 \times 10^{-7}$  m $^2$  s $^{-1}$ ) and  $Q$  is the mean volumetric flow rate from the vent. From this, the hazard radius for the Tolbachik 2012-3 flow is calculated to be 39 km, given a magma flux of 440 m $^3$  s from the vent as was estimated early in the eruption (Belousov et al., 2015). The total area within this radius that is also below the vent-plus-modal-flow-thickness elevation is 1,415 km $^2$ . Note that the mapped flow area of 26 km $^2$  only covers 1.9% of this defined hazard area (i.e.  $Pr(Lava) = 0.019$ ).

A second strategy would be to run many lava flow models from the known vent location(s) while varying input parameters. This would give a range of flows and the true flow might be completely contained within the region given by this range of simulations. Below, a Monte Carlo (MC) method will be used to simulate a large range of flows. If we define a potential hazard area as any location inundated by at least one simulated flow in this MC approach, the hazard area would be 72 km $^2$ . As the mapped flow area from the Tolbachik eruption is 39% of this area, it would be more practical to use this as the *a priori* hazard area because it more reasonably reflects the potential inundation area. Both the Kilburn-Kauahikaua method and this MC method are illustrated in Figure 2.9.

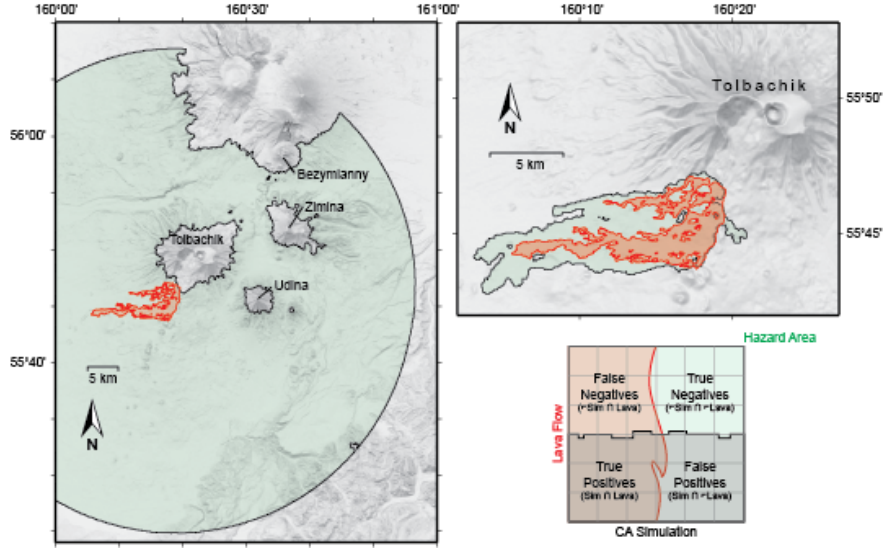


Figure 2.9: Potential hazard areas of the 2012-3 Tolbachik Flows in light green, defined by a maximum flow radius (left, Equation 2.18) and the total areal coverage of 100,000 random flow simulations (top-right, Section 2.4.2). The mapped lava flow is red. The chart to the bottom right shows four regions defined by the presence or absence of lava and simulated lava across a map grid.

**2.4.0.1.2 Review of Validation Level 3** Instead of using model sensitivity and the Jaccard index as benchmarks for the various lava flow models, now the two posteriors will be used. The potential hazard area is defined as the distribution of MC simulations ( $72 \text{ km}^2$ ). To give an example calculation,  $\Pr(Lava|Sim)$  is found with Equation 2.15 by dividing true positives (green boxes in 2.8) by the simulation area (green and red boxes). The negative posterior,  $\Pr(\neg Lava|\neg Sim)$ , is found by diving true negatives (blue area, in bottom right diagram of Figure 2.9), by the area not simulated (top half of bottom right diagram of Figure 2.9).

### Traditional Fit Metrics and Bayesian Posterior Functions

---

Transition		Results of simulations over SRTM DEM		
Function	Jaccard	Sensitivity	$\Pr(Lava Sim)$	$\Pr(\neg Lava \neg Sim)$
4/P/S	56.7%	76.4%	70.4%	84.5%
8/P/S	61.1	80.8	73.2	87.3
4/N/S	57.2	77.5	70.3	85.1
8/N/S	63.1	82.8	74.4	88.5
4/P/E	51.2	71.5	66.0	81.4
8/P/E	58.8	78.2	72.0	85.7
4/N/E	54.5	74.5	68.7	83.3
8/N/E	59.6	78.8	72.8	86.2

---

For the rest of this section, the 8/N/S (the 8-connected, no parent-child relationships, with slope-proportional spreading) algorithm will be used. This is preferred because it outperformed other algorithms over the SRTM DEM. By applying this model to the Tolbachik lava flows, Bayesian methods will be used to improve the “Pulse Volume” parameter and will later be used to constrain model uncertainty at Tolbachik.

#### 2.4.1 Improving model performance on one model parameter

In the Tolbachik benchmark tests given as examples of comparing simulation algorithms against real lava flows (Section 2.3.4), all but one algorithm performed worse on the TanDEM-X derived elevation model. This was in part due to large run-out distances in the simulations (e.g. bottom right of Figure 2.8), which considerably increased simulation false positives. The large run-out distances might be due to the pulse volume, the volume of lava given to source cells at each code loop in MOLASSES, being poorly chosen. Here, the Bayesian statistics defined above will be used to compare different pulse volumes and identify an optimal pulse volume.

An optimal pulse volume will ideally produce a flow simulation with the highest posterior and negative posterior value. Pulse volumes with high associated posterior values will

produce simulations where areas simulated as inundated by lava will have a high likelihood of actually being inundated by lava. Pulse volumes with high associated negative posterior values will produce simulations where areas simulated to not be inundated will have a high likelihood of actually not being inundated.

#### 2.4.1.1 Model Execution

To populate  $\text{Sim}$ , I have run the MOLASSES lava flow code using TanDEM-X derived parameters listed in Table 2.3. All variables are fixed except the pulse volume parameter, which is the amount of lava delivered to source cells in the Cellular Automata grid of MOLASSES. The lowest pulse volume,  $1755 \text{ m}^3$  per pulse, is approximately the product of the TanDEM-X DEM grid cell size ( $225 \text{ m}^2$ ) and the residual flow thickness ( $7.8 \text{ m}$ ). The other 15 pulse volumes are multiples of this volume (i.e. they are  $1.5$  to  $8.5 \times 1775 \text{ m}^3$ ).

Table 2.3: MOLASSES Flow Parameters

Elevation Model	15-m bistatic TanDEM-X, 11 Nov 2015
Modal Thickness	$7.8 \text{ m}$
Pulse Volumes	16 equally separated volumes, $[1755,14917] \text{ m}^3$
$\text{Vent}_N$ Easting	$582800 \text{ m}$ (UTM Zone 57)
$\text{Vent}_N$ Northing	$6182100 \text{ m}$
$\text{Vent}_N$ Total Volume	$4.63 \cdot 10^7 \text{ m}^3$
$\text{Vent}_S$ Easting	$582475 \text{ m}$
$\text{Vent}_S$ Northing	$6180700 \text{ m}$
$\text{Vent}_S$ Total Volume	$1.737 \cdot 10^8 \text{ m}^3$

Model output is compared to a list of x,y locations in the Tolbachik area that have been inundated or not. This location list is stored in a raster with the same projection and extent as the elevation model used in MOLASSES. ASCII locations output by MOLASSES are also listed in the same projection within the same extent as the elevation model. This enables direct comparison between the Model information (i.e.  $\text{Sim}$ ) and the mapped lava flow (i.e.  $\text{Lava}$ ). True Positives, False Positives, and False Negatives are reported as cell

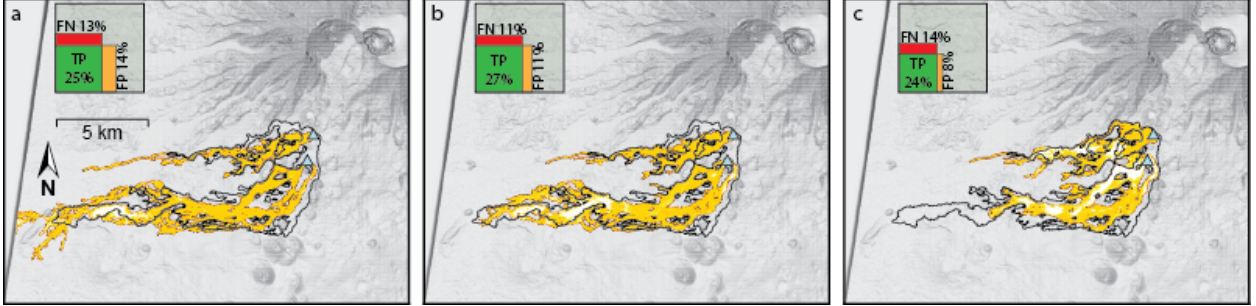


Figure 2.10: MOLASSES Simulations of the 2012-3 Tolbachik Lava Flows. Vents are shown as blue triangles and the mapped flow is outlined in black. a) Pulse Volume = 1755 m<sup>3</sup>, the simulation far exceeds the true runout distance; b) Pulse Volume = 4387 m<sup>3</sup>, this simulation performs best under the negative posterior  $\text{Pr}(\neg \text{Lava} | \neg \text{Sim})$  test; c) Pulse Volume = 14040 m<sup>3</sup>, this simulation performs best under the posterior  $\text{Pr}(\text{Lava} | \text{Sim})$  test, but does not have a runout length similar to the mapped flow.

counts (number of grid locations where *Lava* and *Sim* agree or not). Three examples of these simulations are mapped in Figure 2.10.

#### 2.4.1.2 Results

Three example simulations are shown in Figure 2.10 using simulation parameters from Table 2.3 and different pulse volume values. With increased pulse volume, simulated run-out distance is shorter. This is because the MOLASSES code ends once all volume is delivered to the vents and the DISTRIBUTE module has run once more. In other words, if the pulse volume is doubled, the number of times the PULSE and DISTRIBUTE modules will be run will be halved, as the total volume will be delivered to the vents in half the code loops (see Figure 2.2). By running DISTRIBUTE fewer times, cells have fewer opportunities to advect lava downslope.

The posterior statistical measure is the fundamental tool of Bayesian statistics, and quantifying it enables an update of belief in risk of lava inundation. A perfect posterior value would mean that if the model simulates lava inundating a location, lava will certainly inundate that location. The posterior is calculated for simulated lava flows of different Pulse Volumes and is graphed in Figure 2.11. From this, it can be seen that the highest pulse

volumes, which coincidentally form the shortest flow simulations, perform best with this test, with the best fit having a pulse volume of 14040 m<sup>3</sup> per algorithm loop (Figure 2.10,c). A local maximum does exist in the low pulse volumes at 4387 m<sup>3</sup> per loop.

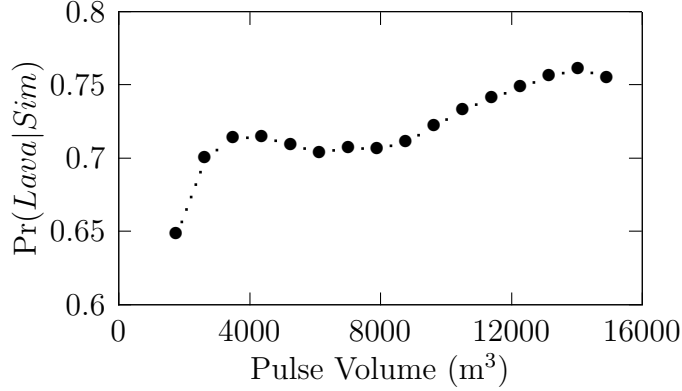


Figure 2.11: Posterior  $\text{Pr}(Lava|Sim)$  for MOLASSES flows with differing Pulse Volumes.

The negative posterior  $\text{Pr}(\neg Lava|\neg Sim)$ , is the percentage of non-inundated area in the simulation that is also not inundated in real life. A perfect negative posterior would indicate that, if a model does not simulate a hit for a location, lava will certainly not inundate that location. The negative posteriors of simulations with different pulse values are shown in Figure 2.12. Unlike the previous posterior analyzed, the best performing flows have smaller pulse volumes and the best performing volume is 4387 m<sup>3</sup> per model pulse loop (Figure 2.10,b).

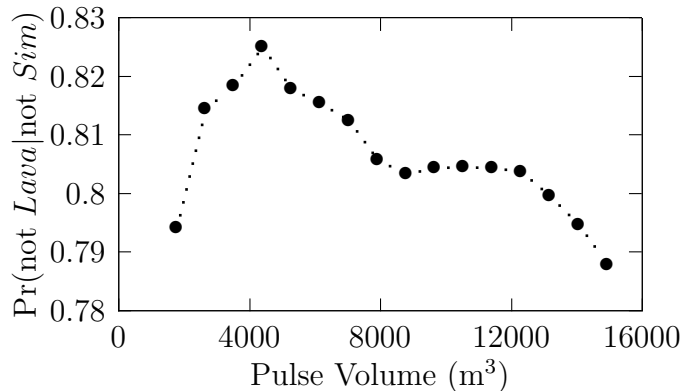


Figure 2.12: Negative posterior  $\text{Pr}(\neg Lava|\neg Sim)$  for MOLASSES flows with differing Pulse Volumes.

### 2.4.2 Incorporating Model Uncertainty with a Monte Carlo method

Model uncertainty is a result of input parameter uncertainty, such as uncertainty in the underlying DEM. This can be distinguished from model error, which might be defined as the difference between the true lava flow and a simulation carried out with perfect input parameters, and is created by the inherent deviations between a computer model and real life processes. Because there is parameter uncertainty, it is essential to quantify the range of model solutions given the likely range of each parameter.

In this example, elevation uncertainty will be examined. Elevation uncertainty is an element in the MOLASSES module **INITFLOW**, where each grid cell elevation can be defined randomly before the lava flow simulation begins. The user can add an elevation uncertainty, in meters, to the configuration file. If this value is provided, each grid cell will receive a new elevation value randomly selected from a normal distribution whose mean is the DEM elevation and the standard deviation is the uncertainty value.

Table 2.4: Monte Carlo MOLASSES Flow Parameters

Elevation Model	75-m SRTM
Elevation Uncertainty, $1\sigma$	3 m
Residual Thickness	7.8 m
Pulse Volume	$44200 \text{ m}^3$
$\text{Vent}_N$ Easting	582800 m (UTM Zone 57)
$\text{Vent}_N$ Northing	6182100 m
$\text{Vent}_N$ Total Volume	$4.63 \cdot 10^7 \text{ m}^3$
$\text{Vent}_S$ Easting	582475 m
$\text{Vent}_S$ Northing	6180700 m
$\text{Vent}_S$ Total Volume	$1.737 \cdot 10^8 \text{ m}^3$

The Monte Carlo method runs MOLASSES 100,000 times over a 75-m SRTM DEM. Vertical uncertainty of this data is estimated by Rodríguez et al. (2006) for Eurasia to be 6.2 m at a 90% confidence level and is shown to be randomly distributed. With this result, elevation uncertainty in the MOLASSES model is given a value of  $1\sigma = 3$  m. Other input parameters remain unchanged from the benchmark exercise above; MOLASSES flow param-

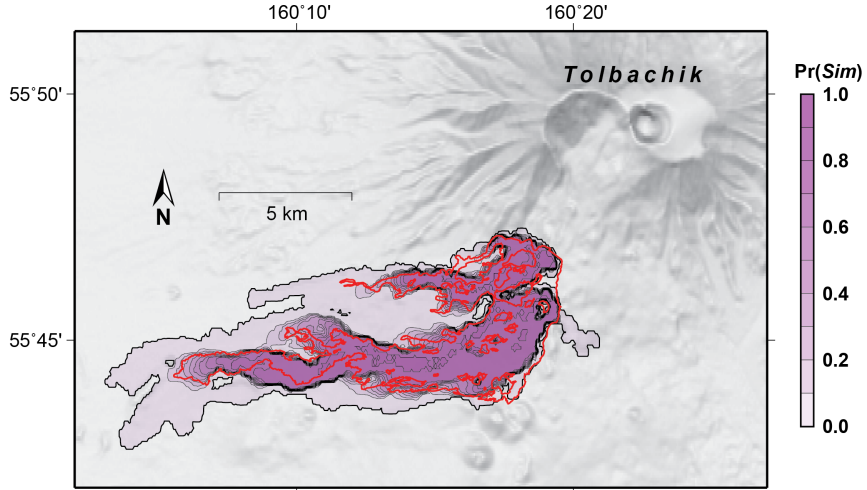


Figure 2.13: Cumulative distribution of 100,000 simulated lava flows over SRTM topography with 3 m elevation uncertainty. The red outline is the mapped flow extent of the 2012-3 Tolbachik flow. Darker purple areas represent more simulation hits (i.e. higher  $\text{Pr}(Sim)$ ).

eters for the Monte Carlo model are listed in Table 2.4. The combined 100,000 simulations are mapped in Figure 2.13 where flow color indicates the number of flows that impacted each location.

#### 2.4.2.1 Bayesian distribution of MC results

The reliability of a model can be better understood by showing the distribution of model performance given model uncertainty, as opposed to treating model parameters, and thus model output, as completely certain. Figure 2.14 shows the distribution of the posterior and the negative posterior scores. Each dot in the main chart of Figure 2.14 represents a single flow simulation over a partially randomly generated DEM. The clustering of these points shows a positive correlation between the two posterior metrics, and both metrics are not normally distributed as shown on the histograms on either side of the main chart of Figure 2.14. The flow simulation assuming no elevation uncertainty (shown in the top right corner of Figure 2.8) fits the mapped flow better than the median value of both posteriors in the distribution, though it still lays within the MC distribution.

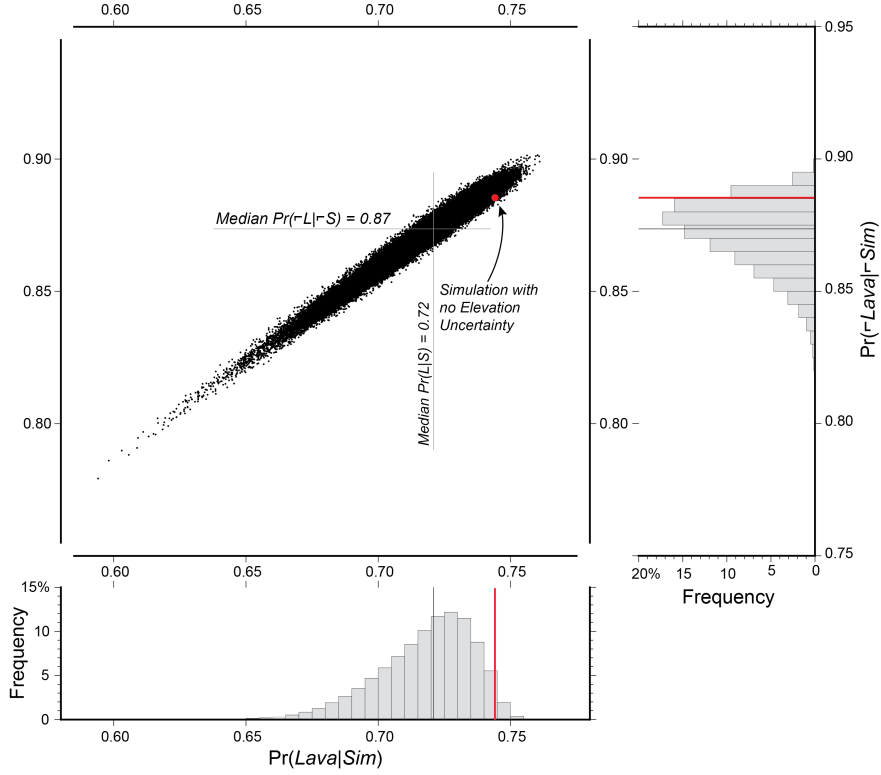


Figure 2.14: Fitness statistic distribution between for 100,000 simulations of the 2012-3 Tolbachik Lava Flows, over SRTM topography with 3 m standard elevation uncertainty. Each point represents the posterior probabilities of inundation/non-inundation for one simulation. Red lines are the fitness values of a simulated flow over SRTM data assuming 0 m elevation uncertainty (top right corner of Figure 2.8). Black lines are placed at the median values of each posterior probability.

If the elevation model used were perfect, the posterior values would be a single number ( $\text{Pr}(\text{Lava}| \text{Sim}) = 74.4\%$  and  $\text{Pr}(\neg \text{Lava}| \neg \text{Sim}) = 88.5\%$ ). However, because elevation values have inherent uncertainty, model fitness, as defined by the posterior values, can be given as a range. Including elevation uncertainty, the  $\text{Pr}(\text{Lava}| \text{Sim})$  fitness has a range of 59-76% and the  $\text{Pr}(\neg \text{Lava}| \neg \text{Sim})$  has a range of 77-91%.

#### 2.4.2.2 Estimating inundation risk from the simulated frequency of inundation

Figure 2.13 shows a map view of the probability of inundation from the 100,000 MC simulations. Generally, areas within the mapped flow appear to be inundated by more simulations than outside the mapped flow. But can the probability of simulation inundation,  $\text{Pr}(\text{Sim})$ ,

be used in a more formal way to judge the probability of lava inundation? In this section, the Tolbachik region map will be split into sub-regions based on  $\Pr(Sim)$ , and the probabilities of inundation and not inundation will be compared.

Three example sub-regions are shown in Figure 2.15. These sub-regions are defined as the area where  $\Pr(Sim)$  falls between a 10% range. For instance, the top sub-region in Figure 2.15 shows all locations that were forecast as inundated by at least 90% of all MC simulations, while the middle sub-region example contains all locations inundated by 40-50% of simulations. The sub-regions inundated by 0-10% and 90-100% of simulations are the largest sub-regions, while other sub-regions are thin rings between these two bounding sub-regions.

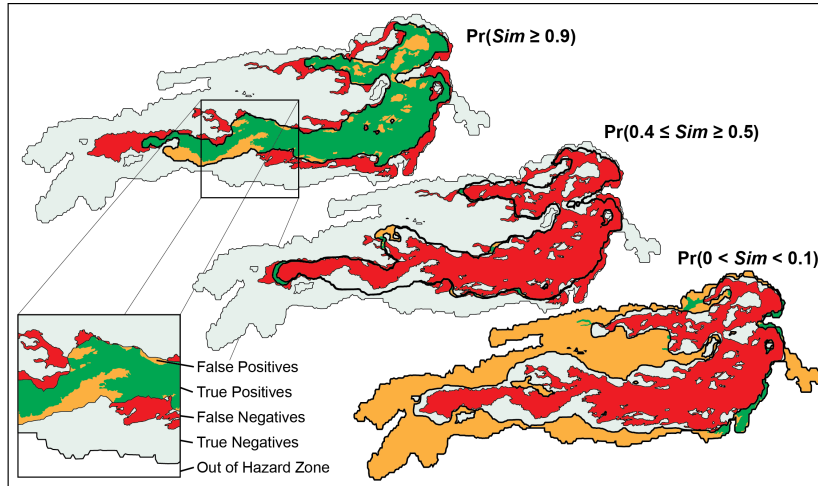


Figure 2.15: Sub-regions within the Monte Carlo solution, defined by  $\Pr(Sim)$ . At the top, all areas inundated by  $\geq 90\%$  of all simulations are shown in green (True Positives) and orange (False Positives). The remaining mapped lava flow (False Negatives) is red. The underlying region is the total Monte Carlo Hazard Area. At center, A thin band represents all areas inundated by 40-50% of all Simulations. At bottom, a thick shell of areas rarely inundated by simulated lava is mostly orange, indicating rarely simulated flow areas are unlikely to have been inundated in real life.

It can be seen in Figure 2.15 that most of the mapped flow is covered by the  $\Pr(Sim \geq 90\%)$  sub-region, as the green true positive region is larger than the red false negative region. The sub-region defined as  $\Pr(0 < Sim < 10\%)$  does not spatially intersect with the mapped flow area as much as the  $\Pr(Sim \geq 90\%)$  sub-region, and this can be seen in the lower right

of Figure 2.15 as the sub-region area is mostly orange false positives with small green true positive areas.

The relative risk of inundation can be calculated for each subregion by comparing the probability of actual flow inundation  $\Pr(Lava)$  against the probability of not inundation  $\Pr(\neg Lava)$  using the Bayes Factor of Equation 2.11. Here “Data” is the probability of simulated inundation  $\Pr(Sim = X)$ , Model 1 is Real Flow Inundation and the opposing Model 2 is No Real Flow Inundation. For example, the relative probability of inundation for the sub-region defined by  $\Pr(40 \leq Sim < 50\%)$  can be given as

$$BF = \frac{\Pr(0.4 \leq Sim < 0.5 \mid \text{Inundation})}{\Pr(0.4 \leq Sim < 0.5 \mid \text{Not Inundation})}. \quad (2.19)$$

The numerator  $\Pr(0.4 \leq Sim < 0.5 \mid \text{Inundation})$  is the probability of 40-50% of simulations hitting a given location, given the location actually being hit by lava. Graphically, this is the percent of the true flow (red and green areas in the center example of Figure 2.15) that are within the simulated sub-region (green areas in the center example of Figure 2.15). The denominator  $\Pr(0.4 \leq Sim < 0.5 \mid \text{Not Inundation})$  is probability of 40-50% of simulations hitting a location, given the location is not inundated in the real flow. This is the percent of the area not hit by the flow (light gray and orange areas in Figure 2.15) that is within the subregion (orange areas in Figure 2.15).

The probability that 40-50% of simulations hit a location that is inundated is 2.7%. The probability the 40-50% of simulations hit a location that is not inundated by lava is 2.1%. The Bayes Factor is then calculated to be 1.3, where the model of Inundation is 1.3 times more likely to describe this subregion than the model of Not Inundation. Referring to Table 2.2, this result means that the preference for Inundation over Not Inundation is “just worth a mention.” Results for each 10% wide sub-region are given in Table 2.5 and are illustrated in Figure 2.16.

Table 2.5: Relative likelihood of inundation given  $\Pr(\text{Sim})$

X	$\Pr(\text{Sim}=\text{X}   \text{Lava})$	$\Pr(\text{Sim}=\text{X}   \neg \text{Lava})$	Bayes Factor	Jeffreys (1998) Interpretation
$0 < \text{X} < 0.1$	0.06	0.67	0.09	Strong evidence against inundation
$0.1 \leq \text{X} < 0.2$	0.02	0.08	0.23	Substantial evidence against inund.
$0.2 \leq \text{X} < 0.3$	0.03	0.04	0.74	No Inundation more likely
$0.3 \leq \text{X} < 0.4$	0.03	0.03	1.21	Inundation more likely than not
$0.4 \leq \text{X} < 0.5$	0.03	0.02	1.29	Inundation more likely than not
$0.5 \leq \text{X} < 0.6$	0.03	0.02	1.53	Inundation more likely than not
$0.6 \leq \text{X} < 0.7$	0.04	0.01	2.63	Inundation more likely than not
$0.7 \leq \text{X} < 0.8$	0.05	0.02	2.69	Inundation more likely than not
$0.8 \leq \text{X} < 0.9$	0.06	0.02	2.84	Inundation more likely than not
$0.9 \leq \text{X} \leq 1.0$	0.66	0.10	6.93	Substantial evidence for inundation

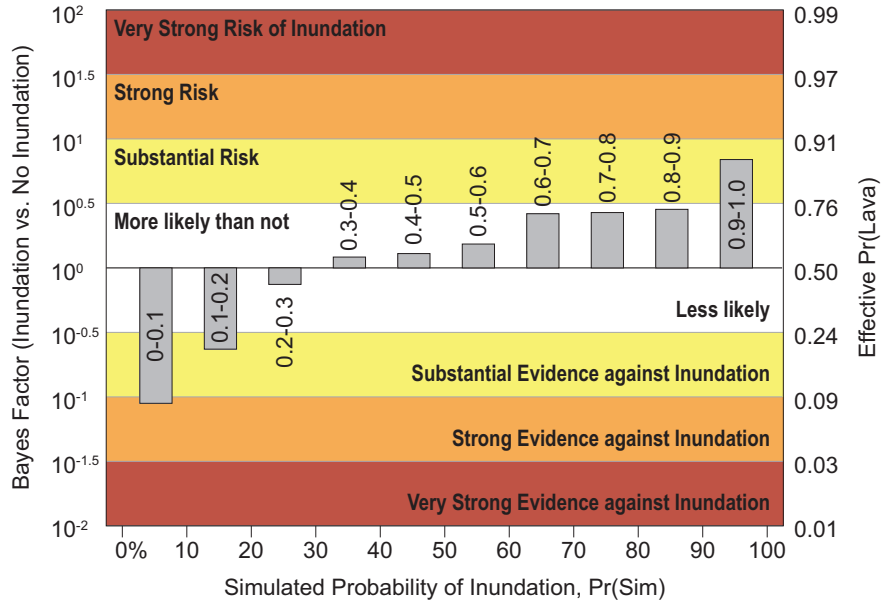


Figure 2.16: Relative likelihood of inundation given  $\Pr(\text{Sim})$ . Only locations inundated by  $< 10\%$  of Monte Carlo simulations show strong evidence against inundation in the actual 2012-3 Tolbachik lava flows.

Only the sub-region least likely to be hit by simulations, where  $\Pr(\text{Sim} < 10\%)$ , has a Bayes Factor of  $< 10^{-1}$ , which is interpreted as strong evidence against lava flow inundation. As the Bayes Factor can be treated as posterior odds for or against a model (Aspinall et al., 2003), a factor of 1/10 indicates 10:1 odds against inundation. Sub-regions with factors greater than 1/10, and are therefore more in support of flow inundation, have odds less than

10:1 against inundation. As 10:1 odds against inundation is the same as a probability of 9% for inundation, all sub-regions besides the  $\Pr(\text{Sim} < 10\%)$  sub-region have  $\Pr(\text{Lava} > 9\%)$ .

## 2.5 Discussion

### 2.5.1 Benchmark Validation

Unique flow algorithms are validated by using common benchmarks that show whether these algorithms replicate expected lava flow morphologies under specific conditions. Different benchmark tests that are applicable to CA codes fall into three validation levels: 1) tests that show that simulations don't change when parameters remain meaningfully identical; 2) tests that show that simulations replicate experimental results or analytical expectations; and 3) tests that show that simulations replicate real world flow examples. A summary of the results of the eight algorithms against the example benchmarks are given below in Table 2.6.

Table 2.6: Transition Algorithm Results

Transition Function	Levels			
	1 DEM Rotation	2 Pancake	3 SRTM	3 TanDEM-X
4/P/S	Pass	Fail	Pass	Pass
8/P/S	Pass	Pass	Pass	Fail
4/N/S	Fail	Fail	Pass	Fail
8/N/S	Pass	Pass	Pass	Fail
4/P/E	Fail	Ambiguous	Pass	Pass
8/P/E	Fail	Ambiguous	Pass	Pass
4/N/E	Fail	Pass	Pass	Pass
8/N/E	Fail	Pass	Pass	Pass

Because these validation levels increase in complexity from Level 1 to Level 3, one possible strategy in validating different algorithms would be to only test algorithms at more complex benchmarks after they successfully pass less complex benchmarks. Valid models might then be determined by elimination. Only 3 of 8 tested algorithms pass the first “rotating slope” benchmark: 4/P/S, 8/P/S, and 8/N/S. Although more algorithms passed the second “bingham flow on a flat surface” benchmark, only 8/P/S and 8/N/S passed

the previous benchmark and this one. Both of these flows then successfully replicated the Tolbachik lava flows over SRTM topography. Therefore the 8/P/S and 8/N/S algorithms hold up to three benchmark tests.

Overall, in all tests 8-connected models outperform 4-connected models. While equal sharing algorithms outperform slope-proportional sharing on a flat slope, they fail on a rotating DEM and perform about the same on real topography. There does not seem to be an unambiguously better choice between using parent-child relationships or not. If future tests continue to show similar performance between models with and without parentage, other reasons can be used to choose a model, such as computer run-time.

The strength of the MOLASSES code is that new algorithms, such as those used in the SCIARA model (Crisci et al., 2004), can be implemented relatively quickly and run through the Benchmarking tests, which are written in Python. Combinations of implementation strategies can also be created on the fly by adjusting the makefile of the MOLASSES code instead of the code itself.

### **2.5.2 Bayesian applications for real lava flows**

Validation of lava flow models is important as a method of increasing the value of models to forecast lava flow processes, thereby decreasing preventable loss. Flow models are generally improved by reducing false positives and false negatives while increasing the true positive area, which is the union of a flow simulation and real, mapped lava flows. Often, reducing one type of error comes at the cost of increasing another type. For example, by increasing the pulse volume parameter, false positives can be reduced while false negatives are increased (Figure 2.10).

A decision can be made as to whether false positives or false negatives are more important to reduce in calibrating a lava flow model. One possible decision would be to prefer the reduction of false negatives over the reduction of false positives, with the reason being that a forecast of inundation without eventual engulfment by lava (a false positive result) is bad, but an unexpected engulfment by lava (a false negative) would be worse.

### 2.5.2.1 Using Bayesian statistics to compare models

In Section 2.4.1, an optimal pulse volume was defined as a volume that produced a simulated lava flow that had the highest posterior and negative posterior values. However, the pulse volume  $14040 \text{ m}^3$  had the highest posterior value, while the pulse volume  $4387 \text{ m}^3$  had the highest negative posterior value. The simple definition of “optimal” pulse volume does not seem to work.

The best pulse volume might be decided based on a preference for reducing false negatives as discussed above. The posterior probability of inundation,  $\Pr(Lava|Sim)$  increases with increased true positives and decreases with increased false positives (Equation 2.15). It is essentially blind to false negatives. The negative posterior  $\Pr(\neg Lava|\neg Sim)$  probability is the opposite, increasing with increased true negative results, while decreasing with increased false negative results (Equation 2.16).

If false negatives are more important to reduce than false positives, more weight can be given to the negative posterior value of a simulation than the positive posterior value. In Figure 2.17, the posterior and negative posterior values for each pulse volume (Figures 2.11 and 2.12) are used to produce weighted average scores of pulse volume. The extent to which false negative reduction might be preferred over false positive reduction is unknown, so four hypothetical weights are used. One of the weighted averages that is plotted assumes both posteriors are equally important in determining the best pulse volume parameter. The other three curves weight the negative posterior as being 2, 5, and 10 times as important as the positive posterior in scoring pulse volumes. Using these three weights, the highest scoring pulse volume is  $4387 \text{ m}^3$  (Figure 2.10b). If the two posteriors have equal importance, the highest scoring pulse volume is  $14040 \text{ m}^3$  (Figure 2.10c).

### 2.5.2.2 Decision Making with the Bayes Factor

By dividing the Monte Carlo set of simulations of the Tolbachik lava flows into sub-regions based on  $\Pr(Sim)$ , the relative likelihood of inundation was calculated (Figure 2.16). By

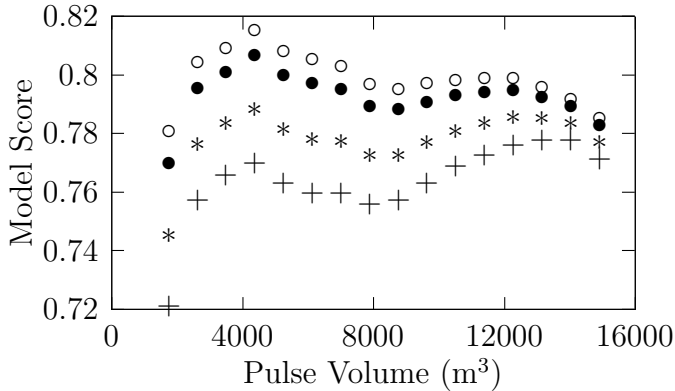


Figure 2.17: Weighted averages of  $\Pr(Lava|Sim)$  and  $\Pr(\neg Lava|\neg Sim)$  for different pulse volumes. Hollow circles, negative posterior ( $\Pr(Lava|Sim)$ ) is given  $10\times$  the weight of the posterior ( $\Pr(\neg Lava|\neg Sim)$ ); solid circles,  $5\times$  weight; asterisks,  $2\times$  weight; plusses, equal weight between posteriors. The highest scoring pulse volume is  $4387\text{ m}^3$  for all weight ratios except when both posterior values are weighted equally.

using the Bayes Factor to compare likelihood of Indundation to Not Inundation, most sub-regions were not significantly better described by one model or the other. Only the sub-region of locations least likely to be hit by flow simulations had “strong evidence” against inundation, and only the sub-region of locations most likely to be hit by simulations had “substantial risk” of inundation. These results leave a large amount of ambiguity when making decisions to fortify or evacuate due to a lava flow.

In discussing the decision making process for calling an evacuation due to an eruption at Mount Vesuvius, Marzocchi and Woo (2007) provided a cost-loss model where two actions can be taken, protect and do not protect. Two costs are associated with these actions:  $\mathcal{C}$  is the cost of protection and  $\mathcal{L}$  is the cost of loss if the volcanic hazard occurs while a decision to not protect is made. If  $\mathcal{L}$  is incurred, it is assumed to exceed cost  $\mathcal{C}$ , often because loss due to volcanic hazards includes the loss of life.

Marzocchi and Woo (2007) show that the minimum cost can be achieved if protection occurs when  $p > \mathcal{C}/\mathcal{L}$  where  $p$  is the probability of the hazard occurring. The ratio  $\mathcal{C}/\mathcal{L}$  is hard to quantify because the socio-economic cost of lost lives or of lost trust in the government (in the case of false evacuations) is difficult to calculate, even though the physical cost of evacuation and the cost of infrastructure loss might be straight forward estimates. Woo

(2008) provided one estimate of  $\mathcal{C}/\mathcal{L} = 0.1$  at the very maximum if 10% of people evacuated from an area would owe their lives to that evacuation. In this case, protection would be made when  $p > 0.1$ .

While lives are not commonly lost due to lava flows with the notable exceptions of Laki (A.D. 1783, Iceland) and Nyiragongo (A.D. 1977 and 2002, Democratic Republic of the Congo) (Peterson and Tilling, 2000), the “protection threshold”  $p > 0.1$  can still be used as an example. All Monte Carlo sub-regions have a probability of inundation ( $\text{Pr}(Lava)$ ) greater than 0.1 except the sub-region  $\text{Pr}(Sim < 0.1)$  (Figure 2.16). If action to protect is made at  $\text{Pr}(Lava > 0.1)$ , then evacuations or fortifications will be made for all locations inundated by  $\geq 10\%$  of Monte Carlo simulations.

Two Bayes-factor thresholds in Figure 2.16 have odds against lava inundation at better than 10:1 (i.e.  $\text{Pr}(Lava < 0.1)$ ), “strong evidence” and “very strong evidence” against inundation. Given the hypothetical protection threshold of  $p > 0.1$ , the decision to protect against a lava flow should be made for a location whenever the Bayes factor supporting inundation is  $> 10^{-1}$ , or when there is less than “strong evidence” against inundation for that area. If the protection threshold is decided to be less than 0.1, then the evidence against inundation will have to be even stronger to support a decision to not protect an area.

It is unknown whether sub-regions defined as  $\text{Pr}(Sim < 0.1)$  should be expected to be relatively safe areas when using Monte Carlo results at future lava flow sites. To test the effectiveness of the MOLASSES algorithm used for the Tolbachik flows in other study areas, more example flows around the world will have to be tested.

## 2.6 Conclusions

The MOLASSES framework used in this project provides a modular set of functions that can be interchanged to fundamentally alter the flow simulation algorithm. While only 8 different algorithms, which focused on simple variations in the transition function of Cellular Automata codes, were explored, different modules can feasibly be modified to change

other flow characteristics (e.g. vent geometry, mass flux at source locations, temperature dependent flow).

All CA and CA-like codes, including SCIARA (Crisci et al., 2004), MAGFLOW (Del Negro et al., 2008), ELFm (Damiani et al., 2006), LavaPL (Connor et al., 2012), and MOLASSES share similarities. For instance, lava inundation is a binary condition for each location on a grid and source locations are set at defined grid cell coordinates. This enables a common set of benchmarks to be defined, which can be used to test the validity of all CA codes.

Three validation levels have been identified and different benchmark tests have been given which apply to each level. After a code is successfully demonstrated to conserve mass, the first validation level ensures that the code does not change when parameters are changed in a meaningless way. The example benchmark is that simulated flows should not be slope-direction dependent. The second level compares simulations to analytical or experimental results. As lava flows on large scales are similar to Bingham fluids, a flow simulator should produce a circular pattern on a flat surface. The third and final level tests simulations against true lava flows. Here, the 2012-3 Tolbachik lava flow is used as an example, with flow parameters identified using TanDEM-X analysis (Kubanek et al., 2015). It might only make sense to validate codes at higher validation levels once they have been sufficiently developed to be validated at lower levels.

Two common fitness tests for lava flows are the Jaccard coefficient and model sensitivity. Model sensitivity gives the percentage of a mapped lava flow that a simulation successfully forecasts. A possible alternative to these tests is to use Bayesian posterior probabilities to evaluate the positive and negative predictive values of the simulation. These posteriors ( $\Pr(Lava|Sim)$  and  $\Pr(\neg Lava|\neg Sim)$ ) give the likelihood of flow inundation or not inundation given the simulation results.

Once lava simulators have been successfully validated through benchmarking, these Bayesian statistics can be used to improve model input parameters and evaluate model

uncertainty by incorporating uncertainty inherent in input parameters. It is also possible that the two posterior predictive values can be used to aid in decision making processes associated with active lava flow crises.

## 2.7 Data Statement

This code is available for free use on GitHub at the USFVolcanology page located at <https://github.com/USFvolcanology>, while the benchmarking codes can be found at [https://github.com/jarichardson/MOLASSES\\_benchmarking](https://github.com/jarichardson/MOLASSES_benchmarking). The MOLASSES code and the Benchmarking algorithms are kept in separate self-contained repositories.

## 2.8 References

- Aspinall, W., Woo, G., Voight, B., and Baxter, P. (2003). Evidence-based volcanology: application to eruption crises. *Journal of Volcanology and Geothermal Research*, 128(1):273–285.
- Avolio, M. V., Crisci, G. M., Di Gregorio, S., Rongo, R., Spataro, W., and Trunfio, G. A. (2006). Sciara  $\gamma$ 2: An improved cellular automata model for lava flows and applications to the 2002 etnean crisis. *Computers & Geosciences*, 32(7):876–889.
- Barca, D., Crisci, G., Gregorio, S. D., and Nicoletta, F. (1994). Cellular automata for simulating lava flows: a method and examples of the etnean eruptions. *Transport theory and statistical physics*, 23(1-3):195–232.
- Bayarri, M. J., Berger, J. O., Paulo, R., Sacks, J., Cafeo, J. A., Cavendish, J., Lin, C.-H., and Tu, J. (2007). A framework for validation of computer models. *Technometrics*, 49(2).
- Belousov, A., Belousova, M., Edwards, B., Volynets, A., and Melnikov, D. (2015). Overview of the precursors and dynamics of the 2012–13 basaltic fissure eruption of tolbachik volcano, kamchatka, russia. *Journal of Volcanology and Geothermal Research*, 299:19–34.

Connor, L. J., Connor, C. B., Meliksetian, K., and Savov, I. (2012). Probabilistic approach to modeling lava flow inundation: a lava flow hazard assessment for a nuclear facility in armenia. *Journal of Applied Volcanology*, 1(1):1–19.

Crisci, G., Iovine, G., Di Gregorio, S., and Lupiano, V. (2008). Lava-flow hazard on the se flank of mt. etna (southern italy). *Journal of Volcanology and Geothermal Research*, 177(4):778–796.

Crisci, G. M., Rongo, R., Di Gregorio, S., and Spataro, W. (2004). The simulation model sciara: the 1991 and 2001 lava flows at mount etna. *Journal of Volcanology and Geothermal Research*, 132(2):253–267.

Damiani, M. L., Groppelli, G., Norini, G., Bertino, E., Gigliuto, A., and Nucita, A. (2006). A lava flow simulation model for the development of volcanic hazard maps for mount etna (italy). *Computers & geosciences*, 32(4):512–526.

Del Negro, C., Fortuna, L., Herault, A., and Vicari, A. (2008). Simulations of the 2004 lava flow at etna volcano using the magflow cellular automata model. *Bulletin of Volcanology*, 70(7):805–812.

Glaze, L. and Baloga, S. (2003). Dem flow path prediction algorithm for geologic mass movements. *Environmental & Engineering Geoscience*, 9(3):225–240.

Griffiths, R. (2000). The dynamics of lava flows. *Annual Review of Fluid Mechanics*, 32(1):477–518.

Harris, A. J. and Rowland, S. (2001). Flowgo: a kinematic thermo-rheological model for lava flowing in a channel. *Bulletin of Volcanology*, 63(1):20–44.

Hidaka, M., Goto, A., Umino, S., and Fujita, E. (2005). Vtfs project: Development of the lava flow simulation code lavasim with a model for three-dimensional convection, spreading, and solidification. *Geochemistry, Geophysics, Geosystems*, 6(7).

- Ishihara, K., Iguchi, M., and Kamo, K. (1990). Numerical simulation of lava flows on some volcanoes in japan. In *Lava Flows and Domes*, pages 174–207. Springer.
- Jeffreys, H. (1998). *The theory of probability*. OUP Oxford.
- Kauahikaua, J., Margriter, S., Lockwood, J., and Trusdell, F. (1995). Applications of gis to the estimation of lava flow hazards on mauna loa volcano, hawai'i. *Mauna Loa Revealed: structure, composition, history, and hazards*, pages 315–325.
- Kilburn, C. (2000). Lava flow and flow fields. In Sigurdsson, H., editor, *Encyclopedia of Volcanoes*, pages 331–343. Academic Press, San Diego, CA.
- Kubanek, J., Richardson, J. A., Charbonnier, S. J., and Connor, L. J. (2015). Lava flow mapping and volume calculations for the 2012–2013 tolbachik, kamchatka, fissure eruption using bistatic tandem-x insar. *Bulletin of Volcanology*, 77(12).
- Marzocchi, W. and Woo, G. (2007). Probabilistic eruption forecasting and the call for an evacuation. *Geophysical Research Letters*, 34(22):n/a–n/a. L22310.
- Miyamoto, H. and Sasaki, S. (1997). Simulating lava flows by an improved cellular automata method. *Computers & Geosciences*, 23(3):283–292.
- Peterson, D. and Tilling, R. (2000). Lava flow hazards. In Sigurdsson, H., editor, *Encyclopedia of Volcanoes*, pages 957–971. Academic Press, San Diego, CA.
- Rodríguez, E., Morris, C. S., and Belz, J. E. (2006). A global assessment of the srtm performance. *Photogrammetric Engineering & Remote Sensing*, 72(3):249–260.
- Woo, G. (2008). Probabilistic criteria for volcano evacuation decisions. *Natural Hazards*, 45(1):87–97.

### **3. The Volcanic History of Syria Planum, Mars<sup>2</sup>**

#### **3.1 Abstract**

A field of small (10s km in diameter) volcanoes in the Syria Planum region of Mars is mapped to determine abundance, distribution, and alignments of vents. These data are used to assess possible variations in eruption style across space and time. Each eruption site is assigned a point location. Nearest neighbor and two-point azimuth analyses are conducted to assess the spacing and orientations between vents across the study area. Two vent fields are identified as unique volcanic units along with the previously identified Syria Mons volcano. Superposition relationships and crater counts indicate that these three volcanic episodes span ~900 Ma, beginning in the early Hesperian and ending in the Early Amazonian. No clear hiatus in eruptive activity is identified between these events, although a progression from eruptions at Syria Mons, to regionally distributed eruptions that form the bulk of the Syria Planum plains, to a final migration of dispersed eruptions to Syria's northwest is identified. Nearest neighbor analyses suggest a non-random distribution among the entire population of Syria Planum, which is interpreted as resulting from the interaction of independent magma bodies ascending through the crust during different stress regimes throughout the region's eruptive history. Two-point azimuth results identify three orientations of enhanced alignments, which match well with radial extensions of three major tectonic centers to the south, east, and northwest of the study area. As such, Syria Planum volcanism evolved from a central vent volcano to dispersed shield field development over several hundred million years, during which the independent magma bodies related to each small volcano interacted to some extent with one or more of at least three buried tectonic patterns

---

<sup>2</sup>This chapter has been reprinted from the Journal of Volcanology and Geothermal Research with permission from XXX as: Richardson, J. A., Bleacher, J. E., Glaze, L. S., (2013), The Volcanic History of Syria Planum, Mars, Journal of Volcanology and Geothermal Research, 252, 1-13.

in the older crust. These results show a strong relationship between independent mapping efforts of tectonic and volcanic features. Continued integration of volcano–tectonic mapping should provide direct constraints for future geodynamic models of magma production and thermal evolution of the Tharsis province.

### 3.2 Introduction

The Tharsis province is a volcanic rise extending over 4500 km across the western hemisphere of Mars, covering nearly a quarter of the planet’s surface (Hodges and Moore, 1994). This region is suggested to display volcanic and tectonic activity into the late Amazonian (Anderson et al., 2001; Neukum et al., 2004) (Martian chronology is detailed briefly in Section 3.3.3). The region is long recognized to include five major shield volcanoes, seven partly buried volcanoes, vast lava plains, and a wide range of smaller eruptive vents (Carr et al., 1977; Greeley and Spudis, 1981; Mouginis-Mark et al., 1992; Hodges and Moore, 1994). While twelve large named volcanoes are cataloged and their morphologies and morphometries described in detail (Hodges and Moore, 1994; Plescia, 2004, and references therein), small volcanic edifices (10s km in diameter) have received much less attention due to a lack of high resolution data with regional coverage prior to the Mars Global Surveyor (MGS) mission.

The acquisition of post–*Viking* data enables for the first time detailed cataloging and morphologic descriptions of the wide range of small volcanic vents (hereafter referred to as small vents) in the Tharsis province (Baptista et al., 2008; Baratoux et al., 2009; Bleacher et al., 2007, 2009; Brož and Hauber, 2012; Hauber et al., 2009, 2011; Keszthelyi et al., 2008; Wilson et al., 2009). This ability represents a critical step forward in the scientific understanding of Martian magma production and eruption. Because different types of volcanic features result from a combination of different eruptive conditions, magma and lava properties, and ambient variables (Greeley, 1977; Whitford-Stark, 1982), an understanding of the abundance and distribution of volcanic features serves as a fundamental framework that is

needed to fully understand any volcanic system (Head et al., 1981; Connor and Conway, 2000).

Here we report on mapping and analyses of the vent fields within the Syria Planum region of Mars (Baptista et al., 2008). This is a portion of an ongoing investigation to catalog the location of small (10s km in diameter) vents across the Tharsis region. Although each vent appears minor in areal coverage and volume compared to the larger Tharsis shield volcanoes, when considered together as vent fields comparable to the Snake River Plain in Idaho, USA (Greeley, 1977, 1982), they represent significant magma production events. In addition to the volume of lava visible on the surface, the entire crust of the Tharsis region appears to have been demagnetized (Connerney et al., 2005; Lillis, 2006). The passage of many small magma packages into and through the crust provides a plausible explanation for this demagnetization in areas that are hundreds of kilometers away from major shield volcanoes (Lillis et al., 2009). Likewise, tectonic evidence has led to the suggestion that the Tharsis province has experienced multiple episodes of large mantle upwellings (Plescia and Saunders, 1982; Mege and Masson, 1996; Anderson et al., 2001, 2004; Wilson and Head, 2002), the centers of which are not necessarily spatially overlapping with major volcanoes. Anderson et al. (2001, 2004) refer to these events as magmatic-driven tectonic episodes, which is consistent with the identification of vent fields in the Tharsis plains. As such, it is critical to assess the number, location, and duration of magma production events that contributed to the current morphology of the Tharsis region.

### 3.2.1 Geologic Description

Past mapping of Syria Planum has enabled the identification of several distinct units based on morphologic characteristics. Baptista et al. (2008) identified three distinct units in southwestern Syria: 1) a unit comprised of NW-trending graben, 2) lava flows associated with Syria Mons, and 3) a field of coalesced low shield volcanoes. The lava flows associated with Syria Mons are hundreds of kilometers in length and form kilometers-wide, finger-like sheets of lava throughout the unit. These flows embay the graben field, which is composed of

narrow (100s of meters to kilometers) linear and curvilinear graben that are tens to hundreds of kilometers in length. The Syria Mons flows are crosscut by NE–SW trending graben, 10s of km in length. The coalesced shield field is composed of low shield volcanoes several kilometers in diameter that embay the Syria Mons lava flows. Both the field and the flows are crosscut with NW–SE trending graben (km in length). A newly identified geologic unit (Hnsf in Figure 3.1) is located to the north of the Baptista et al. (2008) study area and is seen to embay the coalesced shield field to the south. It is characterized by lava flows tens to hundreds of kilometers in length emanating from a topographic ridge approximately 200km in length that trends NE–SW. The lava flows that form this unit are seen to fill preexisting graben that crosscut the southern coalesced shield field and embay vents from the southern shield field.

The mapping of Baptista et al. (2008) was limited by High Resolution Stereo Camera (HRSC) data availability to 100-105°W, 13-23°S within the Syria region. Despite this limitation, Baptista et al. (2008) demonstrated that analysis of high resolution image data with regional coverage showed new volcanic and tectonic complexities in this region that had previously been identified as a plains style volcanic province (Sakimoto et al., 2003) similar to those described on the Earth (Greeley, 1982), and other Mars volcanic field studies (Bleacher et al., 2007, 2009; Hauber et al., 2009). The addition of several tectonic episodes that temporally separate volcanic emplacement events leads to the hypothesis that Syria Planum is the surface product of multiple (opposed to one long-lived) magma production events. For clarity, we use the term “magma production event” to represent a broad magmatic upwelling that might feed multiple shallow, crustal magma bodies and small volcanic vents across a region like Syria. Such an event might be comparable to an event that feeds a major shield like Olympus Mons or each of the Tharsis Montes, and should be considered in models of the thermal and geologic evolution of Tharsis. Therefore, it is imperative to determine if a large field of vents like Syria represents one magma production event, or possibly multiple, temporally distinct events that are spatially overlapping on the surface of the planet.

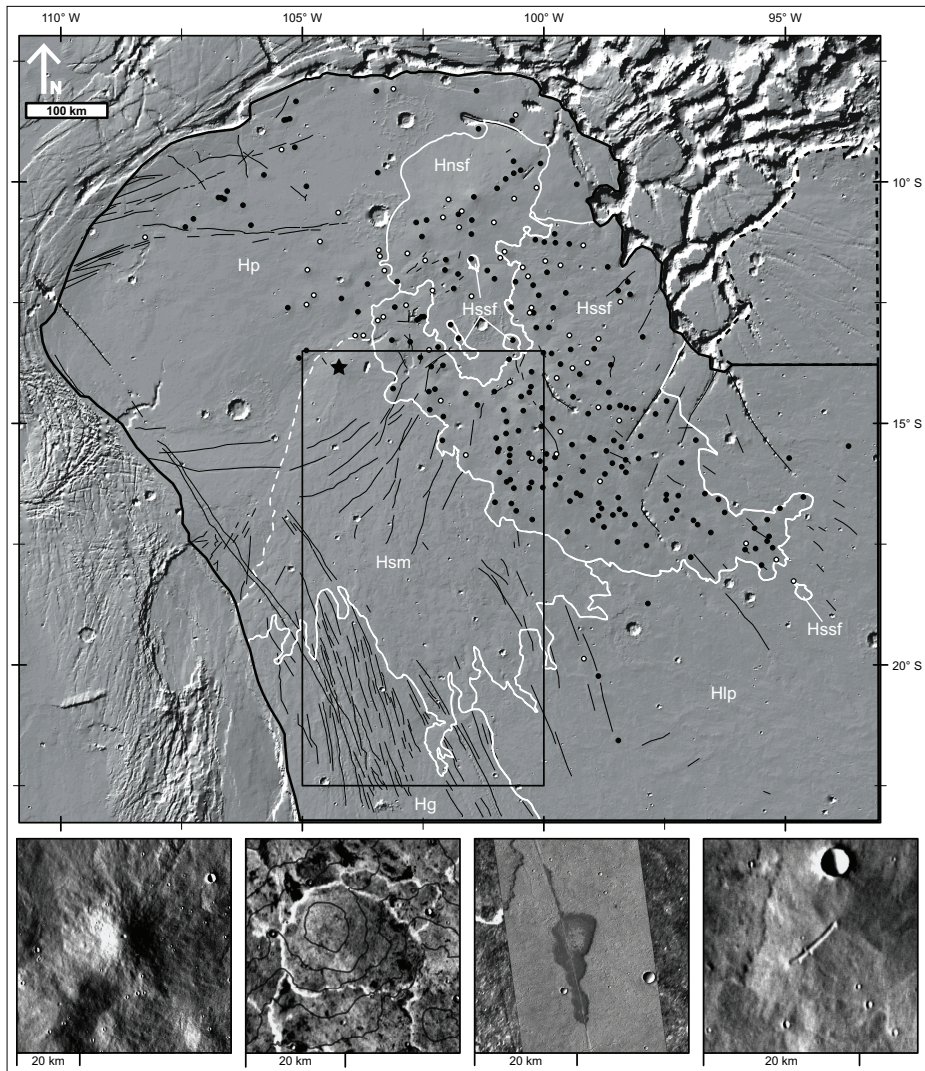


Figure 3.1: Geologic Map of Syria Planum. The study area is shown inside the thick black line with a MOLA-derived hillshade basemap. The study area of Baptista et al. (2008) is shown as a rectangle in the south-central region of the study area. In the east a dotted line surrounds an area where no volcanic vents are found and is therefore not included in the study area (crater counting was not performed in this area). Volcanic vents are represented as a solid black point, likely volcanic vents as a white point outlined in black, and Syria Mons is represented as a star. Graben are shown as thin black lines. White lines separate geologic units. From north to south these units are: Hp, a unit on the margins of the plateau that features scattered individual vents; Hnsf, a northern shield field of coalesced volcanic vents; Hssf, a southern shield field of coalesced volcanic vents; Hsm, lava flows of Syria Mons; Hg, a graben-rich unit; Hlp, a unit of lava flows on the southeast margin of Syria Planum that hosts relatively few volcanic vents.

In order to test this hypothesis we map volcanic vents in the full Syria Planum region at comparable resolutions to the study of Baptista et al. (2008), which is only now possible due to the combined data acquisition of HRSC, Thermal Emission Imaging System (THEMIS), and Context Imager (CTX) images. Our objectives are to determine if multiple separable magma production events occurred in Syria and to assess whether these events can be clearly identified as unique events or the extension of a long-lived, continuous magma production event, either of which provide new insight into and modeling constraints for the thermal and tectonic evolution of the Tharsis province.

In this paper, new spatio-temporal boundaries of known volcanic units are presented and a new volcanic unit in the north of Syria is identified, separated from southern volcanism by a distinct flow margin. Each volcanic unit in Syria Planum is temporally constrained with superposition relationships and crater age-dating. Methods which are used to spatially describe small volcanic vents in Syria are then discussed, including nearest neighbor and 2-point azimuth statistical analyses. Finally, a revised volcano-tectonic history of Syria Planum is proposed, wherein we interpret that volcanism has likely migrated spatially throughout the evolution of Syria and wherein the style of volcanism has likely shifted from one central vent at Syria Mons to forming coalesced shield fields.

### 3.3 Methods

#### 3.3.1 Study Area

The study area (Figure 3.1), Syria Planum, is located on the southeastern margin of the Tharsis province between 8-23°S and 110-93°W. Syria Planum is bordered by Noctis Labyrinthus to the north, Claritas Fossae to the west and Solis Planum to the southeast. This area forms a regional plateau with a maximum elevation of 8000 m based on analysis of Mars Orbiter Laser Altimeter (MOLA) (Smith et al., 2003) gridded data. A total relief of 4000 m exists between this point and the southeastern portion of the study area. The study area is roughly 1000 by 900 km in size as defined by Scott and Tanaka (1986), with an abundance of volcanic vents focused in an area roughly 700 by 600 km in size (Richardson

et al., 2010; Richardson et al., 2012). In order to characterize the volcanic evolution of Syria all identifiable volcanic vents in the study area are mapped and morphologic units are identified as temporally separable by crater counting. Nearest neighbor and 2-point azimuth statistical analyses are applied to the vent location data to provide additional constraints on the evolution of the volcanic region. A 512 pixels-per-degree (ppd) THEMIS infrared (IR) day-time mosaic (Christensen et al., 2004) and the 128 ppd MOLA gridded dataset (Smith et al., 2003) are used as base maps. Relevant CTX (Malin et al., 2007) and THEMIS visible (VIS) (Christensen et al., 2004) images are co-registered to this base map for the identification of volcanic vents.

### 3.3.2 Catalog of Volcanic Vents

Volcanic vents are spatially cataloged as single points in a Cartesian grid, referencing their plan view position with respect to the THEMIS IR day-time mosaic and the gridded MOLA dataset base maps. Each datum is assumed to closely represent the four-dimensional (space and time) pathway along which magma ascended through the crust to erupt at the surface and produce an identifiable vent structure (Bishop, 2007). Volcanic vents are here defined as positive topographic landforms, tens to hundreds of meters in height, with flows or flow-like textures radiating from the apex and/or depressions at the topographic summit. Many positive topographic landforms lack clear flow features or a preserved depression at the apex, but are otherwise morphologically similar to cataloged vents. These landforms, which are tens to hundreds of meters in height, are also cataloged as likely volcanic vents (an example with contours is shown in Figure 3.1). It is assumed that many volcanic vents that formed within the volcanic field on Syria Planum have since been buried by continued volcanism. This mapping project does not consider these buried vents, nor does this study provide any assumptions about stalled magma bodies for which ascension pathways were established but did not lead to surface eruptions (in other words, the intrusion to extrusion ratio of the region as was estimated in southern Tharsis by Lillis et al. (2009)). Instead, vents that are currently identifiable on the surface are assumed to represent the last stage of

eruptive activity in the region and are used to provide new insight into the magmatic and volcanic history of Syria and the Tharsis province.

A variety of volcanic vent morphologies are present on Tharsis and have recently been characterized using post-*Viking* era image data (Bleacher et al., 2007, 2009; Brož and Hauber, 2012; Keszthelyi et al., 2008; Baptista et al., 2008; Hauber et al., 2009; Wilson et al., 2009; Baratoux et al., 2009). Different methods are implemented for different vent morphologies to realistically assign a representative two-dimensional point to this four-dimensional process. For volcanic vents with depressions at the summit from which lava has visibly erupted (based on interpretation of radiating textures or buildup of spatter or cinder rims (examples in Figure 3.1)) a data point is digitally created at the center of the depression using ArcGIS 9.3. For volcanic vents with linear depressions along a topographic high, the data point is created at the midpoint of a line with endpoints at the extents of the depression. In cases where the depression extends beyond the apparent eruptive activity (in other words, an extended dry fracture associated with the eruptive segment of the fissure as discussed by Greeley (1977) in volcanic fields) the data point is assigned at the middle point of a line connecting the ends of the eruptive segment. For likely volcanic features, which do not display summit depressions, data points were assigned at the topographic summit of the feature or at the origin of radiating flow textures where possible.

Cataloging the location of volcanic vents within Syria also enables the identification of distinct large scale flow features and units based on different morphological and superposition characteristics. Consistent superposition relationships among vent groups within Syria are identified. Using the map of vent locations (Figure 3.1) and superposition relationships for Syria Planum, several techniques are applied to further characterize the region's eruptive history. Based on the identification of unique vent groups, crater counts (described in Section 3.3.3) are conducted to test whether quantifiable hiatuses occurred between the formation of different volcanic and tectonic events. Nearest neighbor analysis (described in Section 3.3.4) is applied to the complete Syria vent catalog and to subgroups of vents within the study

area based on morphological mapping units. Nearest neighbor analysis is applied to assess the spatial distribution among vents. This has been shown as a method of characterizing a group of data points as being composed of one or a combination of populations (Bishop, 2007; Baloga et al., 2007). A two-point azimuth technique (described in Section 3.3.5) is implemented to identify potential lineaments between volcanic vents that might correlate to underlying structures (Lutz, 1986; Wadge and Cross, 1988, 1989; Connor, 1990; Lutz and Gutmann, 1995; Bleacher et al., 2009) in an attempt to better understand the ascent of magma beneath Syria. The combination of such spatial and alignment analyses has been used to characterize volcanic fields on the Earth (Lutz, 1986; Lutz and Gutmann, 1995; Cebriá et al., 2011; Roberts et al., 2011) and Mars (Bleacher et al., 2009).

### 3.3.3 Crater Counting

Using the 512ppd THEMIS infrared daytime mosaic, craters larger than 0.5 km in diameter are cataloged in accordance with identified vent groups and morphologic units. For each morphologic unit, a crater retention age is fitted to a cumulative crater size–frequency distribution following the method described in Hartmann (2005) and using the freely available software Craterstats2 (Michael and Neukum, 2010). The size–frequency distribution is fit to a production function from Ivanov (2001) and an absolute age is calculated using the chronology model from Hartmann and Neukum (2001).

Given the relatively large surface area of each morphologic unit (e.g. one unit is composed of >100 volcanic shields) and the relatively low spatial resolution of the THEMIS mosaic (100 m), isochrons for this study are fit using craters of diameter  $\geq 1$  km. Craters of diameter  $< 1$  km are not used for determining ages due to the tendency for the number of smaller craters to artificially diminish as their diameter approaches the resolution of the base map.s Crater retention rates are reported with errors following the equation

$$N(1) = \frac{n_{1km}}{A} \pm \frac{\sqrt{n_{1km}}}{A} \quad (3.1)$$

where  $n_{1km}$  is the observed number of craters with diameters greater than 1 km and  $A$  is the surface area in  $\text{km}^2$ .

Ages determined by crater age-dating are assigned an epoch range based on the Martian chronostratigraphic system as recently outlined by Werner and Tanaka (2011). Generally, the three periods of the Martian system are the Noachian, Hesperian, and Amazonian, ranging from >3.96-3.57 Ga, 3.57-3.00 Ga, and 3.00 Ga-present, based on the chronology model of Hartmann (2005), respectively. These periods are further separated into epochs as follows: Middle Noachian, 3.96-3.85 Ga; Late Noachian, 3.85-3.57 Ga; Early Hesperian, 3.57-3.40 Ga; Late Hesperian, 3.40-3.00 Ga; Early Amazonian, 3.00-0.88 Ga; Middle Amazonian, 0.88-0.24 Ga; Late Amazonian, 0.24 Ga to present.

### 3.3.4 Nearest Neighbor Analysis

The distances from each volcanic vent to its nearest neighboring vent in a volcanic field can be used to characterize the spatial distribution of the volcanic vents within a field. It has been hypothesized that the vents of a terrestrial volcanic vent field (i.e. field volcanism) will conform to a random spatial distribution (Lutz, 1986; Lutz and Gutmann, 1995). This is to say that each vent is located in the study area independently of the location of any other vent, that each vent has the same probability of occurrence at any location in the study area, and that any subarea of the study area is equally likely to contain any vent as any other identically sized study area (Clark and Evans, 1954).

Based on the Poisson spatial distribution, Clark and Evans (1954) defined two statistics with which to analyze nearest neighbor (NN) distances for a spatial distribution of points. First, the test statistic,  $c$ , is given by the equation

$$c = \frac{\bar{r}_a - \bar{r}_e}{\sigma_e}, \quad (3.2)$$

where  $\bar{r}_a$  is the mean observed NN distance,  $\bar{r}_e$  is the expected mean NN distance for a Poisson spatial distribution, and  $\sigma_e$  is the expected standard deviation of NN distances. Expected

values of  $c$  were simulated by Baloga et al. (2007) to remove bias based on sample size. If the observed  $c$  statistic departs from the expected  $c$  by more than  $2\sigma$  for the appropriate sample size, spatial randomness may be rejected.

Second, the ratio between the observed mean NN distance,  $\bar{r}_a$ , and the expected mean NN distance,  $\bar{r}_e$ , given by equation 3.3, also tests the fit of Poisson randomness.

$$R = \frac{\bar{r}_a}{\bar{r}_e} \quad (3.3)$$

If a vent field is spatially random in a Poisson sense, the  $R$ -index will approach 1. Values of  $R > 1$  suggest that the points approach maximal packing, while values of  $R < 1$  suggest that points are more clustered than expected for a Poisson spatial distribution. Similar to the test statistic  $c$ , the calculated  $R$ -index may be compared to an expected  $R \pm 2\sigma$  to test for the fit of Poisson randomness to describe the distribution of points.

Baloga et al. (2007) also developed a test using the skewness and kurtosis of the NN distribution to further constrain the applicability of the Poisson distribution to a spatial sample. Using 1000 simulated Poisson point sets of the same sample size, it was observed that skewness and kurtosis are strongly correlated and focus around an elliptical centroid. If the skewness and kurtosis values for a given point set plot sufficiently far away from the centroid of simulated Poisson values, randomness in the Poisson sense may again be rejected.

Nearest neighbor analysis described above can be used to quantitatively compare the spatial distribution of volcanic vents with the null hypothesis,  $H_o$ , of spatial randomness in a Poisson sense. We hypothesize that if the vents are spatially random in the Poisson sense, then the vents have formed independently of each other as part of one larger magma production event (e. g. their respective magma ascension pathway through the crust was not influenced by the location of any other vent thereby causing a random spacing of eruption points). If a Poisson distribution is rejected and the  $R$ -index statistic shows evidence for clustering, we interpret the result as evidence that multiple temporally distinct magma pro-

duction events have occurred beneath Syria Planum that are spatially overlapping, thereby resulting in two or more random but mixed statistical populations (Lutz, 1986; Lutz and Gutmann, 1995).

To perform nearest neighbor analysis, Geological Image Analysis Software (GIAS), version 1.12, was used (Beggan and Hamilton, 2010; Hamilton et al., 2010, 2011).

### 3.3.5 Two-point azimuthal analysis

Two-point azimuth techniques have been used to observe and describe lineaments between volcanic vents for decades (Lutz, 1986; Wadge and Cross, 1988, 1989; Connor, 1990; Lutz and Gutmann, 1995; Bleacher et al., 2009; Cebriá et al., 2011; Roberts et al., 2011). Azimuth techniques determine the directions from each point to every other point. Lineaments between vents are identified by looking at anomalously high numbers of azimuths in any given direction and comparing that with other linear features, such as faults and graben, observed in the area or in adjacent, older terrains for which their traces might have been buried by the emplacement of the volcanic field or other geologic processes.

Cebriá et al. (2011) postulated that lineaments between two vents are more likely if those vents are relatively close to each other. They therefore suggested that two point azimuth techniques should use a *minimum significant distance*, a distance where the azimuths of closer inter-vent relationships best characterize lineaments of the given field. Inter-vent relationships farther than this minimum significant distance are not as likely to be related by the same underlying geological structures. Adding to the benefit of using only inter-vent relationships smaller than this distance is that anomalously far inter-vent relationships will likely display bias in the direction of the vent field's major axis. If the vent distribution for example, resembles a narrow ellipse due to topographic focusing, the longer inter-vent relationships will necessarily point in the direction of the long axis of the ellipse even if regional tectonic patterns are perpendicular.

For this study, the minimum significant distance used is defined by Cebriá et al. (2011)

$$d \leq (\mu_v - 1\sigma_v)/3 \quad (3.4)$$

where  $\mu_v$  is the mean inter–vent distance and  $\sigma_v$  is the standard deviation of inter–vent distances. Using the set of inter–vent relationships shorter than this distance, relationships are grouped by direction into nine bins of a rose diagram. We hypothesize that bins containing an anomalous amount (count  $\geq \bar{x}_n + \sigma_n$ ) of inter–vent relationships are evidence of lineaments between vents. These orientations are compared with regional tectonic trends as possible influences of magma ascension (Bleacher et al., 2009; Cebriá et al., 2011).

## 3.4 Results

### 3.4.1 Mapping

In the study area 263 vents are identified, with 206 cataloged as volcanic vents and 57 cataloged as likely volcanic vents. There is no specific area where likely volcanic vents (as opposed to volcanic vents) are concentrated, though the highest abundance of likely volcanic vents are in northern Syria Planum. Because of the likely volcanic vents' regional distribution and topographic similarity to landforms cataloged as volcanic vents, we have included likely volcanic vents in the statistical analysis of all volcanic vents on Syria Planum. Here after both categories of vents are treated as one catalog, which includes 263 features.

The 263 identifiable vents within Syria Planum are distributed among five of six identified map units on Syria, which are delineated based on observed superposition relationships. Cataloged volcanic vents, geologic units, and graben are plotted in Figure 3.1. A graben–rich unit previously described by Baptista et al. (2008) and Tanaka and Davis (1988), Hg, is located in the southwest of the study area and is seen to be embayed by the lavas of the Syria Mons unit, Hsm. Lavas associated with Syria Mons cover much of the study area and extend at least several hundreds of kilometers from Syria Mons' main vent towards the southeast. The Syria Mons summit is the only vent cataloged in this unit. The

boundaries of the Syria Mons unit are defined to the west and south by the margins of distinct, overlying lava flows. To the east, the Syria Mons unit is embayed by low shields that coalesce into a volcanic vent field, Hssf. Syria Mons and thirty volcanoes that make up this coalesced vent field unit were extensively mapped by Baptista et al. (2008). The majority of vents cataloged in Syria Planum, 192, are cataloged in this vent field. Low shields that coalesce to form this unit have slopes 1-2.5° and diameters between 10 and 35 kilometers. Eight vents are identified in this unit that have slopes up to 6° and diameters of 2-10 km. The low shields of this unit extend into the southeast where they flow over a unit of large scale lava flows, Hlp, that extend from a center within Syria Planum, which is unrecognized at this time. In this southeastern unit, 6 vents are cataloged.

To the north of the coalesced unit are distinct flow margins. The lava that created these flow margins embay low shields associated with the coalesced unit and fill graben that have cross-cut the coalesced unit. The source of the embaying lava flows to the north is a unit comprised of 22 vents that form a second coalesced volcanic vent field. To distinguish between these two coalesced volcanic units, the field to the south, Hssf, is labeled as the “southern shield field” and the field to the north, Hnsf as the “northern shield field.” The northwestern boundary of the northern shield field is determined by the extent of visible lava flows, which extend to the north and south of the vents as far as 200 km. The northwest region of the study area is identified as one unit, Hp, beyond the lava flows of Syria Mons and the northern shield field. The northwestern unit contains 42 vents, which do not coalesce together to make one distinct field. The relative superposition of this unit to the Syria Mons lava flows and the northern shield field are not clearly defined.

The vents of the two coalesced shield fields are identified as subgroups within the catalog of Syria Planum vents and are used for statistical analysis in this study. The locations of volcanic vents cataloged in the study area are summarized in Table 3.1. Because the flow fronts farthest from, but still associated with, the northern shield field are buried by successive flow fronts closer to the observed vents of the shield field, their temporal connection

Table 3.1: Summary of Vent Counts in Defined Units

	Volcanic Vents	Likely Volcanic Vents	Total Vents
Northern Shield Field, <i>Hnsf</i> *	13	9	22
Southern Shield Field, <i>Hssf</i> *	159	33	192
Syria Mons Unit, <i>Hsm</i>	1	0	1
Northwest Syria Planum, <i>Hp</i>	28	14	42
Southeast Syria Planum, <i>Hlp</i>	4	2	6
Totals	205	58	263

\*Nearest neighbor analysis is performed on the vent populations of the northern and southern shield fields and the combination of these fields.

Table 3.2: Crater Retention Rates and Ages for Selected Units

	$10^{-3} N(1)$ craters $\text{km}^{-2}$	Age, Ga	Epoch*
Northern Shield Field, <i>Hnsf</i>	$1.4 \pm 0.2$	2.56-3.23	Late Hesp. to Early Amaz.
Northwest Syria Planum, <i>Hp</i>	$1.5 \pm 0.1$	3.17-3.29	Late Hesp.
Intermediate Flows, <i>Hnsf?</i>	$1.7 \pm 0.4$	3.28-3.52	Early to Late Hesp.
Southern Shield Field, <i>Hssf</i>	$1.7 \pm 0.1$	3.23-3.35	Late Hesp.
Southeast Syria Planum, <i>Hlp</i>	$1.8 \pm 0.1$	3.33-3.40	Late Hesp.
Syria Mons Unit, <i>Hsm</i>	$2.0 \pm 0.1$	3.41-3.47	Early Hesp.
Graben Basement, <i>Hg</i>	$2.2 \pm 0.2$	3.37-3.46	Early to Late Hesp.

\*Hesp.: Hesperian; Amaz.: Amazonian.

to the observed vents is not confirmable. For this reason, geologically lower flow fronts which are embayed by flows and are not able to be connected to northern shield field vents are described as intermediate flows in age-dating exercises discussed in Section 3.4.2.

### 3.4.2 Age-Dating

In Table 3.2 and illustrated graphically in Figure 3.2, crater counts and their corresponding age-dates are presented. According to these counts, the last lava flowed over the surface of Syria Planum as recent as the early Amazonian. Crater dating also shows that the lavas from Syria Mons and the graben-rich basement that they embay, which are the lowest observed geologic units, were last significantly resurfaced during the early Hesperian epoch.

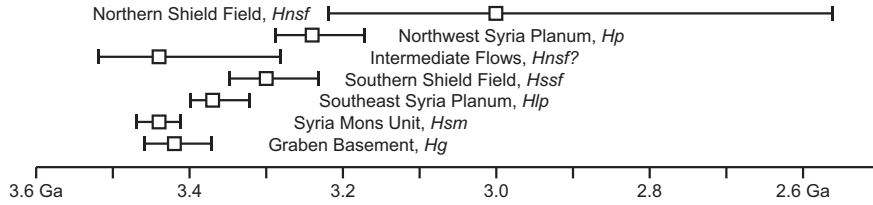


Figure 3.2: Graphical summary of age-dating results by unit.

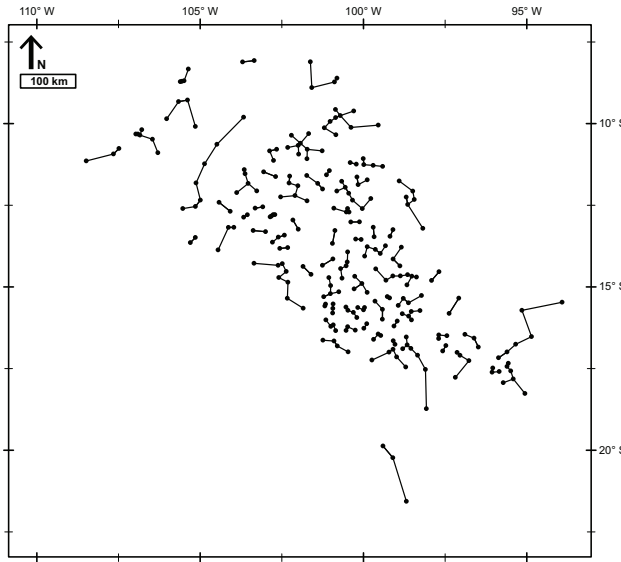


Figure 3.3: Plot of vents with lines drawn to their nearest neighbors.

Using superposition, volcanic units are relatively dated with Syria Mons erupting first, low shields of the southern shield field embaying its flows, and lavas of the northern shield field embaying the southern shield field. As shown in Figure 3.2, error bars between ages of flows associated with Syria Mons, the southern shield field, and the northern shield field do not overlap and are in agreement with superposition observations. However, no significant hiatus exists between the development of each unit. While some units seem ambiguously dated with respect to superposition (e.g. the graben-rich basement unit upon which are flows from Syria Mons is dated to be younger than the Syria Mons flows), no unit is in direct disagreement with relative dating observations, within error.

Table 3.3: Summary of Nearest Neighbor Analysis on Cataloged Vents and two Subgroups of Vents

		$\bar{r}_e$	$\bar{r}_a$	$R_e$	$R$	$c_e$	$c$	S/K Plot
All Planum	Syria	18.7 km	16.5 km	$1.03 \pm 0.07$	0.88	$0.80 \pm 2.14$	-3.57	rejected
N&S Fields	Shield	13.6 km	14.7 km	$1.03 \pm 0.08$	1.11	$0.82 \pm 2.14$	2.20	rejected
Southern Field	Shield	13.6 km	15.4 km	$1.03 \pm 0.09$	1.09	$0.83 \pm 2.15$	2.29	accepted
Northern Field	Shield	14.9 km	12.3 km	$1.15 \pm 0.39$	1.25	$0.97 \pm 2.57$	1.82	accepted

$\bar{r}_e$ , the expected mean NN distance;  $\bar{r}_a$ , the observed mean NN distance;  $R_e$ , the expected  $R$ -index and acceptance range;  $R$ , the observed  $R$ -index value (from Equation 3.3);  $c_e$ , the expected  $c$  statistic and acceptance range;  $c$ , the observed  $c$  statistic (from Equation 3.2). The final column lists the results of the skewness/kurtosis plot tests, testing the null hypothesis of Poisson spacing at the 0.05 significance level.

### 3.4.3 Nearest Neighbor Analysis

Figure 3.3 is a map of all vents cataloged in Syria Planum with lines drawn to represent the connections from each vent to their nearest neighbor. Nearest neighbor analysis is conducted using these distances. Table 3.3 presents results of the nearest neighbor analyses. The first two columns of Table 3.3 give the expected and observed nearest neighbor distances for each area examined. The columns for  $R_e$  and  $c_e$  give the acceptance ranges for values of  $R$  (defined in Equation 3.3) and  $c$  (defined in Equation 3.2), respectively, based on sample size. The results of the skewness/kurtosis test are plotted in Figure 3.4. Each plot shows simulated values of skewness and kurtosis for 1000 random Poisson spatial distributions (in gray). When the black diamond (indicating observed skewness and kurtosis values) falls within the gray area, this indicates consistency with Poisson randomness. Inferences based on the skewness/kurtosis values shown in Figure 3.4 are summarized in the last column of Table 3.3.

All cataloged vents in the study area are first analyzed as a single group to test the null hypothesis,  $H_o$ , that the vents are spatially random in a Poisson sense. Spatial randomness

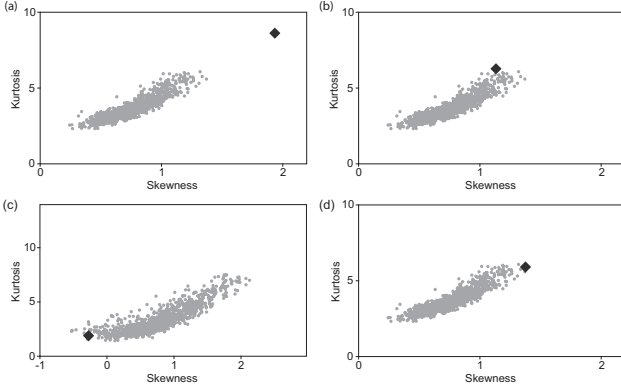


Figure 3.4: Plots of skewness vs. kurtosis values for 95% of 1000 simulated Poisson spatial distributions. Diamonds represent the corresponding experimental values for a) all catalogued vents on Syria Planum, b) vents in both shield fields, c) vents in the northern shield field, and d) vents in the southern shield field. Randomness is rejected for all vents and for the combined shield fields (a, b respectively) at the 0.05 significance interval and accepted for both shield fields (c,d) individually. Simulated Poisson spatial distributions for a, b, and d use 300 data points; for c, 30 data points.

of the entire study area could be evidence that a single magma production event may explain all volcanism in Syria Planum. However, due to the low  $R$ -index, the low  $c$  statistic, and the result of the skewness/kurtosis test where the field plotted outside the range of Poisson randomness at the 99% confidence interval, we reject the null hypothesis that the vents on Syria Planum are consistent with a Poisson spatial distribution when the entire study area is considered. Moreover, the observed  $R$ -index indicates that for all of Syria Planum the vents have a tendency to cluster, which is evidence that multiple subgroups might be identified as independent magma production events.

A subgroup that includes vents in both the northern and southern shield fields is also examined. Nearest neighbor results of this subgroup (N & S row in Table 3.3) inconclusively characterize the randomness of the combined field. The observed  $c$  statistic is within the predicted range, the  $R$ -index is calculated to be at the limit ( $R = 1.11$ ) of the expected  $R \pm 2\sigma$ , and the skewness and kurtosis values deviate from the elliptical centroid enough to reject randomness at the 0.05 significance level.

The vents within the northern shield field and the southern shield field are also analyzed individually to test their spatial randomness (Table 3.3). According to all three tests

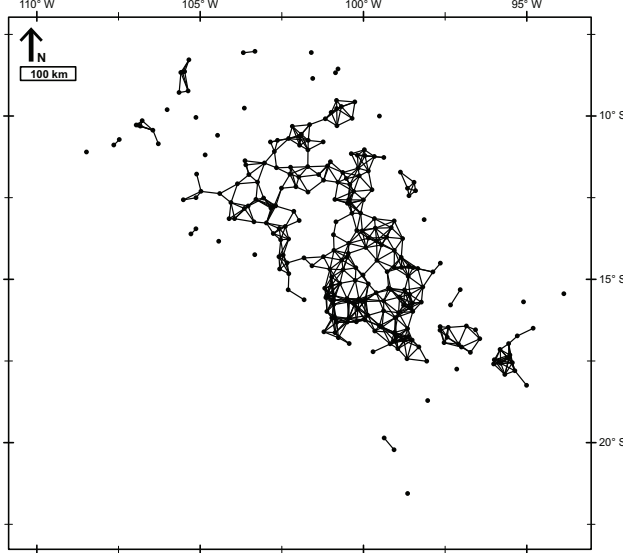


Figure 3.5: Plot of vents and all inter–vent relationships less than the minimum significant distance.

(the  $R$ -index, the  $c$  statistic, and the skewness/kurtosis test) both the northern shield field and the southern shield field are found to exhibit Poisson spatial randomness individually. Therefore the null hypothesis of spatial randomness cannot be precluded for these shield fields. It is important to note that the northern shield field includes only 22 vents, increasing uncertainty in this conclusion. However, as the southern shield field ( $n = 192$ ) clearly exhibits spatial randomness and the combination of the two shield fields produces an ambiguous spatial distribution, there is evidence to suggest that the two shield fields are statistically distinct.

#### 3.4.4 Two-point azimuthal analysis

Figure 3.6a displays a histogram of the lengths of all 34,453 inter–vent relationships. The skewness of this set of distances is 0.79. The mean distance,  $\mu$ , is 267 km and the standard deviation,  $\sigma$ , is calculated to be 157 km. The relationships used to investigate lineaments are below the minimum significant distance of  $\leq 36.9$  km as defined in Equation 3.4 (Cebriá et al., 2011). The number of inter–vent relationships,  $n$ , below the minimum significant distance, is 745. Figure 3.5 is a diagram of the vents represented as points in

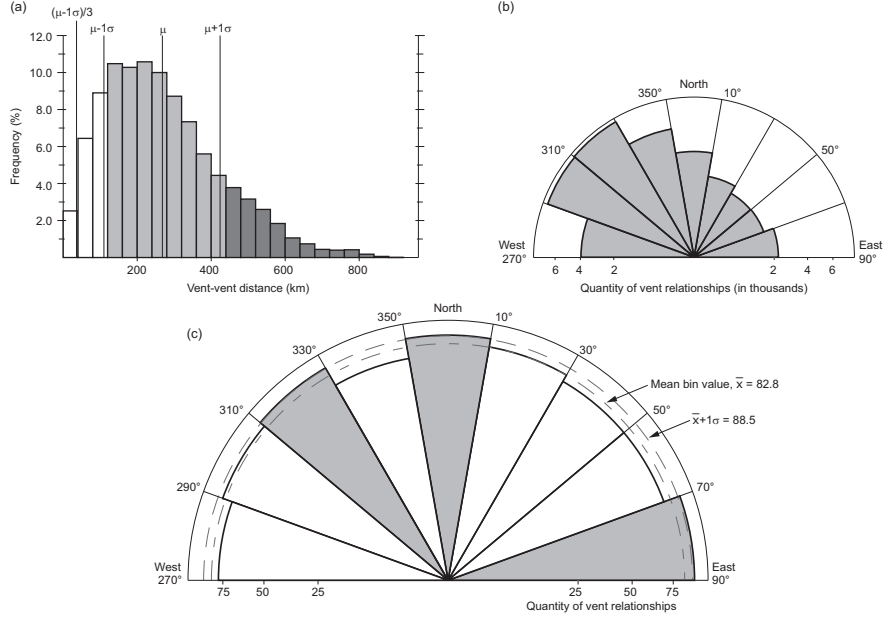


Figure 3.6: a) Distribution of inter–vent distances. Azimuths of inter–vent relationships are used if the inter–vent distance is less than 39.6 km, the defined minimum significant distance. Distances shaded dark gray are anomalously long and might trend in the overall vent field. Distances shaded light gray are of moderate length and are considered to be background noise. b) Directional distribution considering all inter–vent relationships. The plotted northwest mode is a result of including long distance inter–vent relationships. c) Directional distribution of inter–vent alignments below the minimum significant distance. The inner dotted line represents the mean quantity of inter–vent relationships. The outer dotted line represents the quantity of relationships one standard deviation above the mean. Directional wedges shaded gray ( $70\text{--}90^\circ$ ,  $310\text{--}330^\circ$ ,  $350\text{--}10^\circ$ ) have anomalously high quantities of inter–vent relationships.

two-dimensional Cartesian space, using their locations in meters, and relationships between vents that are below the minimum significant distance.

The rose diagram in Figure 3.6c illustrates the results of categorizing relationships based on the direction. The mean quantity of relationships in each direction bin,  $\bar{x}_n$ , is 82.8 and the standard deviation,  $\sigma_n$ , is 5.74. Three bins are identified as containing heightened amounts (count  $\geq \bar{x}_n + \sigma_n$ ) of inter–vent relationships:  $70\text{--}90^\circ$  ENE,  $350\text{--}10^\circ$  N, and  $310\text{--}330^\circ$  NW.

A rose diagram (Figure 3.6b) has been included, which illustrates the 2–point azimuth technique as applied to all inter–vent relationships, including those above the minimum

significant distance. The NW trend of the relationships is comparable to the NW trend of the overall vent field.

### 3.5 Discussion

Previous analyses of post-*Viking* era data show that the development of the Syria Planum region can be subdivided into a series of tectonic and volcanic episodes. The goal of this study is to provide additional detail to this sequence of events, and to determine if this region experienced one long-lived magmatic event or a series of magma production events. Building upon the work of Baptista et al. (2008) we present the following sequential volcano-tectonic development for the Syria Planum region based on superposition relationships. 1) Lava flows erupted from Syria Mons during the Early Hesperian (3.4-3.5 Ga), covering a recently (within hundreds millions of years) formed graben-rich basement unit. 2) Northeast faulting cross-cut the Syria Mons flows. 3) At 3.3-3.4 Ga during the Hesperian a southern shield field formed through the eruption of small volcanic vents in central Syria Planum to the NE of Syria Mons, which occurred contemporaneous to northwest faulting in the region of the vent field. 4) Volcanism continued throughout the northern region of Syria Planum from the Late Hesperian to the Early Amazonian (2.9-3.3 Ga), while concentrating to create a northeast trending ridge of coalesced vents north of and embaying the low shields of the southern shield field.

The most noticeable addition to the work of Baptista et al. (2008) is the separation of their coalesced shield field into a northern and southern coalesced vent field for which the northern is younger based on superposition. The delineation of two distinguishable vent fields in Syria, along with the development of Syria Mons, reveals at least three significant volcanic units or episodes. If these volcanic episodes all result from one magma production event then they display a migration and evolution in eruptive style as Syria volcanic units were emplaced through time. If not, then at least two, possibly more, magma production events produced the current surface of Syria Planum and should be considered in models of the overall development of the Tharsis province.

Crater counts of the units in this study (Table 3.2) are consistent with the inferred relative ages of the units based on superposition as presented above. Crater retention ages (Figure 3.2) suggest that currently preserved lavas flowed across the Syria region as early as the Early Hesperian within the Syria Mons unit and last flowed as recently as the Late Amazonian during emplacement of the north field. We identify a slightly longer temporal range for volcanism at Syria than Plescia (2004) and Baptista et al. (2008) possibly due to our expanded mapping area and use of a more complete higher resolution set of data. Regardless, our results indicate that volcanism at Syria likely spanned a period of time no longer than ~900 Ma. However, we also note that Hauber et al. (2011) conducted crater counts of select individual vents within Syria Planum, finding that some small shields might have erupted as recently as several hundred million years ago. Although our crater counts do not suggest significant temporal overlaps between the volcanic units, error bars do terminate against one another. As such, crater counts confirm our sequential inferences, but are inconclusive, taken on their own, with regard to differentiating between multiple and a single magma production event related to the emplacement of Syria Planum lava flows.

The application of spatial and alignment statistical analyses to vent location data within monogenetic vent fields on the Earth have previously enabled researchers to identify unique vent populations within a field and their relationships to regional tectonics (Connor and Conway, 2000, e.g.). Although such results are often supported by extensive field work, Bishop (2007) showed the value of conducting such analyses based on remote sensing data alone, and recently researchers have demonstrated the potential for using those analyses on martian vent fields (Bishop, 2008; Bleacher et al., 2009; Hamilton et al., 2010, 2011). The Nearest Neighbor and 2–Point Azimuth analyses used here are based on decades of terrestrial research supported by field work and are used here to provide additional insight into the development of Syria Planum where mapping and crater counting alone cannot adequately test our hypothesis.

Lutz (1986) and Lutz and Gutmann (1995) suggest that vent fields with nonrandom spatial distributions represent an overlap of more than one population of randomly spaced vents. Nearest Neighbor analyses for the entire Syria Planum vent field yields a non-random spatial distribution of vents. Based on our mapping that delineates a northern and southern shield field in Syria Planum, and the work of Lutz (1986) and Lutz and Gutmann (1995), we interpret this result to indicate that at least two populations of vents with unique spatial signatures make up the Syria Planum region. Together, the vents of these fields yield a nearest neighbor result of questionable consistency with a random Poisson distribution, but removal of the northern field from the southern field yields a result clearly consistent with a random Poisson distribution for the southern field (Table 3.3). As such, our geologic interpretation of the random statistical spacing of these features is that the southern shield field represents one unique population of volcanic vents. The spacing of 22 vents in the northern shield field is also consistent with a random distribution. One interpretation of these Nearest Neighbor results is the existence of more than one magma production event, each identified by a randomly sorted population of vents in the study area. Another interpretation of Syria's overall nonrandom vent spacing is that magmatic activity migrated towards the north where magma ascension might have been controlled by different tectonic influences that affected the spacing dynamics of the subsequently emplaced vent field. The Nearest Neighbor results are consistent with the possibility of more than one magma production event, in contrast with age-dating results, which do not identify any detectable hiatus in eruptive activity during the entirety of the observable volcanic history of Syria Planum. In spite of this contrast, we are able to confidently state that the southern field is representative of a significant magma production event. The addition of the northern field vents to the southern field vents confuses those results: a clear distinction between two magma production events (southern *and* northern) and a single evolving event (southern *to* northern) is not found.

Many terrestrial volcanic fields display migrations in activity throughout the eruptive cycle associated with a major magma production event. The Springerville Volcanic Field, AZ,

is perhaps one of the best examples of this process. Monogenetic volcanism of Springerville was active from Late Pliocene to Holocene (2.1 to 0.3 Ma), producing basaltic low shields and cinder cones. Over the course of its volcanic activity, vent formation migrated eastward by roughly 2.5 cm/yr. A compositional progression is also seen: volcanism erupted tholeiitic basalts early on and changed over time to erupt alkalic olivine basalts (Condit et al., 1989, 1999).

The results of two-point azimuth analysis for Syria reveal three predominant trends of vent alignment centered at  $0^\circ$ ,  $80^\circ$ , and  $320^\circ$  from north (Figure 3.6). We interpret the geologic cause of these alignments to be shallow faulting which constrained the placement of small vents. Most clearly, northwest faulting first observed by Baptista et al. (2008) occurred contemporaneously to the formation of the south field, which corresponds to the observed northwest vent alignment. Additionally, while the faulting pattern in the graben-rich basement unit trends NW, specifically trending between  $330$ - $350^\circ$  which corresponds to a paucity of inter-vent alignments (Figure 3.6), it is possible that faulting continues and shifts direction where this basement unit is buried. East-west trending graben are observed in the northwest region of the study area extending from the western margins of Noctis Labyrinthus towards the northern shield field, which might correspond to the vent alignments observed at  $80^\circ$ . Such a tectonic influence on magma ascension later in the development of the Syria Planum, particularly in the north, might have caused the confused Nearest Neighbor results discussed above. The alignment of vents to the north is not supported by faulting that is observable at the surface. This might provide insight into the possibility of buried regional-scale faults with north-south alignments.

This mapping project enables insight into the origin of Syria Mons and its relationship to the coalesced field of shields to the east and north. The mapping presented here and by Baptista et al. (2008) demonstrates that Syria Mons is comparable to other large Tharsis shield volcanoes in areal extent, although with a much lower relief than Olympus Mons and the Tharsis Montes. Does Syria Mons itself represent a unique magma production event that

is distinct from the coalesced shields? Superposition demonstrates a consistent embayment of Syria Mons by flows associated with the coalesced vent field. However, crater count data again cannot be used to rule out the possibility of synchronous eruptions within these two units as their error bars end against each other. It is not uncommon for terrestrial shield volcanoes to experience a dispersal of eruption sites in the late stages of volcano growth. This is perhaps best observed at Mauna Kea, Hawaii. As Hawaiian shield volcanoes transition from the tholeiitic shield building to alkali capping stages the eruptions become less frequent and produce shorter flows (Moore and Mark, 1992; Wolfe and Morris, 1996; Rowland and Garbeil, 2000; Bleacher and Greeley, 2008). This transition is the result of numerous effects primarily related to a decrease in magma delivery rate to the surface as the volcano is pulled away from the consistently active Hawaiian hotspot due to plate tectonics. This decrease in magma supply is no longer capable of sustaining a primary shallow magma reservoir at the older volcanoes like occurs at Kilauea or Mauna Loa, and as a result each eruption represents an isolated package of magma. Because these eruptions do not share a shallow magma source they each find their own way to the surface and the eruption sites are dispersed across the volcano. Like the decreased magma supply rate at Mauna Kea, a decrease in the magma supply rate under Syria Mons might have caused a similar dispersal of eruption sites from one central vent volcano to a series of independent vents. Coupled with changing regional stress fields that are displayed by different fault orientations throughout Syria Planum, it might be possible for one major magma production event under the Syria region to have evolved from a sustained central vent edifice (Syria Mons) to plains-style, coalesced vent field volcanism that itself migrated from the southeast to northwest of Syria.

Comparison of the vent spatial and alignment data with the tectonic history of the region yields additional insight into the sequential development of Syria. Syria Planum, and the surrounding areas, are identified as long standing centers of tectonic activity with major tectonic centers existing 1) between Syria and Claritas Fossae in the Noachian, 2) along the southern-central portion of Valles Marineris in the Late Noachian and Early Hesperian, and

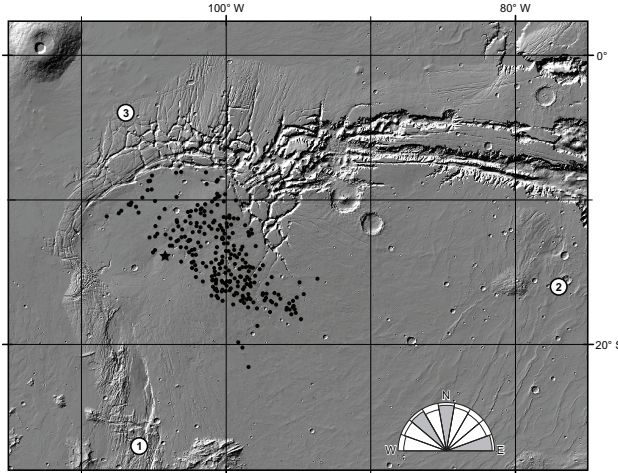


Figure 3.7: Anderson et al. (2001) described tectonic centers located at numbered circles: 1) between Syria and Claritas Fossae in the Noachian, 2) along the southern-central portion of Valles Marineris in the Late Noachian and Early Hesperian, and 3) northwest of Syria into the Early Hesperian. Black circles: vents in this study; star: Syria Mons. The rose diagram of Figure 6c is reproduced in the bottom right to illustrate similarities between inter-vent alignments and directions between Syria Planum and tectonic centers.

3) northwest of Syria into the Early Hesperian (Dohm and Tanaka, 1999; Anderson et al., 2001, 2004) (See Figure 3.7). Dohm and Tanaka (1999) suggest that these tectonic centers likely resulted from significant volcano-tectonic activity, and likely produced much of the volcanic deposition that is seen in those regions today. Some of the regional (hundreds to thousands of kilometers) graben structures crossing Syria Planum described by Dohm and Tanaka (1999), have previously been described as having been utilized as dike pathways subsequent to formation in the Syria and neighboring Thumasia Regions (Plescia and Saunders, 1982; Mege and Masson, 1996; Wilson and Head, 2002).

Comparison of our detailed analyses of the volcanic features within Syria to the tectonic evolution of Tharsis highlights some unique commonalities. The tectonic history suggests a change in location and decrease in intensity of tectonic activity towards the northeast across the Syria region from Claritas Fossae to Valles Marineris, then westward

across the northern extent of the Syria region between the Noachian and Early Hesperian (Dohm and Tanaka, 1999; Anderson et al., 2002; Anderson et al., 2004). Volcanism in Syria, as revealed in this study, migrated east away from Syria Mons, and subsequently to the northwest between Early Hesperian and Early Amazonian. This migration was coupled with an evolution from one major central vent volcano, to broadly distributed volcanism that formed many, smaller central vent volcanoes whose flow fields coalesced to completely resurface Syria. This style of volcanic evolution (single central vent to broadly distributed vents) is also associated, at least in part, with a waning magma supply on some terrestrial volcanoes (Moore and Mark, 1992; Wolfe and Morris, 1996; Rowland and Garbeil, 2000; Bleacher and Greeley, 2008). It is not clear at what time Syria Mons volcanism began. Dohm and Tanaka (1999) suggest that Noachian volcanism from the Syria region emplaced some of the basement units that were later deformed during the formation of Claritas Fossae and Webb et al. (2001) suggest that these eruptions built up the Syria Planum topographic rise by the Late Noachian to Early Hesperian as a major volcanic center that was > 2000 km in diameter and displaying at least 8 km of relief.

A coupled tectonic history of Tharsis and volcanic evolution of Syria is presented here. During the Noachian a center of province-wide tectonism was located between Syria and Claritas Fossae, essentially south of the study area. At this time extensive volcanic plains units were emplaced between Syria and the Thaumasia region to the south, for which no known vents are currently exposed at the surface in Syria. Tectonism at this time would have created radial crustal fractures that trended north through the study area, which is one of three orientations of heightened inter-vent relationships identified in the two-point azimuth analysis (Figure 3.6). Between the Late Noachian and Early Hesperian the center of Tharsis tectonism shifted northeastward towards Valles Marineris. At the same time volcanism in Syria evolved into a single central vent volcano, Syria Mons, although we cannot rule out the possibility of additional distributed volcanic centers across Syria that are now covered by younger deposits. At this time the tectonic center was located to the east of Syria and

would have created west trending crustal structures through the study area, which again is an orientation of heightened inter–vent relationships in Syria (Figure 3.6). During the Early Hesperian, as tectonism continued to shift, now towards the west/northwest, volcanism evolved into dispersed development of numerous small volcanic centers that were distributed across several hundred kilometers of the Syria region. Tectonism related to this center would have created southeast trending crustal structures across the study area at this time, which is the orientation of the third heightened inter–vent relationship orientations identified in this study (Figure 3.6). Following the Early Hesperian, tectonism was focused far to the north near Alba Patera. Volcanism in Syria declined through the Hesperian and eventually ended sometime in the Early Amazonian.

### 3.6 Conclusion

Mapping of the Syria Planum region of Mars shows at least 263 volcanic vents ranging in diameter from one volcano  $>100$  km (Syria Mons) to most volcanoes at 10s of km. Mapping, crater counts, and spatial and alignment statistical analyses reveal a complex volcano–tectonic history for this region that represents at least one major magma production event in the developmental history of Tharsis.

Mapping of lava flows and vents, and their superposition relationships shows a sequence of volcanic activity from a broad shield volcano, Syria Mons, in the early Hesperian to a coalesced field of individually, areally smaller shields that together resurfaced much of the region through the Late Hesperian, possibly including the shields in northwest Syria. This broadly distributed activity eventually became focused to form a northeast trending topographic ridge composed of the region’s youngest group of small shield volcanoes into the Early Amazonian. Crater counts support these mapping–based inferences, indicating that each stage of activity followed the previous stage with no significant hiatus and that each stage likely lasted between 60 and 650 Ma. Spatial statistics are inconclusive with regard to differentiating multiple events, but do suggest that the earlier coalesced shield field and the northern ridge shield field each represent a unique randomly distributed group of vents. We

interpret this result to indicate that each group's vents formed by the ascension and eruption of isolated magma bodies and did not share a common shallow magma reservoir for which magma scavenging of shared resources might have affected vent location.

Results from the study of Syria Planum tectonism and volcanism highlight the difficulty of identifying unique magma production events across planetary volcanic provinces for which detailed field work is not possible. It is assumed that major shield volcanoes on Mars might be related to magma production events similar to the concept of mantle plumes in terrestrial geology. However, the cause of eruptions for shield field volcanism across such large areas of the Martian crust are more difficult to interpret. Our remote sensing-based mapping, crater counts, and spatial and alignment analyses do not conclusively demonstrate either that Syria experienced one, evolving magma production event, or a series of unique events that are spatially overlapping. However, the tectonic evolution around and across Syria does demonstrate that the Syria region was influenced by evolving stress fields during the same timeframe that volcanic eruptions were occurring. We identify orientations of enhanced inter-vent alignments that are aligned with extensions of all three of the closest tectonic centers through our study area. Although buried, these structural features within the underlying crust of Syria appear to have influenced the ascension of magma bodies to the surface between the Early Hesperian and Early Amazonian, as is seen for the field of volcanic vents south of Pavonis Mons (Bleacher et al., 2009).

It is clear that the Syria Planum region is a major center of Tharsis volcanism, and that this volcanic center is surrounded by at least three major tectonic centers, which appear to have influenced the locations of vent formation across Syria. The mapped distribution (both spatially and temporally) of volcanism in the region can be used to provide direct constraints for testing various hypotheses of the internal processes such as geodynamical models of melt generation from mantle convection (O'Neill et al., 2007, e.g.) and/or lithospheric delamination (Scott and Wilson, 2003, e.g.). Although we cannot identify unique volcanic stages that are temporally isolated by eruptive hiatuses, we do identify the development

of two unique units of coalesced small shields. The emplacement of these two shield fields occurred over a period of 100–800 Ma, both following the development of a major central vent volcano. When taken as a whole, the entire region evolved from a central-vent volcano to dispersed volcanism across  $\sim$ 900 Ma. Our future work focuses on determining the volumes of lava erupted during these volcanic events as an additional modeling constraint. Continued mapping of surface features should provide direct constraints for future integrated geodynamic models of volcanic and tectonic processes that were related to significant Tharsis province magma production events.

Table 3.4: Notation

$c$	test statistic for spatial randomness.
$\bar{r}_a$	observed mean Nearest Neighbor distance.
$\bar{r}_e$	expected mean Nearest Neighbor distance.
$\sigma_e$	expected standard deviation of Nearest Neighbor distances.
$R$	index comparing $\bar{r}_a$ and $\bar{r}_e$ to test spatial randomness.
$d$	minimum significant distance of 2-point azimuth analysis.
$\mu_v$	mean inter-vent distance.
$\sigma_v$	standard deviation of inter-vent distances.
$\bar{x}_n$	mean quantity of inter-vent relationships in directional bins.
$\sigma_n$	standard deviation of inter-vent relationships in directional bins.

### 3.7 Acknowledgments

Funding for this project was provided to all three authors by NASA’s Mars Data Analysis Program. Additional support for J. Richardson was provided by NASA’s Undergraduate Student Research Program funding through Goddard Space Flight Center. We thank Nick Schmerr for insightful comments that improved the content of this report.

### 3.8 References

- Anderson, R. C., Dohm, J. M., Golembek, M. P., Haldemann, A. F. C., Franklin, B. J., Tanaka, K. L., Lias, J., and Peer, B. (2001). Primary centers and secondary concentrations of tectonic activity through time in the western hemisphere of Mars. *Journal of Geophysical Research*, 106(E9):20,563–20,585.
- Anderson, R. C., Dohm, J. M., Haldemann, A. F. C., and Hare, T. (2002). Comparative Investigation of the Geological Histories Among Alba Patera and Syria Planum, Mars. In *Lunar and Planetary Institute Science Conference Abstracts*, volume 33 of *Lunar and Planetary Institute Science Conference Abstracts*, page 1811.
- Anderson, R. C., Dohm, J. M., Haldemann, A. F. C., Hare, T. M., and Baker, V. R. (2004). Tectonic histories between Alba Patera and Syria Planum, Mars. *Icarus*, 171:31–38.
- Balogh, S. M., Glaze, L. S., and Bruno, B. C. (2007). Nearest-neighbor analysis of small features on Mars: Applications to tumuli and rootless cones. *Journal of Geophysical Research*, 112(E3):E03002. doi:10.1029/2005JE002652.
- Baptista, A. R., Mangold, N., Ansan, V., Baratoux, D., Lognonné, P., Alves, E. I., Williams, D. A., Bleacher, J. E., Masson, P., and Neukum, G. (2008). A swarm of small shield volcanoes on Syria Planum, Mars. *Journal of Geophysical Research*, 113(E9):E09010. doi:10.1029/2007JE002945.
- Baratoux, D., Pinet, P., Toplis, M. J., Mangold, N., Greeley, R., and Baptista, A. R. (2009). Shape, rheology and emplacement times of small martian shield volcanoes. *Journal of Volcanology and Geothermal Research*, 185(1-2):47–68. doi:10.1016/j.jvolgeores.2009.05.003.
- Beggan, C. and Hamilton, C. W. (2010). New image processing software for analyzing object size-frequency distributions, geometry, orientation, and spatial distribution. *Computers & Geosciences*, 36(4):539–549. doi:10.1016/j.cageo.2009.09.003.

Bishop, M. (2007). Point pattern analysis of eruption points for the Mount Gambier volcanic sub-province: a quantitative geographical approach to the understanding of volcano distribution. *Area*, 39(2):230–241. doi:10.1111/j.1475-4762.2007.00729.x.

Bishop, M. (2008). Higher-order neighbor analysis of the Tartarus Colles cone groups, Mars: The application of geographical indices to the understanding of cone pattern evolution. *Icarus*, 197(1):73–83. doi:10.1016/j.icarus.2008.04.003.

Bleacher, J. E., Glaze, L. S., Greeley, R., Hauber, E., Baloga, S. M., Sakimoto, S. E. H., Williams, D. A., and Glotch, T. D. (2009). Spatial and alignment analyses for a field of small volcanic vents south of Pavonis Mons and implications for the Tharsis province, Mars. *Journal of Volcanology and Geothermal Research*, 185(1–2):96–102. doi:10.1016/j.jvolgeores.2009.04.008.

Bleacher, J. E. and Greeley, R. (2008). Relating volcano morphometry to the developmental progression of Hawaiian shield volcanoes through slope and hypsometric analyses of SRTM data. *Journal of Geophysical Research*, 113:B09208. doi:10.1029/2006JB004661.

Bleacher, J. E., Greeley, R., Williams, D. A., Cave, S. R., and Neukum, G. (2007). Trends in effusive style at the Tharsis Montes, Mars, and implication for the development of the Tharsis province. *Journal of Geophysical Research*, 112:E09005. doi:10.1029/2006JE002873.

Brož, P. and Hauber, E. (2012). A unique volcanic field in Tharsis, Mars: Pyroclastic cones as evidence for explosive eruptions. *Icarus*, 218(1):88 – 99. doi:10.1016/j.icarus.2011.11.030.

Carr, M. H., Greeley, R., Blasius, K. R., Guest, J. E., and Murray, J. B. (1977). Some Martian volcanic features as viewed from the Viking orbiters. *Journal of Geophysical Research*, 82:3985–4015.

Cebriá, J. M., Martín-Escorza, C., López-Ruiz, J., Morán-Zenteno, D. J., and Martíny, B. M. (2011). Numerical recognition of alignments in monogenetic volcanic ar-

eas: Examples from the Michoacán-Guanajuato Volcanic Field in Mexico and Calatrava in Spain. *Journal of Volcanology and Geothermal Research*, 201(1–4):73–82. doi:10.1016/j.jvolgeores.2010.07.016.

Christensen, P., Jakosky, B., Kieffer, H., Malin, M., McSween, H., Nealson, K., Mehall, G., Silverman, S., Ferry, S., Caplinger, M., and Ravine, M. (2004). The Thermal Emission Imaging System (THEMIS) for the Mars 2001 Odyssey Mission. *Space Science Reviews*, 110(1):85–130. doi:10.1023/B:SPAC.0000021008.16305.94.

Clark, P. J. and Evans, F. C. (1954). Distance to Nearest Neighbor as a Measure of Spatial Relationships in Populations. *Ecology*, 35(4):445–453. doi:10.2307/1931034.

Condit, C. D., Crumpler, L. S., and Aubele, J. C. (1999). Lithologic, Age Group, Magnetopolarity, and geochemical maps of the Springerville Volcanic Field, East-Central Arizona. USGS Miscellaneous Investigations Series Map I-2431.

Condit, C. D., Crumpler, L. S., Aubele, J. C., and Elston, W. E. (1989). Patterns of Volcanism along the Southern Margin of the Colorado Plateau: The Springerville Field. *Journal of Geophysical Research*, 94(B6):7975–7986.

Connerney, J. E. P., Acuna, M. H., Ness, N. F., Kletetschka, G., Mitchell, D. L., Lin, R. P., and Reme, H. (2005). Tectonic implications of Mars crustal magnetism. *Proceedings of the National Academy of Science*, 102(42):14,970–14,974.

Connor, C. B. (1990). Cinder Cone Clustering in the TransMexican Volcanic Belt: Implications for Structural and Petrologic Models. *Journal of Geophysical Research*, 95(B12):19,395–19,405. doi:10.1029/JB095iB12p19395.

Connor, C. B. and Conway, M. F. (2000). Basaltic volcanic fields. In Sigurdsson, H., editor, *Encyclopedia of Volcanoes*, pages 331–343. Academic Press, San Diego, CA.

Dohm, J. M. and Tanaka, K. L. (1999). Geology of the Thaumasia region, Mars: plateau development, valley origins, and magmatic evolution. *Planetary and Space Science*, 47(3–4):411 – 431. doi:10.1016/S0032-0633(98)00141-X.

Greeley, R. (1977). Basaltic “plains” volcanism. In Greeley, R. and King, J. S., editors, *Volcanism of the Eastern Snake River Plain, Idaho: A Comparative Planetary Geology Guidebook*, NASA CR-154621, pages 23–44. NASA, Washington, D. C.

Greeley, R. (1982). The Snake River Plain, Idaho: Representative of a new category of volcanism. *Journal of Geophysical Research*, 87(B4):2705–2712. doi:10.1029/JB087iB04p02705.

Greeley, R. and Spudis, P. D. (1981). Volcanism on Mars. *Reviews of Geophysics and Space Physics*, 19:13–41.

Hamilton, C. W., Fagents, S. A., and Thordarson, T. (2011). Lava-ground ice interactions in Elysium Planitia, Mars: Geomorphological and geospatial analysis of the Tartarus Colles cone groups. *Journal of Geophysical Research*, 116(E3):E03004. doi:10.1029/2010JE003657.

Hamilton, C. W., Fagents, S. A., and Wilson, L. (2010). Explosive lava-water interactions in Elysium Planitia, Mars: Geologic and thermodynamic constraints on the formation of the Tartarus Colles cone groups. *Journal of Geophysical Research*, 115(E9):E09006. doi:10.1029/2009JE003546.

Hartmann, W. K. (2005). Martian cratering 8: Isochron refinement and the chronology of Mars. *Icarus*, 174(2):294 – 320. doi:10.1016/j.icarus.2004.11.023.

Hartmann, W. K. and Neukum, G. (2001). Cratering chronology and the evolution of Mars. *Space Science Reviews*, 96:165–194. doi:10.1023/A:1011945222010.

Hauber, E., Bleacher, J., Gwinner, K., Williams, D., and Greeley, R. (2009). The topography and morphology of low shields and associated landforms of plains volcanism in the

Tharsis region of Mars. *Journal of Volcanology and Geothermal Research*, 185(1–2):69–95.  
doi:10.1016/j.jvolgeores.2009.04.015.

Hauber, E., Brož, P., Jagert, F., Jodłowski, P., and Platz, T. (2011). Very recent and wide-spread basaltic volcanism on Mars. *Geophysical Research Letters*, 38:L10201.  
doi:10.1029/2011GL047310.

Head, J. W., Bryan, W. B., Greeley, R., Guest, J. E., Shultz, P. H., Sparks, R. S. J., Walker, G. P. L., Whitford-Stark, J. L., Wood, C. A., and Carr, M. H. (1981). Basaltic volcanic fields. In W. M. Kaula, et al., editor, *Basaltic Volcanism on the Terrestrial Planets*, pages 702–887. Pergamon Press Inc., New York.

Hodges, C. A. and Moore, H. J. (1994). Atlas of Volcanic Landforms on Mars, USGS Prof. Paper 1534. U. S. Govt. Printing Office, Washington, D. C.

Ivanov, B. A. (2001). Mars/Moon Cratering Rate Ratio Estimates. *Space Science Reviews*, 96:87–104. doi:10.1023/A:1011941121102.

Keszthelyi, L., Jaeger, W., McEwen, A., Tornabene, L., Beyer, R. A., Dundas, C., and Miallazzo, M. (2008). High Resolution Imaging Science Experiment (HiRISE) images of volcanic terrains from the first 6 months of the Mars Reconnaissance Orbiter Primary Science Phase. *Journal of Geophysical Research*, 113(E4):E04005. doi:10.1029/2007JE002968.

Lillis, R. (2006). Electron reflectometry as a probe of the Martian crust and atmosphere, doctoral thesis. Department of Physics, UC Berkeley.

Lillis, R. J., Dufek, J., Bleacher, J. E., and Manga, M. (2009). Demagnetization of crust by magmatic intrusion near the Arsia Mons volcano: Magnetic and thermal implications for the development of the Tharsis province, Mars. *Journal of Volcanology and Geothermal Research*, 185(1-2):123–138. doi:10.1016/j.jvolgeores.2008.12.007.

Lutz, T. M. (1986). An Analysis of the Orientations of Large-scale Crustal Structures:A Statistical Approach Based on Areal Distributions of Pointlike Features. *Journal of Geophysical Research*, 91(B1):421–434. doi:10.1029/JB091iB01p00421.

Lutz, T. M. and Gutmann, J. T. (1995). An improved method for determining and characterizing alignments of pointlike features and its implications for the Pinacate volcanic field, Sonora, Mexico. *Journal of Geophysical Research*, 100(B9):17,659–17,670. doi:10.1029/95JB01058.

Malin, M. C., Bell, J. F., Cantor, B. A., Caplinger, M. A., Calvin, W. M., Clancy, R. T., Edgett, K. S., Edwards, L., Haberle, R. M., James, P. B., Lee, S. W., Ravine, M. A., Thomas, P. C., and Wolff, M. J. (2007). Context Camera Investigation on board the Mars Reconnaissance Orbiter. *Journal of Geophysical Research*, 112(E5):E05S04. doi:10.1029/2006JE002808.

Mege, D. and Masson, P. (1996). A plume tectonics model for the Tharsis Province, Mars. *Planetary and Space Science*, 44:1499–1546.

Michael, G. and Neukum, G. (2010). Planetary surface dating from crater size–frequency distribution measurements: Partial resurfacing events and statistical age uncertainty. *Earth and Planetary Science Letters*, 294(34):223 – 229. doi:10.1016/j.epsl.2009.12.041.

Moore, J. G. and Mark, R. K. (1992). Morphology of the Island of Hawaii. *GSA Today*, 2(11):257–262.

Mouginis-Mark, P. J., Wilson, L., and Zuber, M. T. (1992). The physical volcanology of Mars. In H. H. Kieffer, et al., editor, *Mars*, pages 424–452. The University of Arizona Press, Tucson.

Neukum, G., Jaumann, R., Hoffmann, H., Hauber, E., Head, J. W., Basilevsky, A. T., Ivanov, B. A., Werner, S. C., van Gasselt, S., Murray, J. B., McCord, T., and TeamThe, H.

- R. S. C.-I. C. (2004). Recent and episodic volcanic and glacial activity on Mars revealed by the High Resolution Stereo Camera. *Nature*, 432(7020):971–979. doi:10.1038/nature03231.
- O'Neill, C., Lenardic, A., Jellinek, A. M., and Kiefer, W. S. (2007). Melt propagation and volcanism in mantle convection simulations, with applications for Martian volcanic and atmospheric evolution. *Journal of Geophysical Research*, 112(E7):E07003+. doi:10.1029/2006JE002799.
- Plescia, J. B. (2004). Morphometric properties of Martian volcanoes. *Journal of Geophysical Research*, 109(E3):E03003. doi:10.1029/2002JE002031.
- Plescia, J. B. and Saunders, R. S. (1982). Tectonic history of the Tharsis region, Mars. *Journal of Geophysical Research*, 87(B12):9775–9791.
- Richardson, J., Bleacher, J., Connor, C., and Connor, L. (2012). Using spatial density to characterize volcanic fields on mars. In *Lunar and Planetary Institute Science Conference Abstracts*, volume 43, page 2314.
- Richardson, J. A., Bleacher, J. E., and Baptista, A. R. (2010). Identification of Volcanic Ridge in Northern Syria Planum, Mars: Constraint on Geologic History of Syria. In *Lunar and Planetary Institute Science Conference Abstracts*, volume 41 of *Lunar and Planetary Inst. Technical Report*, page 1427.
- Roberts, K. S., Davies, R. J., Stewart, S. A., and Tingay, M. (2011). Structural controls on mud volcano vent distributions: examples from Azerbaijan and Lusi, east Java. *Journal of the Geological Society*, 168(4):1013–1030. doi:10.1144/0016-76492010-158.
- Rowland, S. K. and Garbeil, H. (2000). Slopes of oceanic basalt volcanoes. In P. J. Mouginis-Mark, et al., editor, *Remote Sensing of Active Volcanism*, *Geophys. Monogr. Ser.*, volume 116. AGU, Washington, D. C. doi:10.1029/GM116p0223.

Sakimoto, S. E. H., Gregg, T. K. P., Hughes, S. S., and Chadwick, J. (2003). Re-Assessing Plains-style Volcanism on Mars. In A. L. Albee & H. H. Kieffer, editor, *Sixth International Conference on Mars*, page 3197.

Scott, D. H. and Tanaka, K. L. (1986). Geologic map of the Western Equatorial region of Mars. USGS Miscellaneous Investigations Series Map I-1802-A.

Scott, E. and Wilson, L. (2003). Did the Alba Patera and Syria Planum regions of Mars lose their lithospheric roots in convective overturn events? *Journal of Geophysical Research*, 108(E5):5035+. doi:10.1029/2002JE001492.

Smith, D. E., Zuber, M. T., Neumann, G. A., Guinness, E. A., and Slavney, S. (2003). Mars Global Surveyor Laser Altimeter Mission Experiment Gridded Data Record. NASA Planetary Data System, MGS-M-MOLA-5-MEGDR-L3-V1.0.

Tanaka, K. L. and Davis, P. A. (1988). Tectonic History of the Syria Planum Province of Mars. *Journal of Geophysical Research*, 93(B12):14,893–14,917. doi:10.1029/JB093iB12p14893.

Wadge, G. and Cross, A. (1988). Quantitative methods for detecting aligned points: An application to the volcanic vents of the Michoacan-Guanajuato volcanic field, Mexico. *Geology*, 16(9):815–818. doi:10.1130/0091-7613(1988)016<0815:QMFDAP>2.3.CO;2.

Wadge, G. and Cross, A. M. (1989). Identification and analysis of the alignments of point-like features in remotely-sensed imagery. Volcanic cones in the Pinacate Volcanic Field, Mexico. *International Journal of Remote Sensing*, 10:455–474. doi:10.1080/01431168908903885.

Webb, B., Head, III, J. W., Kortz, B. E., and Pratt, S. (2001). Syria Planum, Mars: A Major Volcanic Construct in the Early History of Tharsis. In *Lunar and Planetary Institute Science Conference Abstracts*, volume 32 of *Lunar and Planetary Institute Science Conference Abstracts*, page 1145.

Werner, S. and Tanaka, K. (2011). Redefinition of the crater-density and absolute-age boundaries for the chronostratigraphic system of Mars. *Icarus*, 215(2):603 – 607. doi:10.1016/j.icarus.2011.07.024.

Whitford-Stark, J. L. (1982). Factors influencing the morphology of volcanic landforms: An Earth-Moon comparison. *Earth Science Reviews*, 18:109–168.

Wilson, L. and Head, J. W. (2002). Tharsis-radial graben systems as the surface manifestation of plume-related dike intrusion complexes: Models and implications. *Journal of Geophysical Research*, 107(E8):5057. doi:10.1029/2001JE001593.

Wilson, L., Mouginis-Mark, P. J., Tyson, S., Mackown, J., and Garbeil, H. (2009). Fissure eruptions in Tharsis, Mars: Implications for eruption conditions and magma sources. *Journal of Volcanology and Geothermal Research*, 185(1-2):28–46. doi:10.1016/j.jvolgeores.2009.03.006.

Wolfe, E. W. and Morris, J. (1996). Geologic map of the Island of Hawaii, scale 1:100,000. USGS Miscellaneous Investigations Series Map I-2524-A.